JEM Journal of Experimental Medicine

ARTICLE

Inflammation rewires the enteric nervous system through neurogenic monocyte recruitment

Sravya Kurapati[1,2*], Changsik Shin[3*], Krisztina Szabo[1*], Yu Liu[4], Azree Z. Ashraf[1], Balazs Koscso[1], Chinmayee Dash[5], Katherine L. Kruckow[1], Leonardo E. Navarro[1], Amanda M. Clark[6], Monalee Saha[7], Sushma Nagaraj[7], Wenhui Wang[4], Jun Zhu[4], Kevin Brown[6], Travis Thomson[8], Natalia Shulzhenko[9], Andrey Morgun[6], Christina E. Baer[10], Shanthi Srinivasan[11], Subhash Kulkarni[7,12], Pankaj J. Pasricha[7,13], Lauren A. Peters[4,14], and Milena Bogunovic[1,3]

Proper organization of the enteric nervous system (ENS) is critical for normal gastrointestinal (GI) physiology. Inflammatory bowel disease (IBD) disrupts key GI functions, including bowel motility. However, in many IBD patients, motility disorders persist even during remission, suggesting an irreversible ENS defect secondary to IBD. Here, we show that postinflammatory GI motility dysfunction arises from structural remodeling of the ENS, driven by a combination of neuronal loss and neurogenesis. During mucosal inflammation, enteric neurons upregulate CCL2 expression, facilitating the recruitment of monocytes into the myenteric plexus within the intestinal muscle. Monocyte-derived macrophages infiltrate the myenteric ganglia, contributing to excessive ENS remodeling and postinflammatory motility dysfunction. This neuroimmune axis is counterbalanced by a hypoxia-induced stress response in enteric neurons mediated by HIF1α. Enhancing the neuron-intrinsic hypoxia pathway limits ENS remodeling and preserves motility. In summary, this study presents a mechanistic model of postinflammatory GI motility dysfunction and proposes a therapeutic strategy to maintain ENS integrity and function during inflammation.

Introduction

Inflammatory bowel disease (IBD), which includes Crohn's disease (CD) and ulcerative colitis (UC), is a progressive inflammatory condition of the gastrointestinal (GI) tract of noninfectious etiology. Significant progress has been made in the treatment of active inflammation in patients with IBD. However, many patients with IBD in remission develop functional GI disorders including irritable bowel syndrome (IBS), and present with a wide range of symptoms such as chronic abdominal pain and various GI motility dysfunctions (dysmotility) affecting both upper and lower gut regions (Brierley and Linden, 2014; Keller et al., 2009; Rezaie et al., 2018; Gu et al., 2018; Ohman and Simren, 2010). Despite this, there is a lack of understanding of how IBD permanently dysregulates key GI functions.

The GI tract performs vital physiological functions related to food and water consumption. Its dense innervation by the central and peripheral nervous systems allows it to carry out complex physiological processes in a highly coordinated manner. Most peripheral neurons that innervate the GI tract are embedded in the gut wall, where they form the enteric nervous system (ENS), the largest collection of neurons outside the central nervous system (Furness, 2012). The vital physiological GI functions (smooth muscle contractility, epithelial barrier integrity, and blood flow) and some aspects of its mucosal

[1]Department of Pathology, University of Massachusetts Chan Medical School, Worcester, MA, USA; [2]The Biomedical Sciences PhD Program, Penn State University College of Medicine, Hershey, PA, USA; [3]Department of Microbiology and Immunology, Penn State University College of Medicine, Hershey, PA, USA; [4]Department of Genetics & Genomic Sciences, Icahn School of Medicine at Mount Sinai, New York, NY, USA; [5]The Morningside Graduate School of Biomedical Sciences at the UMass Chan Medical School, Worcester, MA, USA; [6]Department of Pharmaceutical Sciences, College of Pharmacy, Oregon State University, Corvallis, OR, USA; [7]Center for Neurogastroenterology, Johns Hopkins University School of Medicine, Baltimore, MA, USA; [8]Department of Neurobiology, University of Massachusetts Chan Medical School, Worcester, MA, USA; [9]College of Veterinary Medicine, Oregon State University, Corvallis, OR, USA; [10]Department of Microbiology, Sanderson Center for Optical Experimentation (SCOPE), University of Massachusetts Chan Medical School, Worcester, MA, USA; [11]Division of Digestive Diseases, Department of Medicine, Emory University School of Medicine, Atlanta, GA, USA; [12]Division of Gastroenterology, Department of Medicine, Beth Israel Deaconess Medical Center, Harvard Medical School, Boston, MA, USA; [13]Department of Medicine, Mayo Clinic, Scottsdale, AZ, USA; [14]Icahn Genomics Institute, Icahn School of Medicine at Mount Sinai, New York, NY, USA.

*S.Kurapati, C. Shin, and K. Szabo contributed equally to this paper. Correspondence to Milena Bogunovic: milena.bogunovic@umassmed.edu

C. Shin's current affiliation is CJ Bioscience, Suwon-si, South Korea. K. Szabo's current affiliation is Division of Neonatology, Department of Pediatrics, University of Florida College of Medicine, Gainesville, FL. B. Koscso's current affiliation is Obsidian Therapeutics, Cambridge, MA. M. Saha's current affiliation is Cellular and Immuno Analytical Research Department, PPD-Thermo Fisher Scientific at GSK Rockville Center for Vaccine Research, Rockville, MD. S. Nagaraj's current affiliation is Department of Neurology, Johns Hopkins University, Baltimore, MD.

immune response are tightly regulated by the ENS (Furness, 2012; Kulkarni et al., 2021). Of the several layers of the gut, the intestinal mucosa is the most proximal to the lumen and is exposed to various stressors, while the somas of enteric neurons are positioned outside of the mucosa in two major plexuses, submucosal and myenteric, with preferential control of the epithelial barrier and smooth muscle contractility, respectively (Sharkey and Mawe, 2023). Significant advances have been made in our understanding of mucosal immune responses in IBD, but extra-mucosal cellular GI compartments, specifically the ENS, have received proportionally less attention. So, it remains largely unknown how mucosal inflammation affects ENS homeostasis and function in IBD (Brierley and Linden, 2014).

A unique population of intestinal macrophages named muscularis macrophages (MMs) resides in the outer smooth muscle layer of the intestine (muscularis externa), where it anatomically associates with nerve fibers and somas of myenteric neurons (Muller et al., 2014; Gabanyi et al., 2016; Phillips and Powley, 2012). Macrophages are immune cells with "housekeeping" functions (Park et al., 2022), and accumulating evidence points to a symbiotic relationship between MMs and enteric neurons in early postnatal ENS development and homeostasis of adult ENS in health and GI infection (Matheis et al., 2020; Viola et al., 2023; De Schepper et al., 2019; Muller et al., 2014), but the functional connection between the two cell types in IBD is yet to be identified.

Here, we sought to establish the mechanisms of postinflammatory GI dysmotility. In a mouse study supported by some human data, we tested the hypothesis that mucosal inflammation in IBD alters homeostatic crosstalk between enteric neurons and MMs. As a result, we uncovered a colitis-driven neuroimmune pathway underlying pathological remodeling of the ENS with associated GI dysfunction and identified its regulatory axis.

Results

Transient colitis induces structural remodeling of the ENS

IBD is a chronic inflammatory condition with a relapsing–remitting pattern. To study postinflammatory GI dysmotility, we established a model of transient colitis to reflect phases of active mucosal inflammation and postinflammatory remission based on the chronic dextran sodium sulfate (DSS) colitis model (Chassaing et al., 2014). Eight-week-old C57BL/6 (B6) wild-type (WT) mice were given three 5-day cycles of DSS to maintain active colitis for 4 weeks (3×DSS colitis); then, mice were followed for another 6–8 weeks until a nearly complete recovery to reproduce remission in patients with IBD (Fig. 1 A). The DSS phase was associated with significant body weight loss, increased fecal lipocalin-2 concentration used as a biomarker of mucosal inflammation (Chassaing et al., 2012) (Fig. 1, B and C), increased fecal water content, occult blood (Fig. S1, A and B), and increased mucosal macrophage and neutrophil counts, consistent with active mucosal inflammation (Fig. 1, D and E). By the late postinflammatory phase, most of the inflammatory readouts had normalized (Fig. 1, B–E; and Fig. S1, A and B), consistent with recovery. Despite "remission," mice with a history of DSS treatment exhibited signs of GI dysmotility, as evidenced by accelerated GI transit, contrasting to the delayed GI transit observed during active colitis (Fig. 1 F). The shortened colon at the postinflammatory phase, although significantly longer compared with the DSS phase (Fig. S1 C), indicated altered contraction of intestinal smooth muscle. Given the essential role of the ENS in GI motility (Furness, 2012), the observed dysmotility in post-colitis 3×DSS mice suggests functional ENS alterations. Consequently, we focused on elucidating the changes in the ENS induced by colitis.

We imaged the colonic myenteric plexus at different stages of colitis and post-colitis. Littermate mice were treated with 3×DSS or water (control). The colonic muscularis externa was isolated at the early acute (weeks 1 and 3) and late postinflammatory (after week 10) time points, and the same regions of the colonic myenteric plexus were stained with the antibodies against Hu (B, C, and D subunits) (Kulkarni et al., 2023), βIII-tubulin, and MHC Class II (MHCII) to visualize neuronal somas, nerve fiber network, and macrophages, respectively, and imaged by confocal microscopy (Fig. 1 G). The total number of myenteric neurons, neuronal density, and nerve fiber architecture were compared between the groups. We found significant structural changes in the myenteric plexus of mice with colitis, and the pattern of these changes differed between the early and late time points as colitis progressed and regressed (Fig. 1, H–L). At week 1, colitis was associated with a significant reduction in the total number of myenteric neurons (Fig. 1 H), which was also reflected in the fragmentation of larger ganglia into smaller clusters (Fig. 1, I and J). Regions between βIII-tubulin$^+$ interganglionic nerve fiber tracts (IGFTs), referred to as IGFT regions (Fig. 1 G), were quantified along with their area and used as indirect readouts to assess structural changes in the fiber network of the myenteric plexus. Compared with water-treated controls, the myenteric plexus of inflamed mice showed a reduction in the number (Fig. 1 K) and an increase in size of the IGFT regions (Fig. 1 L). These data suggest that the structural changes of the myenteric plexus observed in colitis result from a partial loss of myenteric neurons and disruption of the nerve fibers linking adjacent ganglia. These changes were more evident at week 3 of colitis. In contrast to the colitis phase (weeks 1 and 3), by the late postinflammatory phase (week 10), the total number of myenteric neurons appeared to have recovered completely (Fig. 1 H, left panel). However, analysis of neuronal counts using pooled values (Fig. 1 H, right panel) indicated an incomplete recovery. Supporting this, we observed that in the 3×DSS group, the number of neuronal clusters, although reduced over time, remained increased compared with the controls at week 10 (Fig. 1 I, both panels). Similarly, neuronal density (quantified as the number of neurons per cluster) increased over time in the 3×DSS group but remained lower than the controls at week 10 (Fig. 1 J, both panels). Collectively, these readouts indicated a partial recovery of neurons in the postinflammatory phase. Interestingly, neuronal density was found to vary markedly across the examined fields, with regions of severe neuronal loss interspersed with hyperplastic ganglia (Fig. 1, G–J, right panels), suggesting variation in recovery among the ganglia. Additionally, we observed an increase in the

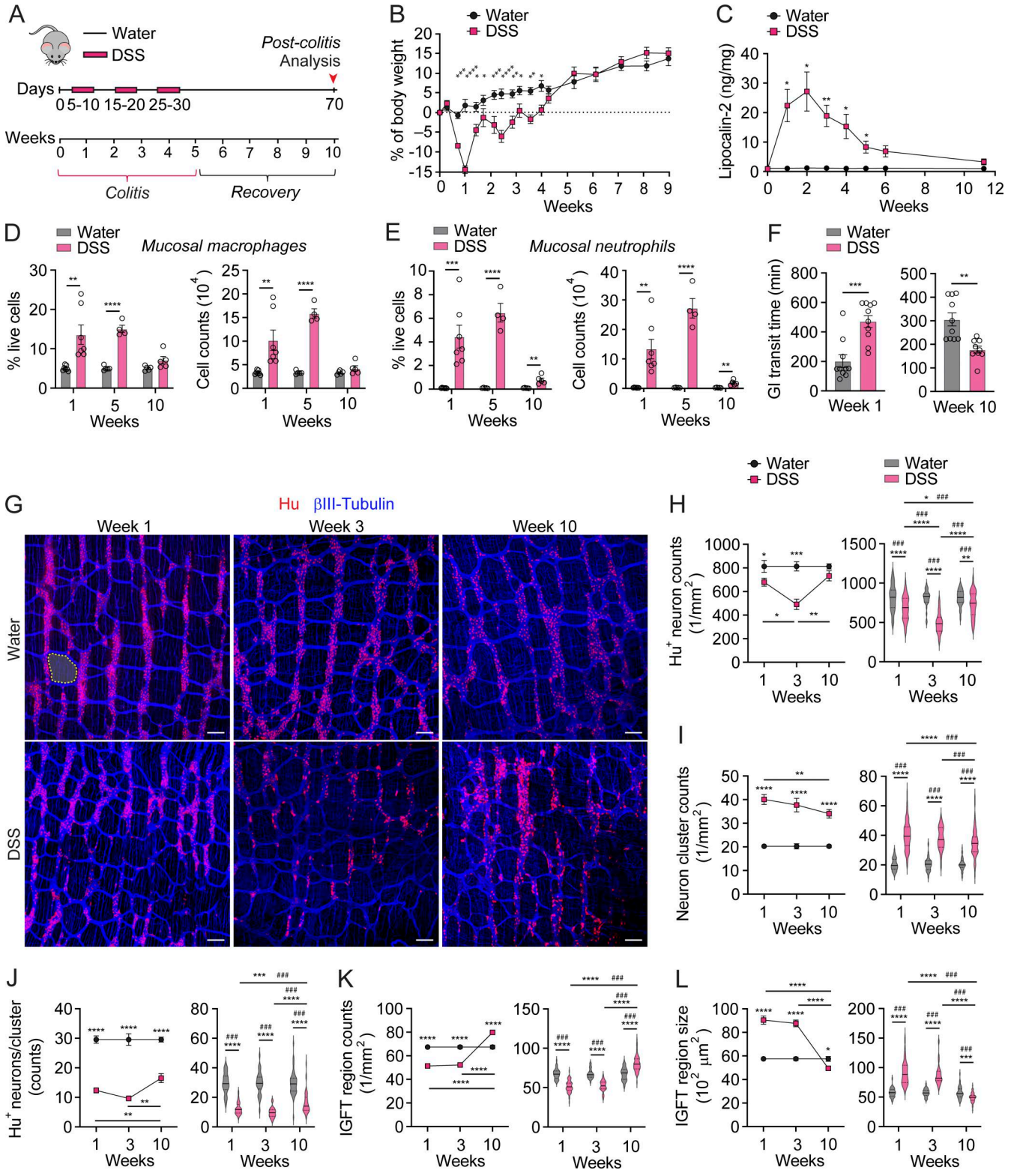

Figure 1. **Transient colitis leads to long-term postinflammatory GI dysmotility and structural remodeling of the myenteric plexus. (A)** Experimental design of transient 3×DSS colitis (3.5% DSS in drinking water). **(B)** Percentage of body weight change in 3×DSS- or water-treated WT mice (n = 10 per group). **(C)** Fecal lipocalin-2 in 3×DSS- or water-treated WT mice, measured by ELISA (control, n = 4; DSS, n = 8). **(D)** Percentage of total viable cells (left) and absolute cell counts (right) of colonic mucosal macrophages in 3×DSS- or water-treated mice, quantified by FC (control, n = 5–7; DSS, n = 4–7). **(E)** Percentage of total viable cells (left) and absolute cell counts (right) of colonic mucosal neutrophils in 3×DSS- or water-treated mice, quantified by FC (control, n = 5–7; DSS, n = 4–7). **(F)** GI transit in 3×DSS- or water-treated mice at week 1 and week 10 after starting DSS (control, n = 10; DSS, n = 9–10). **(G)** Confocal images of colonic myenteric plexus isolated from 3×DSS- or water-treated mice and stained with Hu (neuronal somas), βIII-tubulin (nerve fibers), and MHCII (MMs, channel turned off) antibodies. Images are representative of control (n = 5–10) and DSS (n = 4–13) for each time point. Scale bars, 100 µm. **(H–J)** Changes in colonic

myenteric ganglia displayed in G of mice described in A showing (H) total counts of Hu$^+$ neurons, (I) counts of neuron clusters, and (J) counts of Hu$^+$ neurons per cluster, quantified by confocal microscopy. Data are shown as the mean value per mouse (left, control, n = 5–10; DSS, n = 4–13) or as distribution of pooled values generated from analysis of 4–9 fields of view per mouse (right). **(K and L)** Changes in nerve fiber architecture of colonic myenteric plexus displayed in G of mice described in A showing (K) counts of IGFT regions and (L) area of IGFT regions, quantified by confocal microscopy. Highlighted area in G is an example of IGFT regions identified as spaces between Hu$^+$ myenteric ganglia and βIII-tubulin$^+$ fiber tracts (see Materials and methods). Data are shown as the mean value per mouse (left, control, n = 5–10; DSS, n = 4–13) or as distribution of pooled values generated from analysis of 4–9 fields of view per mouse (right). All graphs show the mean ± SEM, n—mice. Data are representative of at least three independent experiments with similar results. Statistical analyses: unpaired Student's t test (F), multiple t tests (C–E), and two-way ANOVA for multiple comparisons (H–L), *P ≤ 0.05, **P ≤ 0.01, ***P ≤ 0.001, and ****P ≤ 0.0001. # above pooled data in violin plots (right, H–L) indicates empirical P values calculated by the Nested Leave-One-Out Jackknife strategy, where, ###P < 0.001. ANOVA, analysis of variance; FC, flow cytometry.

number but a reduction in the size of interganglionic spaces, indicative of newly formed IGFTs, and, as a result, a denser nerve fiber network (Fig. 1, K and L). Taken together, transient colitis results in the redistribution of myenteric neurons with regions of neuronal loss and hyperplasia and increased nerve fiber density of the myenteric plexus.

Neuronal loss and neurogenesis underlie colitis-induced ENS remodeling

A partial loss of enteric neurons due to programmed cell death has been described in the acute phase of colitis (Gulbransen et al., 2012; Matheis et al., 2020; Forster et al., 2025), and a long-term study in infectious colitis showed progressive neuronal loss (Matheis et al., 2020). We therefore used a second approach based on flow cytometry to assess neuronal loss and recovery after colitis. We established that a cell suspension of murine muscularis externa contained the CD45$^-$ (non-hematopoietic) CD90$^+$CD24$^+$ single-cell subset positive for a pan-neuronal marker PGP9.5 (Fig. S1, D and E). CD90$^+$CD24$^+$ single cells also selectively expressed neuron-specific genes *Elavl3* (encodes Hu C subunit) and *Elavl4* (encodes Hu D subunit) (Fig. S1 F) and a neuron-specific nucleosome component BAF53b in *Actl6b*:tdTomato reporter mice which were generated by crossing BAF53b(*Actl6b*)^{Cre} mice (Zhan et al., 2015; Morarach et al., 2021) with *Rosa26*(*R26*)-STOP$^{flox(fl)/fl}$tdTomato mice (Fig. S1, G–I). When we quantified the number of CD90$^+$CD24$^+$ single cells in the muscularis externa of mice with 3×DSS colitis and controls, the reduction of CD90$^+$CD24$^+$ cells in the DSS group was transient (Fig. 2 A), consistent with confocal microscopy. Therefore, neuronal loss in response to mucosal inflammation is reversed after colitis.

Abrupt localized genetic depletion of adult myenteric neurons *in vivo* has been shown to be followed by their gradual repopulation, along with the emergence of new nerve fiber projections from the neighboring intact regions (Stavely et al., 2024). Based on this, we hypothesized that the changes in the myenteric plexus observed following colitis are driven by enteric neurogenesis. Nestin is a stem cell marker (Tong and Yin, 2024), and Nestin$^+$ progenitor cells can give rise to adult enteric neurons (Kulkarni et al., 2017; Belkind-Gerson et al., 2013; Belkind-Gerson et al., 2015); however, the extent of neurogenesis in the adult intestine, both under normal and inflamed conditions, remains a topic of ongoing debate (Sharkey and Mawe, 2023). To test the contribution of neurogenesis to colitis-induced ENS remodeling, we used a previously described fate-mapping approach (Kulkarni et al., 2017) based on tamoxifen-treated *Nestin*(*Nes*)$^{ER\text{-}Cre}$*R26*-STOP$^{fl/fl}$tdTomato (*Nes*:tdTomato) mice to label newborn neurons. To verify that Nestin$^+$ progenitors can give rise to mature neurons, we cultured myenteric neurons (Zhang and Hu, 2021) from tamoxifen-treated adult *Nes*:tdTomato mice. Two weeks later, we detected clusters of tdTomato$^+$ Hu$^+$PGP9.5$^+$βIII-tubulin$^+$ mature neurons (Fig. S2, A and B). To exclude the possibility that Nestin is upregulated by mature neurons, we cultured myenteric neurons from adult tamoxifen-untreated *Nes*:tdTomato or neuron-specific SLICK-H:tdTomato mice (as a control) and 2 weeks later added 4-hydroxytamoxifen to the established neuronal cultures. Only neurons from SLICK-H:tdTomato mice upregulated tdTomato, while no tdTomato was observed in *Nes*:tdTomato neurons, indicating a lack of Nestin expression in mature neurons (Fig. S2 C). Further, *Nes* was not upregulated in differentiated neuronal cultures treated with lipopolysaccharide (LPS) or in sorted CD90$^+$CD24$^+$ neurons derived from DSS-treated mice (Fig. S2, D and E). Therefore, *Nes*:tdTomato mice represent a relevant model for studying enteric neurogenesis *in vivo*.

After only one cycle of DSS given to tamoxifen-treated *Nes*:tdTomato mice, we detected new tdTomato$^+$Hu$^+$ myenteric neurons at the post-colitis phase. Specifically, tdTomato$^+$ labeling of cell bodies of Hu$^+$ cells inside the ganglia, along with nerve fibers embedded into the myenteric plexus, is consistent with mature neurons (Fig. 2, B and C). Other tdTomato$^+$ cell types included intraganglionic S100β$^+$ enteric glial cells and extraganglionic vascular cells (Fig. S3 A). Next, we quantified the number of Nestin$^+$ progenitor-derived neurons in the 3×DSS model (Fig. 2 B). The analysis of colon cross-sections and the intact myenteric plexus after colitis revealed tdTomato$^+$Hu$^+$ neurons in all colon regions, indicating tissue-wide neurogenesis in response to colitis (Fig. S3, B and C). Overall, ∼6–12% of myenteric neurons were tdTomato-labeled during the postinflammatory phase, although labeling varied considerably across fields and mice, with some reaching up to 20% (Fig. 2, E and F; and Fig. S3, C–F). The higher frequency of tdTomato$^+$ neurons in post-3×DSS mice as compared to age-matched littermates undergoing the same tamoxifen treatment regimen suggested that the increase in tdTomato$^+$ CD90$^+$CD24$^+$ cells upon DSS was happening due to colitis-related factors and not due to age-related upregulation of Nestin in mature neurons. Taken together, these experiments provide *in vivo* evidence of significant Nestin$^+$ progenitor-driven neurogenesis upon colitis recovery. Thus, increased neurogenesis forms the biological basis for the recovery of neuronal counts and remodeled ENS architecture observed after colitis.

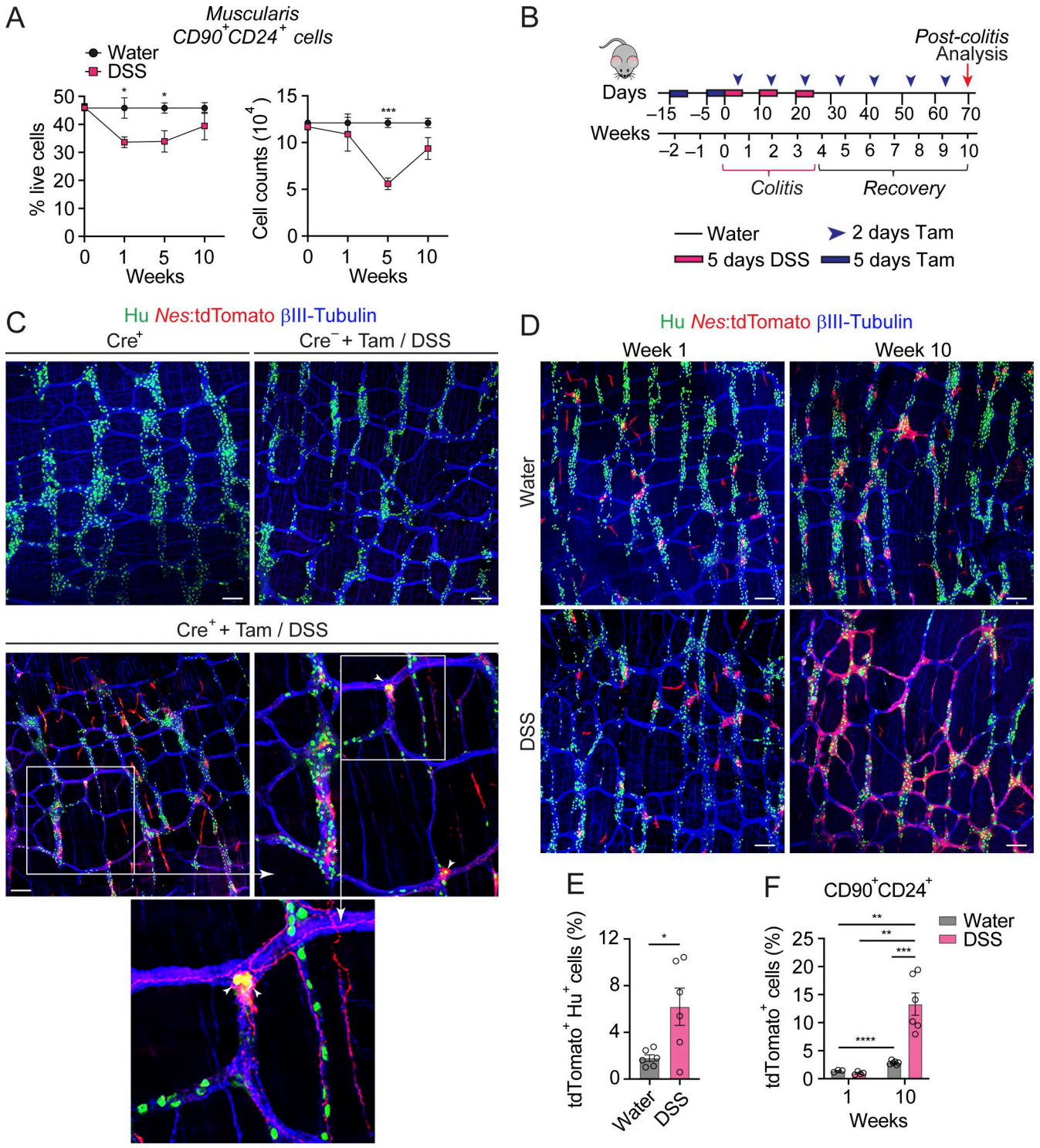

Figure 2. **Transient colitis induces neurogenesis, contributing to structural remodeling of the myenteric plexus. (A)** Percentage of total viable cells (left) and absolute cell counts (right) of colonic muscularis CD45⁻CD90⁺CD24⁺ neurons in 3×DSS- or water-treated WT mice, quantified by FC (control, *n* = 5–7; DSS, *n* = 4–7). **(B)** Experimental design used in D: 3×DSS (2.15%) was given with the tamoxifen (Tam) regimen as shown. In C, only 1×DSS was given with the same tamoxifen regimen. **(C)** Confocal images of colonic myenteric plexus isolated from tamoxifen- and 1×DSS-treated *Nes*$^{ER\text{-}Cre}$*Rosa26*(*R26*)-STOP$^{fl/-fl}$tdTomato (Cre⁺+Tam/DSS) and control *R26*-STOP$^{fl/fl}$tdTomato (Cre⁻ +Tam/DSS) mice, as well as untreated *Nes*$^{ER\text{-}Cre}$*R26*-STOP$^{fl/fl}$tdTomato (Cre⁺) mice on day 45 (6.5 wk), stained with antibodies to Hu (neuronal somas), tdTomato (newborn cells), and βIII-tubulin (nerve fibers). Scale bars, 100 µm. **(D)** Confocal images of colonic myenteric plexus from tamoxifen- and 3×DSS- or water-treated *Nes*$^{ER\text{-}Cre}$*R26*-STOP$^{fl/fl}$tdTomato (Cre⁺) mice at week 1 and 10 after starting DSS, stained with Hu, tdTomato, and βIII-tubulin antibodies. Images are representative of control (*n* = 3–6) and DSS (*n* = 4–6) for each time point. Scale bars, 100 µm. **(E)** Percentage of tdTomato⁺Hu⁺ neurons in the colonic myenteric plexus from Cre⁺ mice described in D at week 10, based on confocal microscopy (*n* = 6 per group). Data represent the mean ± SEM of 5–10 fields of view analyzed per mouse per group. **(F)** Percentage of newly generated tdTomato⁺ cells among CD45⁻CD90⁺CD24⁺ colonic myenteric neurons isolated from mice described in D, quantified by FC (control, *n* = 3–6; DSS, *n* = 4–6). Week 10 data are from the

same mice as in D. All graphs show the mean ± SEM, *n*—mouse. Data are representative of at least two independent experiments with similar results. Statistical analyses: multiple *t* test (A), unpaired Student's *t* test (E and F), *P ≤ 0.05, **P ≤ 0.01, ***P ≤ 0.001, and ****P ≤ 0.0001.

ENS remodeling is also a hallmark of progressive colitis

To evaluate the relevance of our findings in the 3×DSS model to IBD, we assessed ENS remodeling in a genetic mouse model of IBD and in intestinal tissue samples from IBD patients. As opposed to mice with transient colitis, age-matched *Il10*$^{-/-}$ mice with spontaneous colitis (Berg et al., 1996) had signs of progressive mucosal inflammation, elongated colon, signs of rectal prolapse, and delayed GI transit time (Fig. 3, A–F). The myenteric plexus of *Il10*$^{-/-}$ mice was characterized by a combination of neuronal loss and increased density of the nerve fiber network (Fig. 3. G–L). This could possibly be explained by ongoing neurogenesis, with the rate of neuronal loss exceeding that of neuronal replacement, although this has not been experimentally tested.

We then quantified the extent of intestinal innervation in the inflamed and noninflamed colon regions surgically resected from the same patients with CD and in non-IBD noninflamed controls. A significant increase in the density of HLA-DR$^+$ cells was found in the mucosa of patients with CD as compared to non-IBD controls, with the highest HLA-DR$^+$ cell density in inflamed CD regions (Fig. 3, M and O), consistent with the degree of inflammation determined macroscopically. The density of βIII-tubulin$^+$ nerve fibers was higher in CD samples as compared to non-IBD controls, and the density in the inflamed CD regions was higher than in noninflamed CD regions. The neuron density in the enteric ganglia was also significantly increased in the inflamed CD samples (Fig. 3, N and O), consistent with our findings in mice. Collectively, these data provide evidence of substantial ENS remodeling in murine progressive and human refractory colitis caused by IBD.

Monocyte-derived MMs with neuron-associated gene signature expand in the myenteric plexus in response to colitis

The cellular mechanisms driving colitis-induced ENS remodeling are not known. Macrophages in other organ systems have been shown to orchestrate biological processes relevant to tissue remodeling, including the safe disposal of cell debris through efferocytosis and the release of regulatory mediators and growth factors (Park et al., 2022). This led us to investigate whether ENS-associated MMs (Muller et al., 2014; Viola et al., 2023; De Schepper et al., 2019; Gabanyi et al., 2016; Matheis et al., 2020) mediate colitis-induced ENS remodeling.

Quantification of MMs in the myenteric plexus at early and late time points of 3×DSS colitis revealed a transient increase in their number (Fig. 4, A–C), suggesting an external source. Tissue macrophages differ in their developmental origins, arising either from embryonic progenitors (e.g., brain microglia) or from monocytes (Bleriot et al., 2020) (e.g., intestinal mucosal macrophages) (Bogunovic et al., 2009; Bain et al., 2014; De Schepper et al., 2019; Koscso et al., 2020). In contrast, MMs were highlighted to be of a mixed origin (Viola et al., 2023; De Schepper et al., 2019). Still, the MM diversity and origins in colitis have not been sufficiently studied. To address it, a two-step approach was adopted wherein single-cell RNA-sequencing (scRNA-seq) analysis of the normal myenteric plexus was first performed to identify potential MM subsets at steady state. Second, using the scRNA-seq–defined MM clusters as reference, CD45$^+$CD11b$^+$CD16/32$^+$ MM subsets were then subjected to fluorescence-activated cell sorting (FACS) and followed by RNA-seq analysis to establish gene signatures of control and DSS MM subsets. Accordingly, as per step 1, muscularis externa from the normal adult mouse colon was transcriptionally profiled at a single-cell level. We identified 20 cell clusters of 13 distinct cell types (in total 34,417 cells), including clusters of 6,929 MMs and 1,548 myenteric neurons, thus creating a comprehensive dataset to study MMs and their interaction with enteric neurons (Fig. S4 A and Table S1). Cell cluster analysis revealed significant cellular heterogeneity of MMs that were subdivided into five major clusters of *Csf1r*$^+$*Flt3*$^-$ cells (Fig. S4 B). Slingshot analysis of five MM clusters predicted the MM1 cluster that co-expressed the highest levels of monocyte-specific markers *Ccr2* and *Ly6c2*, as well as fibronectin (*Fn1*), to be an immediate monocyte descendant and the last common ancestor for the MM2-5 clusters (Fig. 4, D and E; and Fig. S4 C). However, the MM5 cluster also expressed the markers of self-maintaining monocyte-independent macrophages *Lyve1*, *Timd4*, and *Folr2* (Dick et al., 2022) (Fig. 4 E and Fig. S4 C).

Next, in step 2, to link the scRNA-seq–defined MM1–5 clusters to flow cytometry–defined MM subsets, we identified five major MM populations by flow cytometry based on their differential expression of monocyte/macrophage-specific markers *Ccr2*-RFP, Ly6c, *Cx3cr1*-GFP, and MHCII (Fig. 4, F and G; and Fig. S4, D and E) and purified the most numerous MM2, MM3, MM4, MM5 subsets from normal colon, and MM1, MM2, MM3, and MM4 subsets from inflamed colon using four-way FACS followed by RNA-seq of each subset (Fig. 4 H). The phenotypes and gene signatures of MM subsets sorted from normal colon closely resembled the gene signatures of MM clusters defined by scRNA-seq (Fig. 4. E–H). Quantitively, the MM1 (CCR2$^+$Ly6c$^+$MHCII^{lo}) and MM2 (CCR2$^+$Ly6c$^+$MHCII$^+$) subsets, also expressing *Ccr2, Ly6c2 and Fn1*, were negligible in the control group but expanded >10-fold upon colitis; the numbers of the MM3 (CCR2$^+$Ly6c$^-$MHCII$^+$), MM4 (CCR2$^-$Ly6c$^-$MHCII$^+$), and MM5 (CCR2$^-$Ly6c$^-$MHCII$^-$) subsets either did not significantly change or were reduced upon colitis (Fig. 4 I and Fig. S4 E) reflecting the proportional shift toward the newly recruited monocyte-derived populations (MM1 and MM2). Although the monocyte marker Ly6c covered 65% of CCR2$^+$ MMs in the same DSS mice (Fig. S4, E and F), an increase in Ly6c$^+$ MM counts positively correlated with CCR2$^+$ MM counts (Fig. S4 G and Fig. 4 I). Therefore, in subsequent experiments where the use of *Ccr2*-RFP transgene was not feasible, the Ly6c antibody was used as a substitute for *Ccr2*-RFP. Confocal microscopy of the colonic

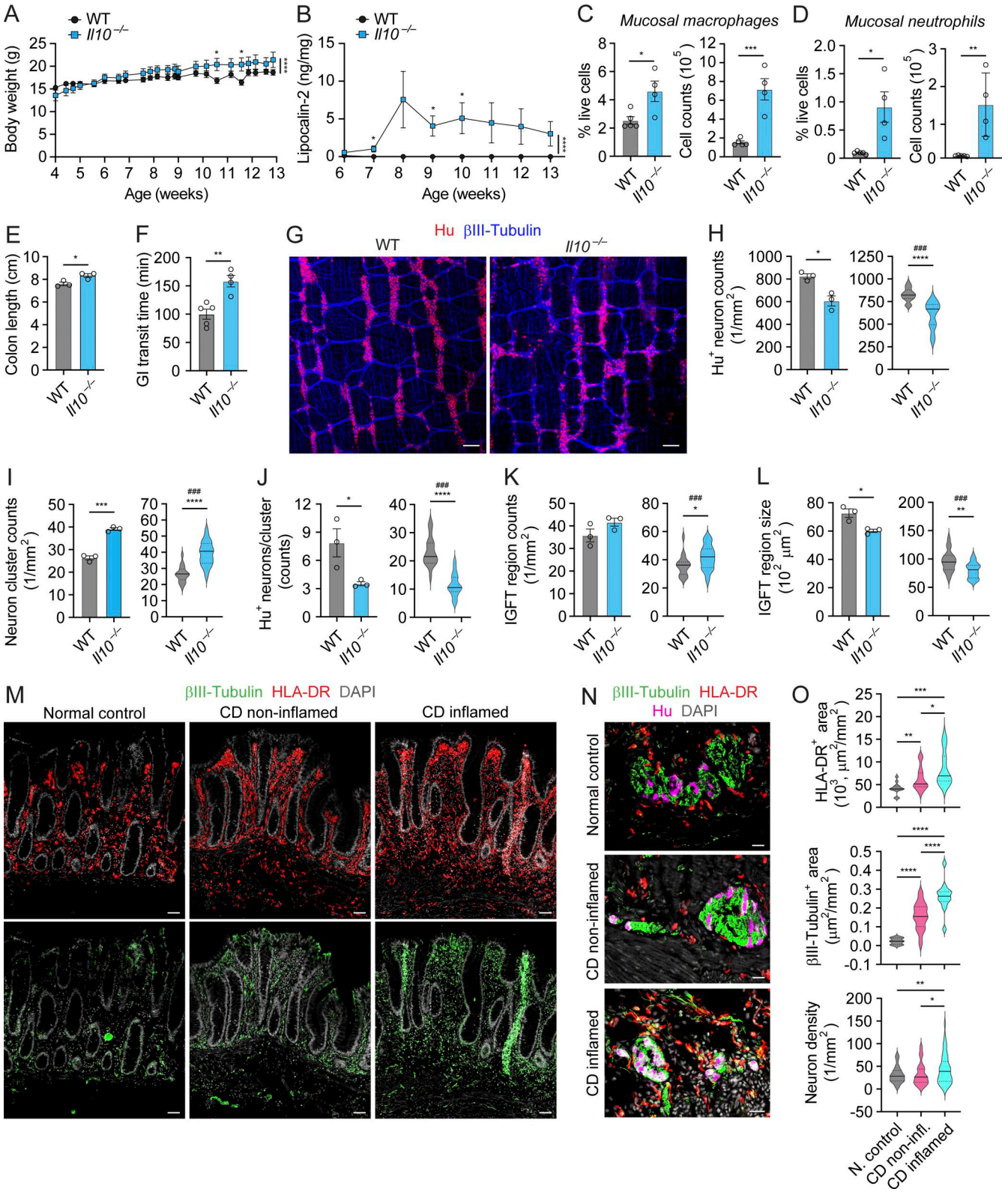

Figure 3. **ENS is remodeled in *Il10*$^{-/-}$ mice with progressive colitis and in human colon with refractory IBD. (A)** Body weight in *Il10*$^{-/-}$ mice from 4 wk of age until they developed rectal prolapse and in WT littermates (n = 5 per group). **(B)** Fecal lipocalin-2 in *Il10*$^{-/-}$ and WT mice, measured by ELISA (n = 5 per group). **(C)** Percentage of total viable cells (left) and absolute cell counts (right) of colonic mucosal macrophages in 13-wk-old *Il10*$^{-/-}$ and WT mice, quantified by FC (WT, n = 5; *Il10*$^{-/-}$, n = 4). **(D)** Percentage of total viable cells (left) and absolute cell counts (right) of colonic mucosal neutrophils in 13-wk-old *Il10*$^{-/-}$ and WT mice, quantified by FC (WT, n = 5; *Il10*$^{-/-}$, n = 4). **(E)** Colon length in 13-wk-old *Il10*$^{-/-}$ and WT mice (n = 3 per group). **(F)** GI transit in 13-wk-old *Il10*$^{-/-}$ and WT mice (WT, n = 5; *Il10*$^{-/-}$, n = 4). **(G)** Confocal images of colonic myenteric plexus from 13-wk-old *Il10*$^{-/-}$ and WT mice stained with Hu (neuronal somas) and βIII-tubulin (nerve fibers) antibodies. Images are representative of 13-wk-old *Il10*$^{-/-}$ and WT mice (n = 3 per group). Scale bars, 100 µm. **(H–J)** Changes in colonic

myenteric ganglia displayed in G of mice described in A showing (H) total counts of Hu$^+$ neurons, (I) counts of neuron clusters, and (J) counts of Hu$^+$ neurons per cluster, quantified by confocal microscopy. Data are shown as the mean value per mouse per group (left, n = 3 per group) or as distribution of pooled values generated from analysis of 6–10 fields of view per mouse per group (right). **(K and L)** Changes in nerve fiber architecture of colonic myenteric plexus displayed in G of mice described in A, showing (K) counts of IGFT regions and (L) area of IGFT regions, quantified by confocal microscopy. Data are shown as the mean value per mouse per group (left, n = 3 per group) or as distribution of pooled values generated from analysis of 6–10 fields of view per mouse per group (right). **(M)** Confocal images of large bowel mucosa in transmural specimens surgically resected from patients with CRC (normal adjacent region—control) and CD (noninflamed and inflamed regions), stained with βIII-tubulin (nerve fibers), HLA-DR (including macrophages), and Hu (neuronal somas) antibodies, and DAPI (nuclei). Images are representative of CRC (n = 3), CD noninflamed (n = 3), and CD inflamed (n = 2) tissue samples. Scale bars, 100 µm. **(N)** Confocal images of myenteric ganglia from the same tissue cross-sections as in M. Images are representative of CRC (n = 3), CD noninflamed (n = 3), and CD inflamed (n = 2) tissue samples. Scale bars, 50 µm. **(O)** HLA-DR$^+$ cells (top, to depict inflammation), βIII-tubulin$^+$ nerve fibers (mid, to depict innervation), and Hu$^+$ neuronal soma density in βIII-tubulin$^+$ ganglia (bottom) in the experiment described in M and N, quantified by confocal microscopy. Data are shown as distribution of pooled values generated from analysis of 6–14 ROIs per patient tissue sample (top and mid-panels) or as distribution of pooled values indicating all ganglia analyzed per patient tissue sample. N., normal; non-infl., noninflamed. All graphs show the mean ± SEM, n—mouse or patient. Data are representative of two independent experiments with similar results (A–L). Statistical analyses: unpaired Student's t test (C–O), multiple t test (A and B), and two-way ANOVA for multiple comparisons (A and B), *P ≤ 0.05, **P ≤ 0.01, ***P ≤ 0.001, and ****P ≤ 0.0001. # above pooled data in violin plots (right, H–L) indicates empirical P values calculated by the Nested Leave-One-Out Jackknife strategy, where ###P < 0.001.

muscularis externa confirmed that CCR2$^+$ MMs expanded specifically within the myenteric plexus following colitis (Fig. 4 J).

MMs are a dominant immune cell type in the normal myenteric plexus (Muller et al., 2014). CD3$^+$ T cells, shown to participate in the killing of enteric neurons infected with neurotropic viruses (White et al., 2018), were rare in the myenteric plexus of both control mice and mice with colitis (Fig. S4 H). The total numbers of muscularis polymorphonuclear cells (M-PMNs) and muscularis T cells (M-T cells) were increased; however, MM dominance remained after colitis induction (Fig. S5, A and B).

To determine the contribution of monocytes to the total MM pool during colitis, we fate-mapped monocyte-derived MMs (Mo-MMs) in *Ccr2*$^{ER\text{-}Cre}$*R26*-STOP$^{fl/fl}$tdTomato (*Ccr2*:tdTomato) mice continuously treated with tamoxifen under water and DSS conditions (Fig. S5 C). Four days after beginning the tamoxifen treatment, nearly 100% of blood Ly6c$^+$ inflammatory monocytes were tdTomato$^+$ regardless of colitis (Fig. S5 D). Four and a half weeks (33 days) later, over 90% of Ly6c$^+$ MM1 and MM2, and ∼75% of Ly6c$^-$ MM3 and MM4 subsets were labeled with tdTomato; i.e., they were mostly monocyte-derived. The rate of MM labeling with tdTomato was only slightly lower in control mice (Fig. 4 K). Confocal microscopy showed similar results—97% of tdTomato$^+$ cells in water-treated mice and 82% in DSS-treated mice colocalized with MHCII$^+$ cells (Fig. S5 E). In contrast, the rate of tdTomato$^+$ cells among MM5 (Ly6c$^-$MHCII$^-$) was only 10% in control mice and 40% in DSS mice, suggesting their low turnover rate and/or low input from CCR2$^+$ monocytes (Fig. 4 K), consistent with their *Lyve1*-, *Timd4*-, and *Folr2*-positive gene signatures. Collectively, our analysis showed that colitis leads to myenteric plexitis with a preferential expansion of monocyte-derived CCR2$^+$ MMs.

To predict the outcome of plexitis, we performed gene expression analysis of MM subsets. First, we identified differentially expressed genes (DEGs) in water control and DSS-inflamed MM subsets (Fig. S5 F; and Tables S2 and S3). Gene pathways upregulated by MM1 subset following colitis included "cell–cell adhesion", "collagen degradation", "extracellular matrix organization", "myelin sheath formation", "negative regulation of neuron apoptotic process", "dopaminergic neuron differentiation", and "pathways of neurodegeneration (multiple diseases)". Gene pathways upregulated by a more differentiated MM4 subset included "efferocytosis", "microglial cell activation", "negative regulation of cell death", "positive regulation of neuron apoptotic process", "positive regulation of neuron differentiation", "inflammatory response", and "antigen processing and presentation" (DSS MM subset pathway enrichment up- and downregulated relative to all other subsets is shown in Table S4).

Using an earlier gene array dataset of intestinal macrophages (Muller et al., 2014; Miller et al., 2012), we established the MM core gene signature, which included genes potentially relevant to ENS remodeling based on a literature search and whose expression was significantly higher in MMs than in mucosal macrophages (Fig. S5 G). Comparison of core MM signature genes and additional microglia-specific genes (common for both MMs and mucosal macrophages) across MM subsets at steady state and during colitis revealed specific candidates potentially involved in ENS remodeling (Fig. S5, H–J; DSS MM subset identity signatures up- and downregulated relative to all other subsets are shown in Table S5). Finally, we compared the expression of common inflammatory and anti-inflammatory genes among MM subsets at steady state and during colitis. Monocyte-derived MM1 and MM4 subsets upregulated the expression of both pro-inflammatory (*Il1b*, *Osm*, *Tnf*) and anti-inflammatory (*Arg1*, *Arg2*, *Il10*) genes in a manner that did not align with pro-inflammatory "M1" and alternative "M2" MMs highlighted earlier (Gabanyi et al., 2016) (Fig. S5 K).

CellChat analysis applied to the scRNA-seq dataset identified ligand–receptor pair interactions between the two most distinct monocyte-derived MM1 or MM4 clusters and myenteric neurons (combined clusters 12 [Morarach et al., 2021] and 13 [Kulkarni et al., 2023]; Fig. 4 L) at steady state, predicting that Mo-MMs engage in functional crosstalk with enteric neurons. Although the ligand–receptor pairs for MM1 and MM4 clusters overlapped, some ligand–receptor pairs were unique to either MM1 (e.g., *Sema3c-Plxnd1* [Kim et al., 2024] and *Fn1-Itgav/b1* [Reichardt and Tomaselli, 1991] reported to be required for axonal growth and synapse formation) or MM4 (e.g., *App-Cd74* and *Gas6-Mertk* likely involved in the regulation of repair and clearance of injured neurons [Matsuda et al., 2009; Healy et al.,

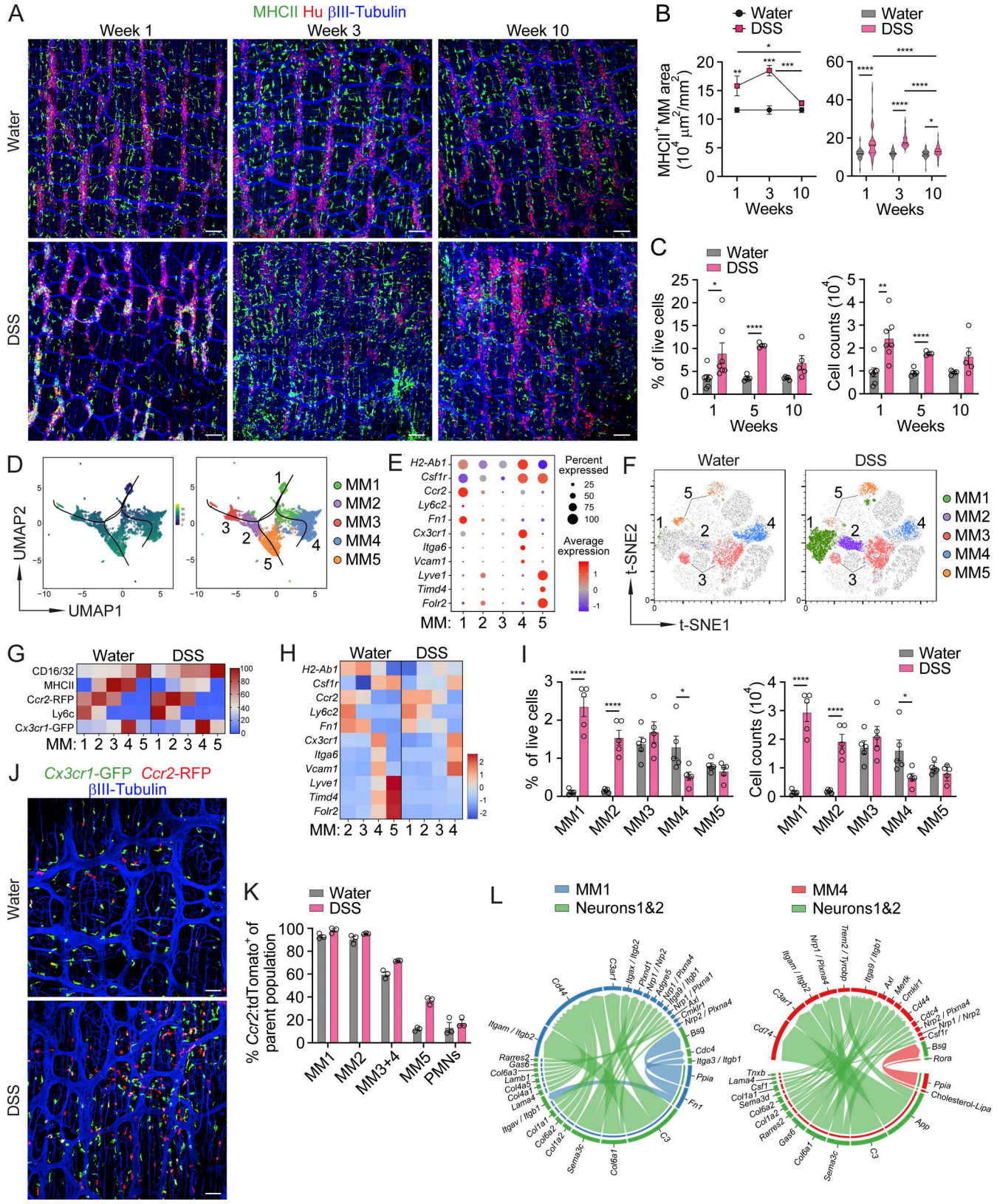

Figure 4. **CCR2⁺ monocyte-derived MMs expand in the myenteric plexus in response to colitis. (A)** Confocal images of colonic myenteric plexus isolated from 3×DSS- or water-treated mice (as in Fig. 1 G but with MHCII channel ON). Images are representative of control (n = 5–10) and DSS (n = 4–13) for each time point. Scale bars, 100 µm. **(B)** Total MHCII⁺ area in the colonic myenteric plexus shown in A, based on confocal microscopy. Data are shown as the mean value per mouse (left, control, n = 5–10; DSS, n = 4–13) or as distribution of pooled values generated from analysis of 4–9 fields of view per mouse (right). **(C)** Percentage of total viable cells (left) and absolute cell counts (right) of colonic MMs from mice described in A, quantified by FC (control, n = 5–7; DSS, n = 4–

7). **(D)** Predicted developmental trajectory of five scRNA-seq MM clusters in normal colon determined by slingshot analysis, shown as pseudotime (left) and MM clusters (right). The scRNA-seq dataset is described in Fig. S4. **(E)** scRNA-seq dot heatmap showing expression of 11 marker genes across five MM clusters displayed in D. Color denotes the average expression level, and size represents the percentage of cells expressing the indicated genes. **(F)** FC t-SNE plots showing MM subsets of colonic muscularis single-cell suspensions from water- or 1×DSS-treated (2.75%) *Ccr2*$^{RFP/+}$*Cx3cr1*$^{GFP/+}$ reporter mice at week 1 (gated on CD45$^+$CD11b$^+$CD16/32$^+$ viable cells). **(G)** MFI heatmap showing expression of five MM-specific protein markers in the same FC experiment as in F. **(H)** RNA-seq heatmap showing expression of 11 marker genes by MM subsets identified in E, isolated by four-way FACS from 1×DSS- or water-treated *Ccr2*$^{RFP/+}$*Cx3cr1*$^{GFP/+}$ mice at week 1 in the same experiment as in F and G. **(I)** Percentage of total viable cells (left) and absolute counts (right) of colonic MM subsets shown in F–H, quantified by FC (n = 5 per group). **(J)** Confocal images of colonic myenteric plexus from 1×DSS- or water-treated *Ccr2*$^{RFP/+}$*Cx3cr1*$^{GFP/+}$ mice at week 1, stained with antibodies to GFP (CX3CR1$^+$ cells), RFP (CCR2$^+$ cells), and βIII-tubulin (nerve fibers). Scale bars, 50 µm. **(K)** Percentage of monocyte-derived tdTomato$^+$ cells among colonic MM subsets and PMNs from tamoxifen- and 1×DSS- (3%) or water-treated *Ccr2*$^{ER\text{-}Cre}$*R26*-STOP$^{fl/fl}$tdTomato mice at week 5, quantified by FC (n = 3 per group). **(L)** Wheel plots showing top ligand–receptor pair interactions between colonic myenteric neurons and monocyte-derived MM1 (left) or MM4 (right) clusters predicted by CellChat analysis of the scRNA-seq dataset described in Fig. S4. All graphs show the mean ± SEM, n—mouse. Data in A–C, F, G, and I are representative of at least three independent experiments, and data in J and K are representative of at least two independent experiments with similar results. Statistical analyses: unpaired Student's t test (I), multiple t test (C), and two-way ANOVA for multiple comparisons (B), *P ≤ 0.05, **P ≤ 0.01, ***P ≤ 0.001, and ****P ≤ 0.0001. MFI, mean fluorescence intensity.

2016]) clusters, suggesting that following recruitment into the myenteric plexus, monocytes represented by MM1 cluster engage in functional interactions with enteric neurons and acquire additional neuron-associated functions while transitioning to terminally differentiated tissue macrophages represented by MM4 cluster. To assess the relevance of the Mo-MM–neuron crosstalk in the colitis setting, we selected the genes that were significant for MM–neuron communication in the normal colon based on CellChat (Fig. 4 L) and evaluated their statistical enrichment in a co-expression network we generated from bulk RNA-seq of mouse colon of DSS mice and water controls from our prior study (Peters et al., 2017; Peters et al., 2023). This analysis (Table S6) established that the MM- and neuron-interacting genes from the single-cell mouse colon dataset are conserved in DSS colitis.

In summary, DSS-induced mucosal inflammation leads to extensive monocyte recruitment into the ENS microanatomical compartment, located outside the mucosa. Monocytes sequentially differentiate into functionally distinct CCR2$^+$ and CCR2$^-$ ENS-associated MMs predicted to engage in functional crosstalk with enteric neurons by acquiring microanatomical compartment-specific tissue remodeling and microglia-like properties in addition to inflammatory, immunoregulatory, and antigen-presenting functions typical of mucosal macrophages. Therefore, Mo-MMs are the most probable immune cell type responsible for ENS remodeling upon colitis.

Mo-MMs recruited by myenteric neurons via the CCL2 axis facilitate ENS remodeling

To test the predicted role of MMs in ENS remodeling *in vivo*, we assessed the dynamic changes in neuron–MM interactions during the active and receding stages of colitis. Mice were treated with one cycle of DSS (to have a better controlled system) or water, and the interactions between MMs (MHCII$^+$) and myenteric neurons (Hu$^+$) were quantified by three-dimensional two-photon microscopy. MHCII was kept as a reliable marker for Mo-MMs in tissue immunofluorescence analyses (Fig. S5 E). Like in prior experiments (Fig. 1, H–J and Fig. 2 A), the initial loss of neurons observed at week 1 was followed by the recovery of their number (Fig. 5, A and B). However, the peak of MM expansion (week 2) was delayed as compared to the peak of neuronal loss (week 1), suggesting that MM expansion is secondary to the initial neuronal loss (Fig. 5, A and B). At the peak of MM expansion, there were increased contacts between MMs and neurons and increased neuronal (Hu) signal inside MMs (MHCII), reflecting MM recruitment into the myenteric ganglia and uptake of neurons by MMs (Fig. 5, A and B; and Videos 1, 2, and 3).

Next, we sought to identify an ENS-associated cell type that plays a role in recruiting monocytes into the ENS niche. In the myenteric plexus, only enteric neurons can directly access the mucosa through projected axons (Margolis et al., 2016; Melo et al., 2020; Fung et al., 2025), and myenteric sensory neurons show increased excitability in the inflamed colon (Linden et al., 2003). We therefore hypothesized that biological changes in enteric neurons should be most upstream to other changes in the microanatomical compartment of the myenteric plexus, and that enteric neurons are the most likely cell type to recruit MMs. Indeed, FACS-purified CD90$^+$CD24$^+$ myenteric neurons and not other stromal cells expressed CCR2 ligand *Ccl2* at baseline and upregulated it further upon colitis (Fig. 5 C). To assess CCL2 expression in myenteric neurons within intact tissue, we used *Ccl2*$^{fl/fl}$ RFP reporter mice, which express RFP under the control of the *Ccl2* promoter. RFP expression was significantly elevated during colitis, primarily localized to Hu$^+$ neuronal somas (Fig. 5 D). Nerve fibers that can originate from both extrinsic and enteric neurons were negative for RFP, thus excluding extrinsic neurons as a potential source of myenteric CCL2. Hu$^-$RFP$^+$ cells were less frequent and consisted of MHCII$^+$ MMs and other nonneuronal intraganglionic cells (Fig. 5 D). In contrast, systemic LPS injection triggered a preferential CCL2 response in nonneuronal cells (both MHCII$^+$ and MHCII$^-$; Fig. S6 A), supporting the idea that, in early colitis, enteric neurons are the primary cell type transmitting inflammatory signals from the mucosa to the myenteric plexus. In addition, CCL2 immunoreactivity was detectable in myenteric neurons of the inflamed human CD colon (Fig. S6 B).

To provide the *in vivo* evidence of the neuron-to-monocyte CCL2 signaling axis, we conditionally depleted *Ccl2* in enteric neurons *in vivo*. To avoid possible developmental ENS defects caused by early MM loss (Viola et al., 2023), we used SLICK-H$^{ER\text{-}Cre}$ mice as a tamoxifen-inducible transgenic Cre line specific to neurons (Young et al., 2008) (Fig. S7, A–E). Currently, no other

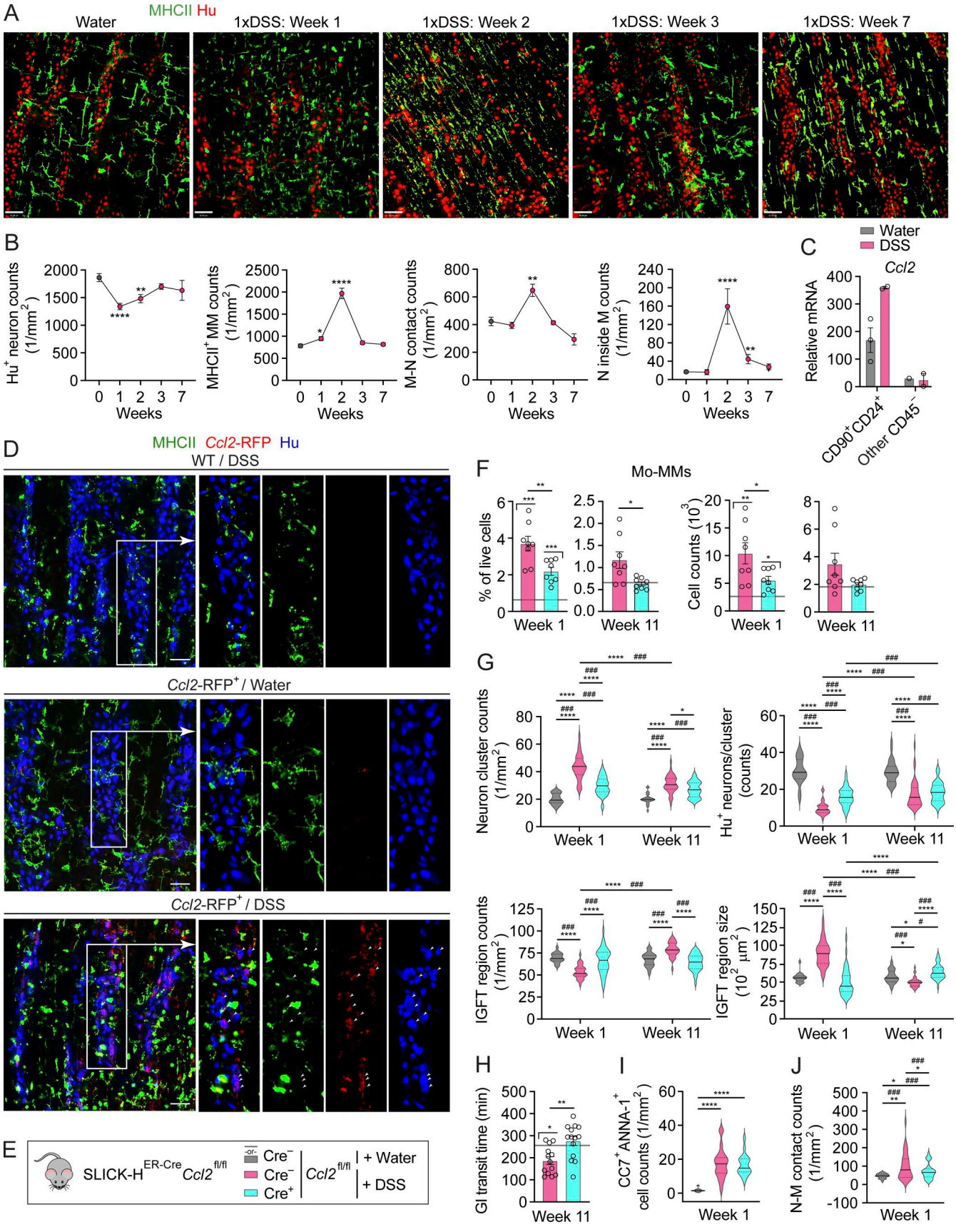

Figure 5. **Enteric neuron-derived CCL2 facilitates pathological myenteric plexus remodeling and postinflammatory GI dysmotility by excessive recruitment of monocytes in response to colitis. (A)** Two-dimensional projections of three-dimensional two-photon images of colonic myenteric plexus

from 1×DSS- (3%) or water-treated mice, stained with MHCII (MMs) and Hu (neuronal somas) antibodies. Images are representative of control (n = 3) and DSS (n = 1–3) mice for each time point. Scale bars, 100 µm. **(B)** Myenteric neurons, MMs, their interactions, and neuronal uptake by MMs quantified by two-photon microscopy in the experiment described in A (control, n = 3; DSS, n = 1–3). Data are shown as the mean of pooled values generated from analysis of 5–18 fields of view per group. **(C)** *Ccl2* expression by qPCR in $CD45^-CD90^+CD24^+$ myenteric neurons and other $CD45^-$ stromal cells FACS-purified from colonic muscularis of 1×DSS- or water-treated mice at week 1, normalized to the housekeeping gene *Actb* (control, n = 1–3; DSS, n = 2, where n = independent cell sorting). **(D)** Confocal images of colonic myenteric plexus from 1×DSS (2.5%)- or water-treated *Ccl2*-$RFP^{fl/fl}$ and WT mice at week 1, stained with MHCII (MMs), tdTomato (*Ccl2*-RFP), and Hu (neuronal somas) antibodies. White arrowheads indicate $CCL2^+Hu^+$ neurons. Scale bars, 50 µm. **(E)** Experimental groups used in F–J, analyzed at weeks 1 and 11 after starting DSS. **(F)** Percentage of total viable cells (left) and absolute cell counts (right) of colonic Mo-MMs in tamoxifen- and 3×DSS-treated (2.15%) SLICK-$H^{ER\text{-}Cre}Ccl2^{fl/fl}$ (Cre^+) and $Ccl2^{fl/fl}$ littermates (Cre^-), quantified by FC (DSS Cre^- and Cre^+, n = 8 per group). Baseline shows the mean value for tamoxifen- and water-treated $Ccl2^{fl/fl}$ littermates (Water Cre^-, n = 5–6). P values above each column indicate statistical differences against baseline. **(G)** Structural changes in the colonic myenteric plexus of mice described in F, showing counts of neuron clusters, counts of Hu^+ neurons per cluster, and counts and area of IGFT regions, quantified by confocal microscopy (DSS Cre^- and Cre^+, n = 7–8 per group; Water Cre^- baseline, n = 4–6). Data are shown as distributions of pooled values generated from analysis of 5 fields of view per mouse. **(H)** GI transit in tamoxifen- and 3×DSS-treated Cre^- and Cre^+ littermates at week 11 after starting DSS (DSS Cre^- and Cre^+, n = 13–14 per group; Water Cre^- baseline, n = 9). P values above each column indicate statistical differences against baseline. **(I)** Counts of $CC7^+ANNA\text{-}1^+$ colonic myenteric neurons analyzed at week 1, quantified by confocal microscopy (DSS Cre^- and Cre^+, n = 4 per group; Water Cre^- baseline, n = 2). Data are shown as a distribution of pooled values generated from analysis of 5–6 fields of view per mouse. **(J)** Interactions (contacts) between $MHCII^+$ MMs and myenteric Hu^+ neurons analyzed at week 1, quantified by confocal microscopy (DSS Cre^- and Cre^+, n = 7–8 per group; water Cre^- baseline, n = 4). Data are shown as distributions of pooled values generated from analysis of 5 fields of view per mouse. All graphs show the mean ± SEM, n—mouse, unless stated differently. Data are representative of at least two independent experiments with similar results. Statistical analyses: unpaired Student's t test (B, F, H, I, and J) and two-way ANOVA for multiple comparisons (G), *P ≤ 0.05, **P ≤ 0.01, ***P ≤ 0.001, and ****P ≤ 0.0001. # above pooled data in violin plots (right, G) indicates empirical P values calculated by the Nested Leave-One-Out Jackknife strategy, where #P < 0.5–0.01, and ###P < 0.001.

Cre line has been described that can target the majority of enteric neurons in an inducible manner. The specificity of the SLICK-$H^{ER\text{-}Cre}$ mouse model to myenteric neurons but not enteric glia was confirmed in SLICK-$H^{ER\text{-}Cre}$*R26*-$STOP^{fl/fl}$tdTomato mice (Fig. S7, C–E). Successful tamoxifen-induced (as in Fig. 2 B) *Ccl2* depletion in enteric neurons of SLICK-$H^{ER\text{-}Cre}Ccl2^{fl/fl}$ ($Ccl2^{\Delta Neu}$) mice was also confirmed (Fig. S6 C). Next, $Ccl2^{\Delta Neu}$ mice and their $Ccl2^{fl/fl}$ littermates were given 3×DSS and analyzed at early acute and late postinflammatory time points (Fig. 5 E). The depletion of *Ccl2* in enteric neurons reduced the number of recently recruited $Ly6c^+$ Mo-MMs both at early and at late time points (Fig. 5 F and Fig. S6 D), while having no significant impact on M-PMNs and M-T cells (Fig. S6, E and F). There were also no significant difference in mucosal inflammation (Fig. S6, G–I) and blood monocyte counts (Fig. S6 J) between the *Ccl2*-sufficient and *Ccl2*-deficient groups. These data demonstrate that during colitis enteric neurons recruit monocytes into the myenteric plexus by upregulating CCL2 production.

According to our scRNA-seq data supported by flow cytometry analysis presented in Fig. 4, no cell types in the myenteric plexus other than MMs express *Ccr2*. Therefore, $Ccl2^{\Delta Neu}$ mice provided a Mo-MM–reduced model with an intact mucosal macrophage compartment for functional studies addressing the overall role of inflammatory Mo-MMs in colitis-associated ENS remodeling. Next, ENS remodeling was assessed in the same cohort of mice described above (Fig. 5 E). Neuron counts per field are a highly variable readout (Fig. 1 H), necessitating a larger sample size and high-power analysis. Therefore, we focused on more sensitive measures of neuronal loss based on neuronal density and pooled values. We found that both Mo-MM–sufficient and Mo-MM–defficient mice experienced neuronal loss during active colitis. However, the myenteric plexus of $Ccl2^{\Delta Neu}$ mice showed less severe ganglion fragmentation, as evidenced by fewer neuronal clusters and more neurons per cluster, indicating it was less affected (Fig. 5 G; and Fig. S8, A and B). This was consistent with less disrupted nerve fiber network in $Ccl2^{\Delta Neu}$ mice as their IGFT region counts and IGFT region size were more similar to control mice without colitis (Fig. 5 G; and Fig. S8, A and B). In the post-colitis phase, we observed a partial recovery of neuronal counts and increased nerve fiber density in Mo-MM–sufficient mice, consistent with neurogenesis, while Mo-MM–deficient $Ccl2^{\Delta Neu}$ mice remained more similar to control mice without colitis (Fig. 5 G; and Fig. S8, A and B). These data suggest that reduced recruitment of Mo-MMs diminished the early neuronal degeneration and subsequent ENS remodeling in the myenteric plexus. In line with reduced ENS remodeling, $Ccl2^{\Delta Neu}$ mice exhibited GI transit that was similar to water-treated control mice, indicating protection from postinflammatory GI dysmotility (Fig. 5 H).

DSS and infectious colitis have been shown to increase programmed cell death of enteric neurons (Gulbransen et al., 2012; Matheis et al., 2020; Forster et al., 2025). Because Mo-MMs upregulate inflammatory gene expression during colitis (Fig. S5 K), we asked about their role in early neuronal apoptosis. We saw an increase in cleaved caspase-7 $(CC7)^+$ apoptotic neurons in mice with early colitis as compared to no colitis control, but there was no significant difference in the frequency of $CC7^+$ neurons between $Ccl2^{\Delta Neu}$ and $Ccl2^{fl/fl}$ groups with colitis (Fig. 5 I and Fig. S8 C). In contrast, the physical contact between MMs and myenteric neurons was reduced in the $Ccl2^{\Delta Neu}$ group (Fig. 5 J). This evidence supports our earlier findings (Fig. 5, A and B) and lends further credence to the idea that Mo-MMs contribute to the cleanup of damaged neurons, providing conditions for neuronal regeneration. Collectively, our data suggest that Mo-MMs recruited by myenteric neurons promote disproportionate ENS remodeling in response to colitis-induced ENS damage, thereby contributing to the pathogenesis of postinflammatory GI dysmotility.

Enteric neuron-intrinsic hypoxia stress response via HIF1α counterbalances colitis-induced recruitment of Mo-MMs and reduces ENS remodeling

The influx of inflammatory immune cells, their local proliferation, and elevated glycolysis during colitis increase oxygen

consumption, leading to suboptimal oxygen levels in the tissue termed "inflammatory hypoxia" as opposed to "physiological hypoxia" present in the normal colon (Taylor and Colgan, 2017). We hypothesized that enteric neurons, in response to hypoxic stress, may activate an adaptation program to limit further monocyte recruitment and mitigate the exacerbation of hypoxia. To test that enteric neurons are hypoxic upon colitis, control mice and mice with early DSS colitis were injected with the nitroimidazole compound EF5, which specifically labels hypoxic cells when injected *in vivo*, or vehicle. In the inflamed colons of DSS-treated mice, there was a significant increase in $EF5^+$ (i.e., hypoxic) neurons along with the $EF5^+$ epithelium, which served as an internal positive control (Taylor and Colgan, 2017) (Fig. 6, A and B). Thus, enteric neurons become hypoxic upon colitis.

The hypoxia-inducible factor (HIF) pathway regulates the expression of a broad range of genes that facilitate cell adaptation to hypoxic stress. HIFs function as heterodimers composed of an oxygen-regulated alpha subunit and a stably expressed beta subunit. HIF1α is ubiquitously expressed, and in the brain, it was shown to regulate the neuronal response to hypoxia (Sharp and Bernaudin, 2004). Under normoxia, cytoplasmic HIF1α is continuously subjected to hydroxylation and proteasomal degradation with the help of the von Hippel–Lindau (VHL) E3 ubiquitin ligase complex (Fig. 6 C). During hypoxia, HIF1α is not degraded and thus translocates into the nucleus, where it dimerizes with HIF1β and binds to HIF-responsive elements in specific target genes (Dengler et al., 2014). One key target of this pathway is vascular endothelial growth factor α, which is positively regulated by HIF signaling (Forsythe et al., 1996; Sharp and Bernaudin, 2004) (Fig. 6 C). We therefore tested *Hif1a* and *Vegfa* expression in enteric neurons isolated from the myenteric plexus of mice at an early phase of DSS colitis and control mice, and found that colitis significantly upregulated neuronal *Hif1a* and *Vegfa* expression (Fig. 6, D and E). HIF1α was also detectable in the nuclei of myenteric neurons during colitis (Fig. S9 A). Thus, mucosal inflammation triggers the adaptation response to hypoxic stress in enteric neurons in addition to the inflammatory CCL2 response.

HIF1α binding site was found in the CCL2 promoter in primary fetal human astrocytes (Mojsilovic-Petrovic et al., 2007), but the functional link between hypoxia signaling and CCL2 expression in enteric neurons has not been established. To test the hypothesis that HIF1α signaling regulates *Ccl2* expression in enteric neurons during inflammation, we modeled chemical hypoxia *in vitro* by treating cultures of myenteric neurons isolated from adult mice (Zhang and Hu, 2021) (Fig. S9, B and C) with cobalt chloride ($CoCl_2$), a known stabilizer of HIF1α and activator of HIF signaling (Munoz-Sanchez and Chanez-Cardenas, 2019). To confirm that our *in vitro* hypoxia system is HIF1α-dependent, cultured myenteric neurons were treated with $CoCl_2$ in the presence of the HIF1α inhibitor PX-478 (Schwartz et al., 2009), and *Vegfa* expression was quantified by quantitative PCR (qPCR). $CoCl_2$ treatment upregulated *Vegfa* expression, but when combined with PX-478, *Vegfa* expression was reduced (Fig. S9 D).

Using this validated *in vitro* model system, we examined the role of the HIF pathway on *Ccl2* expression. Myenteric neurons cultured in the presence or absence of $CoCl_2$ were treated with pro-inflammatory stimuli LPS or IL-1β, both known as positive regulators of CCL2 expression in other cell types (Serbina et al., 2008; Serbina et al., 2012). We found that like primary enteric neurons (Fig. 5 C), cultured enteric neurons expressed detectable levels of *Ccl2* at baseline (Fig. S9 E) and significantly upregulated *Ccl2* expression upon LPS or IL-1β treatment. Triggering the HIF pathway with $CoCl_2$ reduced *Ccl2* expression both at baseline and upon stimulation (Fig. 6 F; and Fig. S9, F and G). Similar results were observed for CCL2 protein expression (Fig. 6 G). $CoCl_2$ treatment did not impact cell viability (Fig. S9 H) or significantly change baseline and induced *Il1a* and *Csf1* expression (Fig. S9, I and J), but it did induce *Vegfa* expression in the same cell cultures (Fig. S9 K). Furthermore, treatment with the HIF1α inhibitor PX-478 upregulated *Ccl2* expression in cultured enteric neurons (Fig. 6 H and Fig. S9 L). Collectively, our *in vitro* studies show that the HIF pathway negatively regulates CCL2 chemokine expression in enteric neurons.

To test the role of HIF pathway on enteric neuron-to-MM CCL2 axis *in vivo*, we treated mice with PX-478 or a vehicle control along with DSS and analyzed them at an early time point (Fig. 6 I). We found that enteric neurons from PX-478–treated mice with colitis upregulated more *Ccl2* (Fig. 6 J) and had more Mo-MMs (Fig. 6 K and Fig. S10 A) as compared to the vehicle-treated mice with colitis. In contrast, there was no difference in M-PMN numbers (Fig. S10 B) and mucosal inflammation (Fig. S11, A–C) between the groups. These results support our *in vitro* findings, demonstrating that the HIF pathway negatively regulates CCL2 expression in enteric neurons *in vivo* and reduces monocyte recruitment into the myenteric plexus.

To block HIF signaling in enteric neurons that would mimic PX-478 treatment, we generated transgenic SLICK-$H^{ER\text{-}Cre}$*Hif1a*$^{fl/fl}$ (*Hif1a*$^{\Delta Neu}$) mice that deplete HIF1α specifically in neurons when treated with tamoxifen (as in Fig. 2 B). To reinforce HIF signaling, we generated SLICK-$H^{ER\text{-}Cre}$*Vhl*$^{fl/fl}$ (*Vhl*$^{\Delta Neu}$) mice that deplete a negative regulator of HIF signaling *Vhl* (Fig. 6 C) in neurons upon tamoxifen treatment. And as a positive control, we developed SLICK-$H^{ER\text{-}Cre}$*Myd88*$^{fl/fl}$ (*Myd88*$^{\Delta Neu}$) mice to block the effect of LPS and IL-1β signaling that were used as CCL2 mimetics in the *in vitro* system. *Hif1a*$^{\Delta Neu}$ mice are expected to express more CCL2 in enteric neurons, while *Vhl*$^{\Delta Neu}$ and *Myd88*$^{\Delta Neu}$ mice are expected to have less CCL2 expression in enteric neurons. Similar to PX-478–treated mice, *Hif1a*$^{\Delta Neu}$ mice with active colitis had more Mo-MMs as compared to Cre^- mice (Fig. S10, C and D). In contrast, *Vhl*$^{\Delta Neu}$ and *Myd88*$^{\Delta Neu}$ mice with active colitis had fewer Mo-MMs as compared to Cre^- mice (Fig. 6 M; and Fig. S10, F, G, and I). *Hif1a*$^{\Delta Neu}$, *Myd88*$^{\Delta Neu}$, and *Vhl*$^{\Delta Neu}$ mice did not have significant differences in M-PMN numbers (Fig. S10, E, H, and J) and mucosal inflammation (Fig. S11, D–L), confirming that the effect that we see on Mo-MMs is myenteric plexus–restricted and neuron-driven. Together, these results demonstrate that enteric neurons under hypoxic stress employ HIF signaling to counterbalance the inflammation-mediated recruitment of monocytes into the ENS.

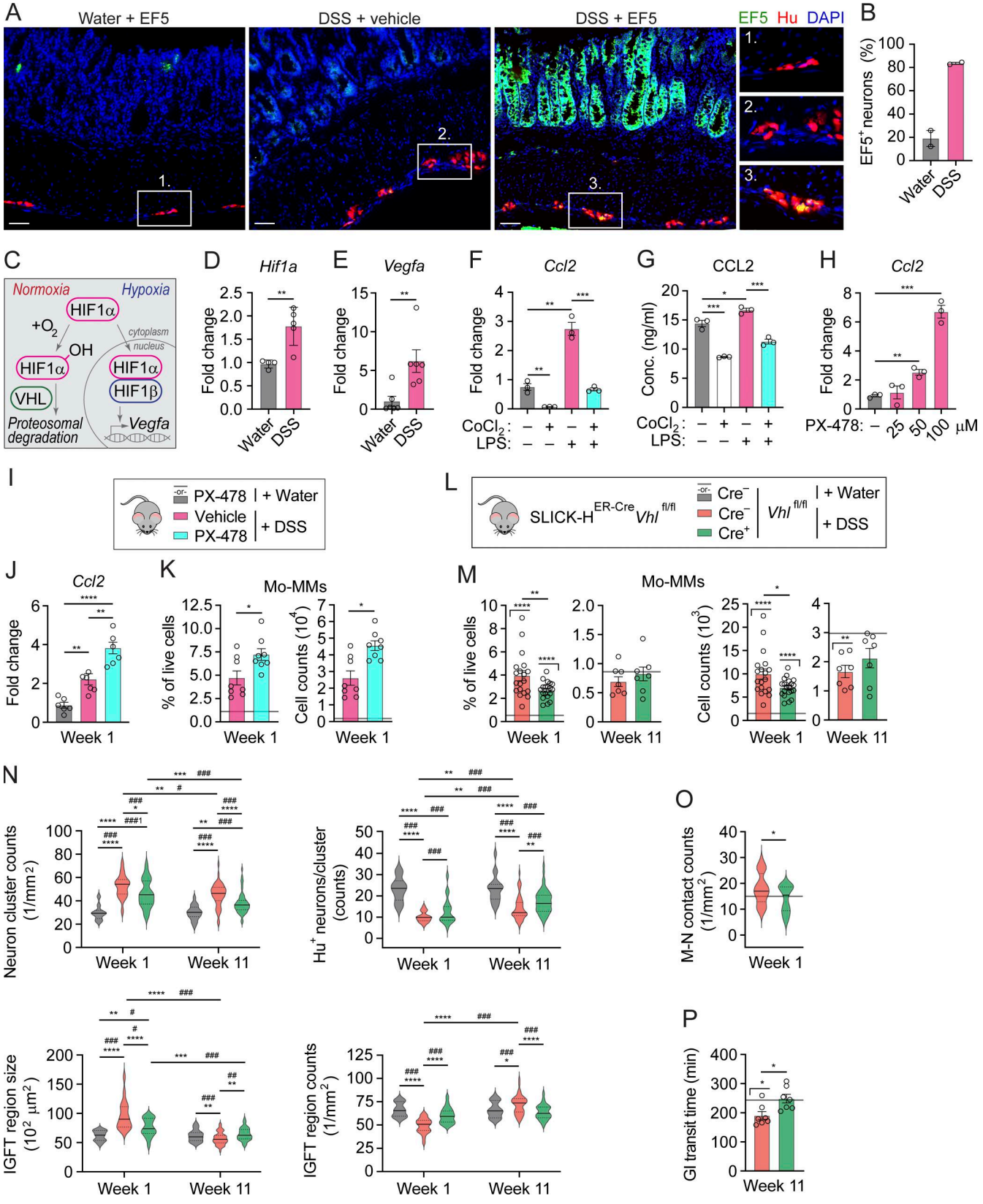

Figure 6. **Enteric neuron-intrinsic HIF1α signaling limits CCL2-driven monocyte recruitment and protects from myenteric plexus remodeling and postinflammatory GI dysmotility. (A)** Confocal images showing cross-sections of colons isolated from 1×DSS- (3.5%) or water-treated and EF5- or vehicle-injected WT mice at week 1, stained with EF5 (hypoxic cells) and Hu (neuronal somas) antibodies, and DAPI (nuclei). Scale bars, 50 µm. **(B)** Percentage of total EF5⁺ Hu⁺ hypoxic neurons in cross-sections of colons of mice described in A (n = 2 per group, n—cross-section of full-length colon Swiss roll). **(C)** Graphical summary of HIF signaling pathway. **(D)** *Hif1a* expression by qPCR in colonic myenteric neurons FACS-purified from 1×DSS- or water-treated mice at week 1,

normalized to *Actb* (n = 4–5 per group, n—independent cell sorting). **(E)** *Vegfa* expression by qPCR in colonic myenteric neurons FACS-purified from 1×DSS- or water-treated mice at week 1, normalized to *Actb*. (n = 6 per group, n—independent cell sorting). **(F)** *Ccl2* expression by qPCR in cultured adult colonic myenteric neurons treated with $CoCl_2$, LPS, or their combinations, normalized to *Actb* (n = 3 per group, n—replica wells in the same cell culture). **(G)** CCL2 concentration by ELISA in supernatants from cultured adult colonic myenteric neurons described in F (n = 3 per group, n—replica wells in the same cell culture). **(H)** *Ccl2* expression by qPCR in cultured adult colonic myenteric neurons treated with the HIF1α inhibitor PX-478 or vehicle, normalized to *Actb* (n = 3 per group, n—replica wells in the same cell culture). **(I)** Experimental groups used in J and K, analyzed at week 1 after starting DSS. **(J)** *Ccl2* expression by qPCR in $CD45^-CD90^+CD24^+$ colonic myenteric neurons FACS-purified from 1×DSS (2.5%)- or water-treated WT mice daily injected with PX-478 or vehicle, analyzed at week 1, and normalized to *Actb* (n = 6 per group). **(K)** Percentage of total viable cells (left) and absolute cell counts (right) of colonic Mo-MMs, quantified by FC (DSS vehicle and PX-478, n = 8 per group). Baseline shows the mean value for PX-478–injected water-treated mice (n = 1). **(L)** Experimental groups used in M–P, analyzed at weeks 1 and 11 after starting DSS. **(M)** Percentage of total viable cells (left) and absolute cell counts (right) of colonic Mo-MMs from tamoxifen- and 1× or 3×DSS-treated (2.5%) SLICK-$H^{ER\text{-}Cre}Vhl^{fl/fl}$ (Cre^+) and $Vhl^{fl/fl}$ littermates (Cre^-), quantified by FC (DSS Cre^- and Cre^+, n = 7–19 per group). Baseline shows the mean value for tamoxifen- and water-treated $Vhl^{fl/fl}$ littermates (Water Cre^-, n = 5–9). P values above each column indicate statistical differences against baseline. **(N)** Structural changes in colonic myenteric plexus of mice described in M, quantified by confocal microscopy, showing counts of neuron clusters, counts of Hu^+ neurons per cluster, and area and counts of IGFT regions. Data are shown as distributions of pooled values generated from analysis of 5–8 fields of view per mouse per group (DSS Cre^- and Cre^+, n = 4–7 per group; water Cre^-, n = 2–3). **(O)** Contacts between $MHCII^+$ MMs and Hu^+ myenteric neurons of mice described in M, analyzed at week 1 (DSS Cre^- and Cre^+, n = 4 per group). Baseline shows the mean value for tamoxifen- and water-treated $Vhl^{fl/fl}$ littermates (water Cre^-, n = 2). Data are shown as distributions of pooled values generated from analysis of 5 fields of view per mouse per group. **(P)** GI transit of mice described in M, analyzed at week 11 (DSS Cre^- and Cre^+, n = 7 per group). Baseline shows the mean value for tamoxifen- and water-treated $Vhl^{fl/fl}$ littermates (water Cre^-, n = 5). P values above each column indicate statistical differences against baseline. All graphs show the mean ± SEM, n—mouse, unless stated differently. Data are representative of at least two independent experiments with similar results. Data are pooled from two to four smaller experiments (D, E, K, and M). Statistical analyses: unpaired Student's t test (D–H, J, K, M, O, and P) and two-way ANOVA for multiple comparisons (N), *P ≤ 0.05, **P ≤ 0.01, ***P ≤ 0.001, and ****P ≤ 0.0001. # above pooled data in violin plots (N) indicates empirical P values calculated by the Nested Leave-One-Out Jackknife strategy, where #P < 0.05, ##P < 0.01, and ###P < 0.001.

Finally, we examined the effect of colitis-associated HIF signaling on ENS remodeling and postinflammatory GI dysmotility. Confocal microscopy revealed greater ganglion fragmentation, nerve fiber loss, and more MM–neuron contacts in $Hif1a^{\Delta Neu}$ mice with active colitis (Fig. S12, A–D). Conversely, $Vhl^{\Delta Neu}$ mice, with reduced monocyte recruitment, exhibited reduced ganglion fragmentation, nerve fiber loss, and fewer MM–neuron contacts (Fig. 6, N and O; and Fig. S12, E and F) during early colitis. In post-colitis mice, their ENS architecture was less remodeled, resembling that of water controls (Fig. 6 N; and Fig. S12, E and F) and $Ccl2^{\Delta Neu}$ mice (Fig. 5 G). In contrast to 3×DSS Cre^- mice, $Vhl^{\Delta Neu}$ mice with a history of colitis showed slower GI transit, similar to water control mice (Fig. 6 P). Thus, bolstering hypoxia-induced HIF signaling by VHL removal protects from pathological ENS remodeling and subsequent postinflammatory dysmotility.

Taken together, these results underscore the role of a hypoxia-induced stress response in enteric neurons that counterbalances their CCL2 expression and monocyte recruitment into the myenteric plexus, likely to prevent further escalation of tissue hypoxia, tissue damage, and excessive repair.

Hypoxia stress response and CCL2 associations are observed in IBD

Subsequently, we investigated whether the hypoxia stress response and CCL2 associations are observed in the intestinal tissue affected by IBD. We leveraged Bayesian networks (BNs) constructed from biopsies collected from the ileum and colon of 2,490 IBD patients, including inflamed and noninflamed tissue, and noninflamed samples from routine screening as controls. These probabilistic networks infer the causal regulatory hierarchy of co-expressed genes in five specific networks: control ileum, CD ileum, control colon, CD colon, and UC colon (Argmann et al., 2021; Suárez-Fariñas et al., 2021). We interrogated the networks for the presence of a hypoxia signal by searching for a homologous hypoxia subnetwork across all networks by curating a hypoxia gene signature comprised of genes downstream of HIF signaling (Watts and Walmsley, 2019) and CCL2/CCR2 (Serbina et al., 2008; Serbina et al., 2012) pathways from the literature. In projecting this hypoxia gene signature onto each network, we identified all gene network nodes overlapping between the signature genes and the network gene nodes (Fig. 7 A). We included all nodes extending out two path lengths from the shared signature and network nodes, to extract the largest connected subnetwork of each network, comprising the hypoxia subnetwork of each network. We generated the inflamed enteric neural signature based on scRNA-seq dataset from ileal IBD surgical resection specimen (Martin et al., 2019) (Table S7) and tested its fold enrichment in the hypoxia subnetwork relative to the full BNs for each of the five control and disease networks. In the control ileum, there was no significant overlap between the hypoxia and enteric neural subnetworks, and as expected, the enrichment between enteric neural and hypoxia response was greater in the normal colon than in the normal ileum, likely due to anaerobic lumen of control colon (Fisher's exact test [FET] 1.697, P value 0.0000002) (Colgan et al., 2016). In the IBD tissue, there was a significant overlap, in the CD ileum (FET 1.507, P value 0.0000008), CD colon (FET 1.507, P value 0.0000008), and UC colon (FET 1.5, P value 0.0027). *CCL2* was not present in the control ileum hypoxia subnetwork, where the overlap between the hypoxia and enteric neural subnetworks was not significant. However, *CCL2* was present within the hypoxia subnetworks of the other four networks, where the overlap with hypoxia and enteric neural networks was significant (Fig. 7 A). This analysis predicted the existence of a neuron-intrinsic hypoxia–CCL2 axis in the inflamed ileum, as well as in the normal and inflamed colon.

We then assessed the local network neighborhood structure of *CCL2*, which comprised all gene nodes directly connected

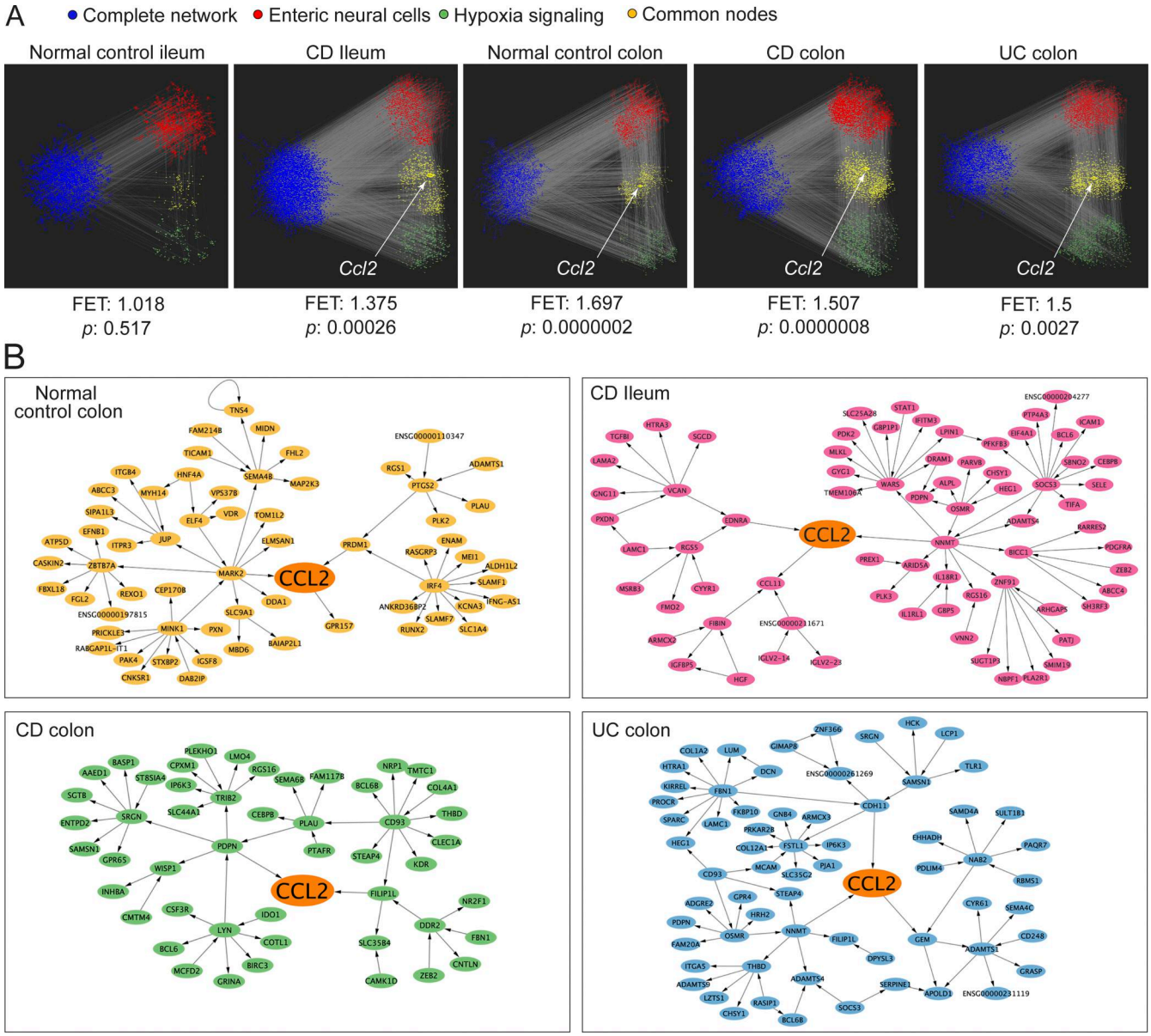

Figure 7. ***CCL2* subnetwork structure in IBD patients. (A)** Hypoxia and inflamed enteric neuron subnetworks from CD ileum constructed in the following BNs: control ileum, CD ileum, control colon, CD colon, and UC colon. FET was used to test enrichment with P < 0.05 as the cutoff. **(B)** *CCL2* subnetworks comprised of the *CCL2* node that is extended out to include all directly connected nodes within three path lengths in the IBD (CD Ileum, CD colon, and UC colon) and control (normal control colon) BNs. Present in normal control colon: *ELF4*, *IRF4*, *SLAMF1*, *SLAMF7*, and *IFNG-AS1* (genes involved in Th17 immune responses) (Cao et al., 2023); *DAB2IP*, *GPR15*, and *ELMSANI* (regulators of neuronal differentiation) (Chang et al., 2013; Takeo et al., 2016; Mondal et al., 2020); and *MARK2* and *TOMIL2* (involved in neurodegeneration) (Matenia and Mandelkow, 2009; Ou et al., 2021); or *SEMA4B* (axon guidance proteins) (Jian et al., 2014). Present in inflamed CD ileum: *IFGB5* (promotes neuronal apoptosis) (Guo et al., 2024), *ZEB2* (promotes proliferation and differentiation of enteric neural precursor cells) (Feng et al., 2024), *FIBIN* (a neurogrowth factor highly expressed in the brain) (Lakner et al., 2011), *PDK2* (a key component for inflammatory pain pathogenesis) (Jha et al., 2015), *MLKL* (involved in ischemia-induced neuronal necroptosis-driven microglia/macrophage polarization) (Yang et al., 2018), and *PDGFRA* (a marker for enteric neuron–associated fibroblast-like cells) (Kurahashi et al., 2011). Present in inflamed CD colon: *NRP1* (encodes neuropilin-1 and controls enteric neuron connectivity) (Gonzales et al., 2020), *NR2F1* (involved in neuronal differentiation and upregulated in aganglionic regions of Hirschsprung's disease) (Gomez Ramos et al., 2024; He et al., 2023), *SAMSN1* (regulates neural stem cell proliferation and promotes hypoxia-induced neuronal injury) (Wang et al., 2023), *ENTPD2* (expressed by enteric glia and regulates enteric neuron numbers and phenotype) (Grubišić et al., 2019), and *SGTB* (promotes neuronal differentiation and neurite outgrowth and is associated with neuronal apoptosis after neuroinflammation) (Vuong et al., 2019; Cao et al., 2013). Present in inflamed UC colon: *DCN* (extracellular matrix protein protecting from traumatic brain injury) (Oshima et al., 2024), *SRGN* (amplifies microglia-mediated neuroinflammation and exacerbates ischemic brain injury) (Qian et al., 2024), *HTRA1* (regulates neuronal differentiation, promotes HIF1α signaling, and is associated with Alzheimer's disease) (Qian et al., 2024), *KIRREL* (involved in synaptogenesis, axon branching, and angiogenesis) (Baltar et al., 2024; Wang et al., 2024), MCAM (involved in angiogenesis) (Jiang et al., 2012), and *PRKAR2B* (inhibits postsynaptic function of neurons) (Weise et al., 2019).

within three path lengths of *CCL2* (Fig. 7 B). No gene nodes were shared between colon control and IBD subnetworks, while some conserved network structure was shared among IBD subnetworks, possibly reflecting the differences between physiological and inflammatory hypoxia. The rest of the nodes were specific to each *CCL2* subnetwork's disease status and subset. Many genes in *CCL2* subnetworks of disease networks involve processes related to neurodegeneration, neural plasticity and neural differentiation programs, adaptation to tissue hypoxia, fibroblast/neuronal interaction, lympho- and angiogenesis, and extracellular matrix and smooth muscle remodeling (Fig. 7 B). Taken together, the identified gene nodes infer that human IBD is associated with remodeling processes of enteric neurons and related stromal cell types. They may predict novel biomarkers or disease targets for further evaluation and prospective validation in follow-up studies for disease types presenting with IBD in remission with motility disorders. In summary, the cellular and molecular pathways identified in our mouse studies are relevant to human IBD, warranting further investigation.

Discussion

Our study established the pathogenesis of colitis-associated postinflammatory GI dysmotility in a mouse model of transient colitis. We revealed that prolonged colitis results in substantial structural ENS remodeling that is pathological in the context of postinflammatory GI dysmotility. ENS remodeling is driven by a combination of partial neuronal loss caused by increased incidence of programmed cell death and subsequent gain of enteric neurons due to enhanced neurogenesis. Mucosal inflammation leads to the neurogenic CCL2-driven monocyte recruitment into the extra-mucosal myenteric plexus for the uptake and clearance of likely damaged neurons. However, newly formed Mo-MMs promote excessive neurodegeneration at the early inflammatory phase followed by excessive ENS remodeling, which we propose is a disproportionate ENS "repair" with dysmotility as its functional outcome. Finally, we identify the enteric neuron-intrinsic regulatory HIF–CCL2 axis that, when targeted, restricts monocyte recruitment into the myenteric plexus, reduces ENS remodeling, and prevents postinflammatory GI dysmotility.

Prior studies have viewed MMs as sessile microglia-like macrophages of mostly embryonic origin that switch their gene signature to a neuroprotective M2 phenotype in response to mucosal challenge (Gabanyi et al., 2016; Matheis et al., 2020; De Schepper et al., 2019). Our study reveals that the extra-mucosal myenteric plexus represents a dynamic cellular compartment along with the intestinal mucosa, and monocytes, known to infiltrate the inflamed mucosa early in the disease, are recruited in the myenteric plexus by activated enteric neurons. Once in the myenteric plexus, monocytes rapidly engage in functional interactions with enteric neurons and continue their differentiation trajectory into tissue MMs. The phenotype of newly recruited monocytes significantly differs from more differentiated Mo-MMs, but both express pro- and anti-inflammatory genes along with genes important for ENS homeostasis and function, suggesting different contributions to ENS remodeling. Future studies will investigate the role of Mo-MM–specific genes in ENS degeneration, regeneration, and subsequent remodeling upon colitis. However, developing an MM-specific Cre line will be necessary to avoid the impact on mucosal macrophages.

In the myenteric plexus, only enteric neurons can directly access the mucosa through their projected axons (Margolis et al., 2016; Melo et al., 2020; Fung et al., 2025), suggesting they directly sense mucosal inflammation. Our study demonstrates *in vivo* that in the context of inflammatory responses, the mucosal and myenteric plexus compartments are functionally interconnected despite their anatomical separation and highlight the unique role of enteric neurons in connecting these compartments through CCL2 chemokine production. However, the specific functional and neurochemical identity of myenteric neurons involved in sensing mucosal inflammation remains to be elucidated. Moreover, the neurochemical phenotype of newly generated neurons in colitis has yet to be characterized. Colitis has been shown to induce long-lasting changes in the intrinsic motor circuitry of the colon in response to inflammation (Mawe, 2015), but it needs to be determined whether newly derived neurons functionally integrate into the established motor circuits. The precise identity of the Nestin$^+$ progenitor responsible for generating enteric neurons also remains to be elucidated. However, a branching model proposed for ENS development (Laddach et al., 2023) suggests the possibility of a common lineage between adult enteric neurons and glia. Finally, the impact of mucosal inflammation on the submucosal plexus warrants further investigation.

Enteric glia are essential components of the ENS, interconnected with enteric neurons (Seguella and Gulbransen, 2021). Neuroglial bidirectional communication shapes enteric neurocircuit output, and hyperactive glia have been linked to postinflammatory dysmotility by driving aberrant neuronal excitation (Seguella et al., 2025). In our study, colitis induced an increase in Nestin$^+$ glia-like cells, suggesting reactive gliosis. However, enteric glia were not included in our analysis, highlighting a critical gap for future studies. Whether enteric glia contribute to plexitis in colitis remains untested. Interestingly, enteric neurons upregulate *Il1a* in response to LPS stimulation *in vitro* (Fig. S9 I), suggesting a potential local amplification loop that may involve glial cells.

The HIF pathway, a mechanism of cellular adaptation to hypoxic stress, has been shown to play a protective role in DSS colitis, with an intrinsic role in the intestinal epithelium (Karhausen et al., 2004; Robinson et al., 2008). Our study highlights the protective role of HIF signaling in pathological ENS remodeling, which is in line with genomic and transcriptomic data generated from the intestinal tissue of thousands of IBD patients. Based on these findings, pharmacologically enhancing the HIF pathway could be a therapeutic strategy in IBD to prevent postinflammatory GI dysmotility and improve gut health by limiting excessive ENS remodeling driven by inflammatory MMs, especially in early disease stages. The HIF pathway promotes glycolysis; in turn, its activity is tightly controlled by the metabolic state of the cell (Sharp and Bernaudin, 2004), with metabolites including lactic acid and

succinate that stabilize HIF1α (Tannahill et al., 2013; Sanmarco et al., 2023). This opens up new possibilities for metabolically regulating HIFs in gut inflammation, potentially through dietary supplementation or engineered probiotics (Sanmarco et al., 2023), to modulate the HIF pathway, control gut inflammation, including within the ENS, and ultimately reduce IBD-associated GI dysfunctions, thereby improving the quality of life of IBD patients.

Study limitations

For GI motility readouts, we focused on *in vivo* assays to directly link the functional changes with inflammatory readouts and biological tissue findings in the same animals. Although whole gut transit measurements in mice, like Carmine red leading-edge transit that we used, do not pinpoint the exact defect in intestinal motility, they "form the cornerstone of *in vivo* preclinical GI motility studies" (Kacmaz et al., 2021; Camilleri and Linden, 2016). Future studies should more precisely assess GI motility defects in our disease models.

Our mouse disease system modeled human relapsing–remitting colitis to study postinflammatory dysmotility. However, we were unable to validate our murine findings in IBD patients with quiescent disease and postinflammatory dysmotility because of the difficulty obtaining transmural biopsies from these patients. Instead, we showed that ENS remodeling is also relevant to refractory IBD. Interestingly, we found no impact of the neuron-to-macrophage CCL2 axis on mucosal inflammation, but *Ccl2*$^{\Delta Neu}$ mice regained their body weight after colitis faster than *Ccl2*-sufficient mice (Fig. S6 G), suggesting a possible link between ENS remodeling and other GI functions. Patients with dysmotility are more likely to have dysbiosis (Collins, 2014) and indigestion-related issues (Rasmussen et al., 2015), both with the potential to destabilize intestinal homeostasis and, hypothetically, predispose to disease flares, which may explain why IBS is a risk factor for IBD (Olbe, 2008). Future studies should investigate the link between ENS remodeling and IBD progression. Further investigation into the mechanisms driving disease-induced ENS remodeling may offer broader insights into inflammation-driven tissue remodeling processes, including fibrosis, stenosis, and vascular changes characteristic of refractory IBD.

Materials and methods

Experimental animals

WT B6 mice were obtained from Charles River Laboratories. *Il10*$^{-/-}$ (B6.129P2-*Il10*^{tm1Cgn}/J; #002251; Jackson Laboratory [JAX]) (Kühn et al., 1993), *Nestin*$^{ER\text{-}Cre}$ (B6-Tg(Nes-cre/ERT2)KEisc/J; #016261; JAX) (Lagace et al., 2007), *Actl6b*^{Cre} (Tg(Actl6b-Cre)4092Jiwu/J; #027826; JAX) (Zhan et al., 2015), *Rosa26*-STOP$^{fl/fl}$tdTomato (B6.*Cg-Gt(ROSA)26Sor*$^{tm14(CAG\text{-}tdTomato)Hze}$/J; #007914; JAX) (Madisen et al., 2010), *Ccr2*$^{RFP/RFP}$*Cx3cr1*$^{GFP/GFP}$ (B6.129(Cg)-*Cx3cr1*^{tm1Litt} *Ccr2*$^{tm2.1Ifc}$/JernJ; #032127; JAX) (Jung et al., 2000; Saederup et al., 2010), *Ccr2*$^{ER\text{-}Cre/ER\text{-}Cre}$ (B6-*Ccr2*$^{em1(icre/ERT2)Peng}$/J; #035229; JAX) (Xu et al., 2020), SLICK-H$^{ER\text{-}Cre}$ (Tg(Thy1-cre/ERT2,-EYFP)HGfng/PyngJ; #012708; JAX) (Young et al., 2008), *Ccl2*-RFP$^{fl/fl}$ (B6.Cg-*Ccl2*$^{tm1.1Pame}$/J; #016849; JAX) (Shi et al., 2011), *Myd88*$^{fl/fl}$ (B6.129P2(SJL)-*Myd88*^{tm1Defr}/J; #008888; JAX) (Hou et al., 2008), *Hif1a*$^{fl/fl}$ (B6.129-*Hif1a*^{tm3Rsjo}/J; #00756; JAX) (Ryan et al., 2000), and *Vhl*$^{fl/fl}$ (C;129S-*Vhl*^{tm1Jae}/J; #004081; JAX) (Karhausen et al., 2004) mice were purchased from the Jackson Laboratory. Since male mice were shown to be more susceptible to DSS-induced colitis (Babickova et al., 2015), only adult females between 5 and 8 wk of age were used. To minimize the role of genetic background, and reduce cage effects and differences in microbiota, cohoused littermates were used. Mice were maintained in specific pathogen-free conditions with food and water provided ad libitum. All animal experiments were performed in accordance with and approved by the Institutional Animal Care and Use Committees at Penn State University College of Medicine, Hershey, PA, USA, the University of Massachusetts Chan Medical School, Worcester, MA, USA, and Johns Hopkins University School of Medicine, Baltimore, MD, USA.

Colitis induction

To induce colitis, mice received 2–4% DSS in sterile drinking water for 5 days and then switched to sterile drinking water for 5 days. This constituted 1 cycle of DSS treatment (1×DSS). For most experiments, mice were given 3 cycles of DSS (3×DSS) followed for up to 60–80 days of post-colitis recovery period. Control mice received sterile drinking water throughout the experiment. For analysis, mice were euthanized on days 5–8 for an early acute colitis phase and days 60–80 for the recovery phase after starting the DSS treatment regimen. For spontaneous colitis, mice received sterile drinking water from the weaning stage and were monitored weekly for body weight and clinical symptoms until they presented with rectal prolapse indicating progressive colitis. To mitigate microbiota-related variability, Cre^{+} and Cre^{-} littermates on DSS were housed together in the same cages.

Inducible gene depletion and cell-fate mapping *in vivo*

Inducible Cre mice and corresponding controls were orally gavaged with 20 mg/ml of tamoxifen (T5648-5G; Sigma-Aldrich) dissolved in corn oil to induce Cre recombinase expression. Before starting the 1×DSS or 3×DSS treatment regimens, mice received two 5-day cycles of tamoxifen with a 5-day break between each cycle. After starting the DSS treatment, mice were given two consecutive gavages every 10 days until the end of the experiment. To trace Mo-MMs, tamoxifen was given for 4 days before the start of the DSS treatment and then given on alternate days until analysis.

LPS treatment *in vivo*

To induce a systemic inflammatory response *in vivo*, mice were injected with sterile 1×PBS containing LPS (10 mg/kg, #L2630; Sigma-Aldrich) or 1×PBS alone intraperitoneally (i.p.) 6 h before the analysis.

HIF1α inhibition *in vivo*

To inhibit HIF1α *in vivo*, B6 mice were injected with PX-478 (#202350; MedKoo Biosciences) in sterile 1×PBS i.p. daily for 3 days before the start of DSS treatment at a dosage of 25 mg/kg, which was then continued daily throughout the DSS cycle until

analysis at week 1 (Schwartz et al., 2009; Li et al., 2021). Control mice were given i.p. injections of sterile 1×PBS daily until analysis.

Detection of tissue hypoxia

To detect hypoxic cells *in vivo* during colitis, the EF5 Hypoxia Detection Kit that included EF5 reagent and EF5-specific antibody (EF5-30A4; EMD Millipore) was used (Koch, 2002). Briefly, at week 1, 3 h before euthanasia, control and DSS-treated mice were retro-orbitally injected with 10 nM of EF5 compound. Harvested colons were washed with complete HBSS (HBSS with 2% FBS) containing dithiothreitol (DTT), rolled into "Swiss rolls," embedded into optimal cutting temperature (OCT) compound, and snap-frozen at −80°C. Eight-µm tissue cross-sections of the frozen Swiss roll tissue were fixed in 4% paraformaldehyde (PFA), blocked, and stained with the antibody specific to Hu (1:500, clone EPR19098; Abcam, stains neuronal somas) followed by donkey anti-rabbit Cy3 secondary antibody (1:800, Jackson ImmunoResearch) and DAPI. Tissue sections were re-fixed with 4% PFA, blocked, stained with Alexa Fluor 488–conjugated EF5 antibody (clone ELK3-51, 150 µg/ml), and mounted onto histological slides with Prolong Diamond Antifade mounting medium (#P36965; Thermo Fisher Scientific). To detect HIF1α-expressing neurons, 8-µm tissue cross-sections of the colon Swiss rolls frozen in OCT were fixed in 4% PFA, blocked, and stained with HIF1α antibody (1:100 dilution, rabbit clone D1S7W, Cell Signaling), and serum was collected from a seropositive patient with a confirmed high titer of type 1 antineuronal nuclear antibody (ANNA-1) specific to Hu (stains neuronal somas, reactive to mouse and human, 1:1,000 dilution; ANNA-1–containing serum was provided by Dr. Sean J. Pittock, Mayo Clinic, Rochester, MN, USA). This was followed by staining with a mixture of fluorochrome-conjugated secondary antibodies raised in donkey against rabbit and human immunoglobulin, and DAPI. Tissue mounting was done as described earlier.

Total GI transit time assay

Total GI transit time assay was performed as we described previously (Muller et al., 2014). Briefly, 3 days prior to the assay, mice were acclimated by being individually housed with hydrogel and no bedding, and fasted for the duration of the assay. On the assay day, mice were given 300 µl of sterile water containing 6% carmine red (Sigma-Aldrich), 0.5% methylcellulose (Sigma-Aldrich), and 0.9% NaCl by intragastric gavage, and fecal pellets were examined for the first appearance of the red dye. Total GI transit time was calculated as the time between gavage and the appearance of the first red fecal pellet.

Sample and tissue collection

To monitor luminal lipocalin-2 levels, fecal pellets were collected weekly and at the end of the experiment, resuspended in 1×PBS, and stored at −80°C for later analysis. Blood was drawn by cardiac puncture to analyze blood monocyte populations by flow cytometry. Colons were processed as we described previously (Koscso and Bogunovic, 2016; Koscso et al., 2015). Briefly, harvested colons were cleaned and washed using complete HBSS containing DTT and EDTA to remove mucus and epithelial cells. Colonic muscularis externa was mechanically separated from the mucosa and submucosa as described previously (Koscso and Bogunovic, 2016; Koscso et al., 2015).

Tissue processing for immunofluorescence

A 5-mm-long piece of the muscularis externa from the mid-colon was excised and fixed with 4% PFA. For experiments comparing neurogenesis in different colon regions, 5-mm-long pieces of the muscularis externa were also excised from the proximal colon. Tissues expressing fluorescent proteins from various reporter mice (*Ccl2*-RFP$^{fl/fl}$ mice containing mCherry, *Actl6b*$^{Cre/+}$*Rosa26*-STOP$^{fl/fl}$tdTomato mice, *Nestin*$^{ER\text{-}Cre}$*Rosa26*-STOP$^{fl/fl}$tdTomato mice, SLICK-H$^{ER\text{-}Cre}$*Rosa26*-STOP$^{fl/fl}$tdTomato mice and *Ccr2*$^{ER\text{-}Cre/ER\text{-}Cre}$*Rosa26*-STOP$^{fl/fl}$tdTomato mice containing tdTomato, and *Ccr2*$^{RFP/+}$*Cx3cr1*$^{GFP/+}$ mice containing RFP and GFP) were fixed with 4% PFA containing 20% sucrose to preserve the fluorescent proteins. After fixation, tissue was stored in 1×PBS containing 30% sucrose at 4°C until immunofluorescence staining.

Human intestinal tissue

Deidentified full-thickness intestinal specimens surgically removed from 4 patients with CD and 2 non-IBD control patients with CRC undergoing colectomy were provided by the UMass Center for Clinical and Translational Science Biorepository under an approved IRB protocol and after informed consent. For CD, noninflamed and inflamed regions were provided for each patient. For two CD patients, large bowel tissue from noninflamed and inflamed regions defined macroscopically by a Board-certified pathologist was provided. For one CD patient, the noninflamed sample was from colon, while the inflamed sample was from the terminal ileum (the terminal ileum sample was excluded from further analysis). For CRC patients, normal large bowel regions adjacent to tumors were used as a control.

Received tissue samples were rinsed with 1×PBS, fixed with 4% PFA, and incubated in 1% PFA with increasing concentrations (10, 20, and 30%) of sucrose. Next, tissues were incubated in a 1:1 mixture of OCT and 1% PFA containing 30% sucrose and embedded in OCT compound before freezing at −80°C.

Immunofluorescence

Mouse whole tissue

Fixed 5-mm piece of intact muscularis externa was washed with 1×PBS, blocked in 1×PBS containing 2% BSA and 1% Triton X, stained with a specific primary antibody cocktail, washed again, and stained with a mixture containing DAPI and a combination of fluorochrome-conjugated antibodies raised in donkey against rat, goat, rabbit, chicken, human, or Armenian hamster. Stained tissues were mounted on histological slides with Prolong Diamond Antifade mounting medium. To stain cells of the myenteric plexus, antibodies specific to mouse Hu (stains neuronal somas, 1:500, clone EPR19098; Abcam), βIII-tubulin (stains nerve fibers, 1:250, rabbit or chicken polyclonal, Abcam), PGP9.5 (stains entire neurons, 1:500, clone EPR4118; Abcam), S100β (stains glial cells, 1:250, rabbit polyclonal, Proteintech), CD31 (stains endothelial cells, 1:200, clone MEC7.46; Novus Biologicals), and

MHCII I-A/I-E (stains MMs, 1:100, clone MS/114.15.2; BioLegend) were used. Serum containing ANNA-1 (specific to Hu, 1:1,000) was also used when indicated. Antibodies specific to tdTomato, RFP, or mCherry (1:250, goat polyclonal, OriGene) and for GFP (1:100, clone FM264G; BioLegend) were used to amplify the signal of endogenously expressed fluorescent reporter proteins. To stain apoptotic neurons, fixed colonic muscularis externa was blocked in 1×PBS containing 5% donkey serum, 0.3% Triton X, and 1% penicillin–streptomycin, then stained with primary antibodies specific to CC7 (Nozaki et al., 2022) (1:250, clone Asp 198; Cell Signaling), βIII-tubulin, and ANNA-1 followed by staining with fluorochrome-conjugated secondary antibodies and mounting as previously described. To stain CCL2-expressing cells, 0.25 mg of brefeldin A (Enzo Life Sciences) was i.p. injected into DSS-treated mice 6 h before euthanasia. Colons were harvested, processed, and fixed as described above. 10 µg/ml of brefeldin A was maintained in all buffers until the blocking step (Koscso et al., 2020). Fixed tissues were blocked, and stained with a primary antibody cocktail containing antibodies specific to RFP, Hu, and MHCII followed by washing, staining with fluorochrome-conjugated secondary antibodies, and mounting on histological slides.

Mouse tissue sections

To detect newly generated neurons along the entire length of the colon, 8-µm tissue cross-sections of colonic Swiss rolls from tamoxifen-treated *Nestin*$^{ER\text{-}Cre}$*Rosa26*-STOP$^{fl/fl}$tdTomato mice and control mice were fixed as mentioned previously. Sections were blocked and stained with a primary antibody cocktail containing antibodies specific to mouse Hu and RFP. Sections were then stained with secondary antibody cocktail containing fluorochrome-conjugated antibodies raised in donkey against rabbit and goat, and DAPI, and then mounted on histological slides.

Human tissue sections

10-µm-thick intestinal tissue cross-sections were blocked with 5% normal donkey serum in 1×PBS containing 0.05% Triton X. Sections were stained with primary antibodies specific to mouse Hu (1:250), βIII-tubulin (1:250), and human HLA-DR (1:250, LN-3; Leica/Novocastra) followed by staining with a cocktail of DAPI and fluorochrome-conjugated secondary antibodies and mounting on histological slides. To detect CCL2 expression in neurons, 10-µm-thick intestinal tissue cross-sections were blocked with 5% normal goat serum in 1×PBS containing 0.01% Triton X, stained with primary antibody specific to mouse CCL2 (1:100, mouse monoclonal, 2D8; Sigma-Aldrich) and Hu (1:250), or mouse IgG1$_\lambda$ isotype control (BD Biosciences) followed by staining with secondary antibodies and mounting on histological slides as previously described.

Microscopy

Whole muscularis externa or cross-sections of mouse colons were imaged using the Leica HC PL APO CS2 10×/0.4 NA objective at 1.136 × 1.136 µm pixel size or 0.568 × 0.568 µm pixel size on the Leica SP8 confocal microscope. The Leica HC PL APO CS2 20×/0.75 NA objective was used at 0.284 × 0.284 µm pixel size on the Leica SP8 confocal microscope for primary adult mouse neuronal cultures. For 3D imaging of neuron–macrophage interactions, the Nikon CFI75 Apo LWD 25× W 1.1 NA objective on the Nikon A1R multiphoton was used. The 10× and 20× water immersion and 63× oil immersion objectives on the Nikon A1R multiphoton microscope were used. All images were processed using Volocity 7 and 6.3.1, Quorum Technologies Inc, and Imaris Viewer, Oxford Instruments. Human tissue sections, mouse tissue sections, and primary adult mouse neuronal cultures were imaged using a 20× 0.75 NA Zeiss Plan Apo objective on the TissueGnostics TissueFAXS SL Q slide scanning microscope. Images were acquired in fluorescence mode, and focus points across the selected region were determined using the DAPI channel. Acquired images were processed using StrataQuest, TissueGnostics, Inc.

Image analysis to quantify ENS remodeling

Confocal microscopy of mouse myenteric plexus

ENS remodeling was assessed by automated analysis of XY images of intact myenteric plexus from mouse colons generated by confocal microscopy to quantify the (1) total number of Hu$^+$ neurons, (2) number of Hu$^+$ neuron clusters, (3) number of Hu$^+$ neurons per cluster, (4) number of IGFT regions, (5) IGFT region size, (6) number of contacts between MMs and neurons, and (7) total MHCII$^+$ MM area per field of view (FOV) using Volocity. Volocity quantitation package was used to create specific measurement protocols based on parameters like standard deviation intensity, size, channel, and region of interest (ROI). All data were normalized to mm^2. For all experiments, 5–8 FOVs were analyzed per mouse and each experiment had $n \geq 3$ mice per group.

Neuron and ganglion identification criteria were adapted from the methodology previously described (Kulkarni et al., 2017; Kulkarni et al., 2023; Young et al., 1993; Zhou et al., 2013). Briefly, an intact *ganglion* or a smaller *cluster of neurons* was defined as a contiguous group of 2 or more Hu $^+$ neurons separated from other Hu$^+$ neurons by a distance ≥ the diameter of at least 2 neurons. The neuronal ganglion or cluster must also be surrounded by βIII-tubulin$^+$ nerve fibers. *Neuron counts per cluster* were defined as the number of Hu$^+$ neurons in a ganglion or cluster. Changes to the organization of nerve fiber architecture of the myenteric plexus were assessed by counting the number and measuring the area of the rounded spaces between Hu$^+$ myenteric ganglia and βIII-tubulin$^+$ intraganglionic fiber tracts that we referred to as *IGFT* regions. Reduction of total Hu$^+$ neuron counts correlated with the increase in neuronal cluster counts and reduced number of neurons per cluster indicative of neuronal loss and fragmentation of the ganglia. Changes in IGFT region counts and IGFT areas reflected loss or gain of IGFTs. In active colitis, we observed a decrease in IGFT region counts and an increase in their area along with reduced Hu$^+$ neuron counts, increased neuronal cluster counts, and fewer neurons per cluster and interpreted it as neuronal loss and neurodegeneration. In late post-colitis phase, an increase in IGFT counts and a decrease in their area correlated with partial

recovery of Hu$^+$ neuronal counts, decreased neuronal cluster counts, and more neurons per cluster that was interpreted as neural regeneration and neurogenesis. A combination of all readouts was the most informative, with the total number of neurons being more variable across the fields and requiring a higher sample size.

MMs were identified as MHCII$^+$ cells and were quantified by measuring the total signal intensity area (i.e., *total MHCII$^+$ area*). Colocalization of MHCII$^+$ signal with Hu$^+$ signal was defined as *contacts* and was measured by identifying the MHCII signal and colocalization of it with the Hu$^+$ signal and conversely. Both ways of quantification were found to be similar and comparable.

Multiphoton microscopy of mouse myenteric plexus

Automated analysis of z-stack multiphoton images was done to quantify the (1) number of Hu$^+$ neurons, (2) number of MHCII$^+$ MMs, (3) number of contacts between MHCII$^+$ MMs and Hu$^+$ neurons, and (4) Hu$^+$ neuronal signal inside MHCII$^+$ MMs that measured uptake of neuronal cellular components by MMs, per FOV using Volocity. All data were normalized to mm^2. For all experiments, 5–8 FOVs were analyzed per mouse and each experiment had $n \geq 3$ mice per group.

Confocal microscopy of tissue sections

To quantify hypoxic neurons in mouse intestinal tissue sections, immunofluorescence images were used to determine the percentage of EF5$^+$ Hu$^+$ neurons per ganglion manually. Automated measurement of Hu$^+$ ganglion counts and size was performed using StrataQuest v7.1.1.143. Data were normalized to mm^2.

ENS remodeling in human large bowel cross-sections

Analysis of immunofluorescence images was performed using a StrataQuest v7.1.1.143 analysis pipeline that was developed to quantify the (1) total area of HLA-DR$^+$ signal per ROI indicating inflammation, (2) total area of βIII-tubulin$^+$ signal per ROI indicating innervation, and (3) area of Hu$^+$ neuronal ganglia. To avoid quantitation errors due to folds in tissue sections, a machine-learning algorithm was used. Briefly, areas with folds and areas without folds were identified by hand in multiple images from the dataset. Manually identified regions were then used to train the classifier to identify areas with folds. Any region identified as a fold was masked out of the image before analysis was conducted. DAPI channel was used to identify nuclei. Hu$^+$ neurons were manually counted within each ganglion to calculate the density of Hu$^+$ neurons per ganglion area (*neuron density*). All data were normalized to mm^2.

Flow cytometry and cell sorting

Freshly isolated colonic muscularis externa or mucosa with submucosa was subjected to enzymatic digestion to obtain single-cell suspensions as we described previously (Koscso and Bogunovic, 2016; Koscso et al., 2015). The number of total live cells in suspension was calculated using a hemocytometer. These total cell counts were used to calculate absolute counts of different subsets. Blood samples were subjected to red blood cell lysis. Obtained single-cell suspensions were stained with antibodies for cell-specific markers.

Antibodies

All antibodies were purchased from BioLegend unless indicated. To stain neurons, antibodies specific to mouse CD24 (clone M1/69; BD Biosciences) and CD90.2 (clone 53-2.1; BD Biosciences) were used. To stain monocytes and macrophages, antibodies specific to mouse CD45 (clone 30-F11), CD11b (clone M1/70), CD11c (clone N418), CD16/32 (clone 93), Ly6c (clone HK1.4), and MHCII I-A/I-E (clone MS/114.15.2) were used. To stain neutrophils, an antibody specific to mouse Ly6g (clone 1A8) was used. To stain B cells and T cells, antibodies specific to mouse B220 (clone RA3-6B2) and CD3 (clone 145-2C11; Thermo Fisher Scientific) were used. For live-cell staining, either DAPI (BioLegend) or Aqua fluorescent reactive dye (Invitrogen) was used. For intracellular staining of PGP9.5 expressed by enteric neurons, fresh cells were first stained for cell surface markers, fixed using the BD Cytofix/Cytoperm Fixation/Permeabilization Solution Kit, and then stained with antibody specific to mouse PGP9.5. All stained samples were acquired on BD LSRII flow cytometers.

Gating strategy

In the mucosa with submucosa, immune cell subsets were analyzed using a published gating strategy (Koscso et al., 2015; Koscso et al., 2020; Koscso and Bogunovic, 2016). In the muscularis, CD90$^+$CD24$^+$ neurons and all other nonneuronal, nonimmune cells (CD90$^+$, CD24$^+$, CD90$^-$CD24$^-$subsets) were defined by gating on CD45$^-$ live cells. In line with a prior report (Windster et al., 2023) on human neurons, SSC/FSC^{lo} nonnucleated cell debris was excluded. To minimize neuronal contamination with other cell types, particularly glia, a strict singlet gate was applied. Immune cell subsets were defined by gating on CD45$^+$ live singlets. Total CD45$^+$ lymphocytes were defined as CD45$^+$CD11b$^-$ cells. M-T cells were defined as CD45$^+$CD11b$^-$CD3$^+$ cells. CD45$^+$CD11b$^+$ myeloid cells were divided into M-PMNs defined as SSC-A^{hi}CD16/32$^-$ (Ly6g$^-$ and Ly6g$^+$) cells and MMs defined as SSC-A$^{lo\text{-}int}$Ly6g$^-$CD16/32$^+$ cells. MMs were further divided into additional subsets based on the combination of *Ccr2*-RFP, *Cx3cr1*-GFP, and cell surface binding of Ly6c and MHCII antibodies as shown in the Results.

Flow cytometry analysis

Data analysis was performed using FlowJo software (FlowJo LLC). *Ccr2*$^{RFP/+}$*Cx3cr1*$^{GFP/+}$ reporter mice were used to perform an unbiased comparative analysis of immune cell subsets of the muscularis externa. All CD45$^+$ events were concatenated groupwise. Unsupervised t-distributed stochastic neighbor embedding (t-SNE) analysis was performed with FlowJo t-SNE plugin set to 6 phenotypic markers (CD11b, CD16/32, *Cx3cr1*-GFP, *Ccr2*-RFP, Ly6c, and MHCII) and used the following settings: auto (opt-SNE)-learning algorithm with approximate (random projection forest-ANNOY) K-Nearest Neighbors (KNN) algorithm (Belkina et al., 2019) and Fast Fourier Transform (FFT) Interpolation (flt-SNE) gradient algorithm.

Sorting of MMs

Ccr2$^{RFP/+}$*Cx3cr1*$^{GFP/+}$ reporter mice were used to sort MM subsets for bulk RNA-seq. Colonic muscularis externa was isolated from cohorts of 3–5 DSS-treated and 3–5 water-treated mice at week 1 time point. Muscularis single-cell suspensions from 5 mice were pooled per condition and represented one replicate. Specific MM subsets were isolated by FACS. In total, 5 such replicates were prepared representing 5 independent cell sorting experiments. Cell sorting was done as we described previously (Koscso and Bogunovic, 2016; Koscso et al., 2015). Cells were stained with a combination of CD45, CD11b, CD16/32, Ly6c, and MHCII antibodies. MMs were defined as CD45$^+$CD11b$^+$CD16/32$^+$ viable singlets, and MM subsets were sorted by a four-way sort using the BD FACSAria Fusion flow cytometer. Based on *Ccr2*-RFP expression, MM subsets were broken down into CCR2$^+$MHCII$^-$ (subset 1), CCR2$^+$Ly6c$^+$MHCII$^+$ (subset 2), CCR2$^+$Ly6c$^-$MHCII$^+$ (subset 3), CCR2$^-$Ly6c$^-$MHCII+ (subset 4), and CCR2$^-$MHCII$^-$ (subset 5) subsets. Between 5,000 and 10,000 cells of subsets 2, 3, 4, and 5 were sorted from control mice, and subsets 1, 2, 3, and 4 were sorted from DSS mice, based on cell frequency.

Sorting of neurons

Single-cell suspensions were prepared from the muscularis of WT B6 mice with or without colitis. Nonimmune cells were defined as CD45$^-$ viable singlets. CD90$^+$CD24$^+$ neurons and other CD45$^-$ cells (pooled CD24$^-$CD90$^+$, CD90$^-$CD24$^+$, CD90$^-$CD24$^-$ stromal cell subsets) were subjected to a 4-way sort using the BD FACSAria Fusion flow cytometer. Sorted cells were collected in RPMI with 10% FBS and stored in TRIzol at −80°C for further processing and analysis.

RNA isolation and gene expression analysis

Total RNA was extracted from sorted cells, 3-mm^2 piece of muscularis externa tissue, and primary adult enteric neuron cultures using TRIzol extraction protocol as described previously (Koscso et al., 2020). RNA was reverse-transcribed using RNA-to-cDNA EcoDry premix (Takara Bio). Gene expression was measured using Power SYBR Green PCR Master Mix (Life Technologies) on a Bio-Rad qPCR instrument. *Ccl2* (Mm.PT.58.42151692), *Vegfa* (Mm.PT.58.13368357), *Csf1* (Mm.PT.58.11661276), *Il1a* (Mm.PT.58.32778767), *Hif1a* (Mm.PT.58.12608714), *Elavl3* (Mm.PT.58.30335452), *Elavl4* (Mm.T.58.33020194), *Uchl1* (Mm.PT.58.32038186), *s100b* (Mm.PT.58.30112765), and *Actb* (IDT 419680055, 419680054) PrimeTime qPCR primers were purchased from Integrated DNA Technologies. Gene expression levels were calculated by normalization to *Actb* and shown as fold change over the control group or population described in the figure legends. Cq (Quantification cycle) values for *Actb* for each cell culture condition were used as an indirect measurement of cell viability in culture.

mRNA-seq

Total RNA was isolated from sorted cell populations as described previously. cDNA libraries were prepared using the QuantSeq 3′ mRNA-seq Library Prep Kit FWD for Illumina (Lexogen) following the manufacturer's instructions. Briefly, RNA-seq libraries were prepared using Lexogen's QuantSeq 3′ mRNA-seq V2 Library Prep Kit Forward (FWD) with 12-nucleotide Unique Dual Indices following the manufacturer's instructions for low-input RNA library prep. One nanogram of total RNA was reverse-transcribed using oligo (dT) primers. The second cDNA strand was synthesized by random priming followed by cDNA purification and library amplification using Lexogen's 12-nt Unique Dual Indices and 24 cycles. The libraries were analyzed for size distribution and concentration using the Bioanalyzer High-Sensitivity DNA kit (Agilent Technologies). Libraries were pooled at equimolar concentrations and sequenced on NovaSeq 6000 (Illumina) to get ∼5 million paired-end 50-bp reads.

RNA-seq analysis of sorted MM subsets

To analyze data generated from mRNA-seq of sorted MM subsets, FastQC (v0.11.9) was used to compute basic statistics and check quality control (QC) of paired reads from RNA-seq (Germain et al., 2021). The results showed that R2 of the paired reads has overall low quality, and considerable number of overrepresented repetitive sequences; thus, only R1 reads were used for further analysis. Trimmomatic (v0.36) was used to trim low-quality parts of reads (Bolger et al., 2014). STAR (v2.7.5b) was used to align reads to GRCm39 (Dobin et al., 2013). Reads counts for each gene were summarized using RNA-SeQC (v2.1.0) (Graubert et al., 2021). Contribution of covariates to the variance was investigated using variancePartition (v1.32.2) (Hoffman and Schadt, 2016). The DEGs were identified by limma-voom model implemented in edgeR package (v4.0.14) (Robinson and Smyth, 2007). The signature for each macrophage subset was generated by taking the union of all differential expression signatures (including up- and downregulated) from pairwise comparison of each subset to all other subsets. Additional DEG signatures include DSS versus water control for each subset and comparisons of specific pairwise DSS subgroups. The cutoff for significance was less than the adjusted P value 0.05 and greater than log fold change 1.5 or less than −1.5. The heatmap was generated using heatmaply (v1.5.0) (Galili et al., 2018). Pathway analyses were conducted using Enrichr (v3.2) (Kuleshov et al., 2016) and David (Huang et al., 2009; Kuleshov et al., 2016; Sherman et al., 2022).

scRNA-seq of muscularis externa

Single-cell suspensions were made from the muscularis externa of the colonic muscularis externa isolated from 11-wk-old adult WT B6 mice as described previously (Kulkarni et al., 2017; Kulkarni et al., 2023). The separated muscularis externa was digested, filtered, and resuspended into maintenance solution containing Opti-MEM with GlutaMAX, B27 supplement, actinomycin D, and RNase inhibitor. Filtered single-cell suspensions were assessed for viability and cell counts using Trypan Blue and Cell Countess (Invitrogen). The library was prepared using Chromium Next GEM Single Cell 3′ kit v3.1 (10× Genomics) at a read depth of 20,000/cell and was sequenced using the NovaSeq 6000 (Illumina) by the Johns Hopkins Single Cell Sequencing Core.

Transcriptome analysis of muscularis externa by scRNA-seq

To analyze data generated from the scRNA-seq of muscularis externa, raw 10× read processing and QC raw sequence reads were quality-checked using FastQC (v0.11.9) software (Andrews, S. [2010]. FastQC: A Quality Control Tool for High Throughput Sequence Data [Online]. Available online at: https://www.bioinformatics.babraham.ac.uk/projects/fastqc/). The Cell Ranger version 7.0 software suite from 10× Genomics was used to process, align, and summarize unique molecular identifier (UMI) counts against the mouse GRCm38 assembly reference genome analysis set, obtained from https://www.10xgenomics.com. Filtered count matrices from Cell Ranger were imported into R (version 4.3.2) for further processing. Low-quality cells were filtered, such as cells for which a high percentage of UMIs originated from mitochondrial features (>20%) and cells with <200 expressed genes. Three methods, Doubletfinder (v2.0.4) (McGinnis et al., 2019), Scds (v1.18.0) (Bais and Kostka, 2020), and scDblFinder(v1.16.0) (Germain et al., 2021), were applied to detect doublets, and doublet cells identified by at least two methods were filtered. Median absolute deviation method was used to derive a cutoff for the maximum number of genes in the cell. After filtering, 34,417 cells were left, and used for further analysis. The Seurat R package (version 5.0) was used for normalization. Harmony (v1.2) was used for integration and plotting (Butler et al., 2018; Hao et al., 2024). Slingshot (v2.10) was used for trajectory and pseudotime analysis (Street et al., 2018). CellChat (v2.1.2) was used to predict cell-to-cell communications between macrophage clusters and neurons (Jin et al., 2021).

To assess the relevance of the MM–neuron crosstalk from the intestine of normal WT mice in the DSS setting, the single-cell MM–neuron interaction gene list determined by CellChat and DSS variance signature enrichment in mouse co-expression network was performed using FET.

IBD patient cohort gene expression analysis

BNs

BNs can capture fundamental properties of complex systems in states that give rise to complex (diseased) phenotypes. We and others have successfully identified and validated a large number of novel targets using these derived network models in various complex diseases, such as diabetes, Alzheimer's disease, and IBD. Individual BNs were constructed from RNA sequence data generated on intestinal biopsy specimens and DNA SNP panels from the Mount Sinai Crohn's and Colitis Registry (MSCCR) UC, CD, and control cohorts (Argmann et al., 2021; Suárez-Fariñas et al., 2021) using their intestinal expression quantitative trait locus information as previously described (Peters et al., 2017). The BNs are region- (ileum/colon) and disease-specific and include both inflamed and noninflamed biopsies. The MSCCR BN was reconstructed using RIMBANet software as previously described and visualized using Cytoscape 3.7. RIMBANet software is available with step-by-step instructions. Final networks were decided with Markov chain Monte Carlo simulation that creates thousands of possible different networks, which were then combined to form a consensus network (RIMBANET: Reconstructing Integrative Molecular Bayesian Network, Integrative Network Biology Group [Zhu Lab], GitHub) (Zhu et al., 2008).

Hypoxia gene list

We curated a hypoxia gene list to represent a signature of genes involved in hypoxia signaling combined from (Mojsilovic-Petrovic et al., 2007) and Enrichr (Chen et al., 2013; Kuleshov et al., 2016; Xie et al., 2021). To identify genes expressed in inflamed enteric neurons, we developed a method to generate cell type–specific signatures using scRNA-seq from the previously published dataset (Martin et al., 2019). We generated hypoxia subnetworks in the following BNs: control ileum BN, CD ileum BN, control colon BN, CD colon BN, and UC colon BN; and by projecting each signature onto the BN, identifying all overlapping nodes between the signature and the BN, then extending out two path lengths, and extracting the largest connected subnetwork using Cytoscape 3.10.2. To test for enrichment of the signature in the subnetwork relative to the full BN, we performed FET, using P value of <0.05 as a cutoff.

Enteric neural signature

The scRNA-seq raw data were published in a prior publication (Martin et al., 2019). We devised an analysis to generate a cell type–specific identity signature for the inflamed enteric neuron by using an unsupervised computational clustering approach employing the Seurat package. Briefly, we generated a gene expression profile for each cell type and/or subset after clustering cells according to each cell type expression profile. Next, we identified genes differentially expressed between inflamed enteric neural cells and the other intestinal cell types in the inflamed IBD ileal tissue, as well as genes expressed above the threshold for expression in the majority proportion of the inflamed enteric neural cells (Table S7).

CCL2 *subnetwork analysis*

The *CCL2* subnetworks are comprised of the *CCL2* node that is extended out to include all directly connected nodes within three path lengths in the following IBD and control BNs: (1) *CCL2* subnetwork of the CD ileum subnetwork, (2) *CCL2* subnetwork of the CD colon subnetwork, (3) *CCL2* subnetwork of the UC subnetwork, and (4) *CCL2* subnetwork of the control colon subnetwork. Cytoscape (v3.10.2) was used to generate the *CCL2* subnetwork plots.

Primary adult enteric neuron culture

Colonic muscularis externa of 6-wk-old mice was extracted, and single-cell suspensions were prepared as described above. Cells were seeded into (1) Matrigel-coated 24-well plates at a density of 150,000 cells/well or (2) Matrigel-coated 4-well chamber slides at a density of 100,000 cells/well and maintained in complete neuronal culture media containing Neurobasal-A media (Gibco), L-glutamine (200 mM, Gibco), B27 (1×, Gibco), glial-derived neurotrophic factor (10 ng/ml, Shenandoah), FBS (1%), amphotericin B (2.5 µg/ml, Gibco), and penicillin–streptomycin (1%, Gibco). Morphological changes were observed daily, and on days 13–14, differentiated neurons in culture were used for experiments.

Inducible neuron fate mapping *in vitro*

To detect tdTomato expression under control of *Nestin* expression in mature enteric neurons, the following tamoxifen treatment strategies were adopted.

Preculture treatment

Nestin$^{ER\text{-}Cre}$*Rosa26*-STOP$^{fl/fl}$tdTomato mice and their corresponding controls were orally gavaged with 20 mg/ml of tamoxifen for two 5-day cycles with a 5-day break between each cycle. Following this, primary adult enteric neuron cultures were generated using single suspension of cells extracted from colonic muscularis externa as described in the previous section.

Postculture treatment

Nestin$^{ER\text{-}Cre}$*Rosa26*-STOP$^{fl/fl}$tdTomato mice and their corresponding controls were used to generate primary adult enteric neuron cultures as described in the previous section. Fully differentiated neurons were then treated with 4-hydroxytamoxifen (1 µM, H-7904; Sigma-Aldrich) for 24 h *in vitro*.

Chemical hypoxia *in vitro*

$CoCl_2$ was used as a chemical mimetic to simulate hypoxia (Munoz-Sanchez and Chanez-Cardenas, 2019) *in vitro*. Differentiated enteric neuron culture was treated with $CoCl_2$ (200 µM, Sigma-Aldrich) for 12 h followed by treatment with LPS (100 ng/ml, Sigma-Aldrich) or recombinant murine IL-1β (100 ng/ml, #211-11B; PeproTech) for another 9 h. To inhibit HIF1α during chemical hypoxia, differentiated enteric neuron cultures were pretreated with PX-478 (25 µM, #202350; MedKoo Biosciences) for 16 h before inducing chemical hypoxia using $CoCl_2$ for 12 h followed by LPS treatment for 9 h. PX-478 was maintained in the culture by replenishing it every 16 h. At the end of the experiment, cells and supernatants were collected for gene expression and protein analyses.

Protein expression by ELISA

The concentration of fecal lipocalin-2 was measured using the R&D Systems ELISA kit (#DY1857). The concentration of secreted CCL2 in supernatants of cultured enteric neurons was measured using the R&D Systems ELISA kit (#DY479-05). Both ELISAs were performed according to the manufacturer's protocol.

Statistical analyses

ENS remodeling microscopy data analysis

To account for both between-sample and within-sample variability in our "pooled" dataset, we implemented a Nested Leave-One-Out Jackknife strategy (Saravanan et al., 2020). This method takes advantage of information collected from several images within the same mouse without pseudoreplicating them (Lazic, 2010) and offers a more robust estimate of stability in our metrics, particularly when the number of samples is small and common assumptions may not hold.

For each of 1,000 iterations of resampling and within each experimental group, we randomly excluded one mouse and one image in each mouse (i.e., leave-one-out for both levels of data). Among the remaining images per mouse, a median value was calculated, representing a summary measure for each resampled mouse. Subsequently, the median of these mouse-level medians was computed for each group. The $\log_2$ fold change between groups was then calculated to evaluate the difference between these group medians.

This procedure yielded a distribution of $\log_2$ fold change values across the 1,000 iterations. To summarize these results, we reported the median $\log_2$ fold change. We also quantified the stability of the observed group differences by calculating the proportion of iterations in which the direction of the $\log_2$ fold change differed from the overall median $\log_2$ fold change direction, thus providing an empirical P value (Lazic, 2010; Davison and Hinkley, 1997). Results with zero iterations showing the opposite sign of median $\log_2$ fold change of all 1,000 iterations of resampling (i.e., empirical P value <0.001) were considered as significant.

General statistical analysis

General statistical analysis was performed using GraphPad Prism 10 software. All data are presented either as mean ± SEM or as specified in the figure legends. A two-tailed paired or unpaired Student's *t* test was used to determine the statistical significance of differences when comparing means of two groups. One-way and two-way analysis of variance were used (as specified in the figure legends) to determine the statistical significance when comparing >2 groups. Differences between groups were considered statistically significant when values of $P \leq 0.05$.

Online supplemental material

Fig. S1 shows colitis readouts supplementary to Fig. 1 and the methodology for defining myenteric neurons by flow cytometry. Fig. S2 shows *in vitro* validation of *Nes*$^{ER\text{-}Cre}$*R26*-STOP$^{fl/fl}$tdTomato fate-mapping strategy to detect newborn neurons. Fig. S3 shows neurogenesis in the colonic myenteric plexus after colitis, supplementary to Fig. 2. Fig. S4 shows immune cell types and MM subsets in the myenteric plexus at steady state and during colitis by scRNA-seq and flow cytometry. Fig. S5 shows the immune cell composition of the myenteric plexus and gene signatures of MMs at steady state and colitis. Fig. S6 shows the efficacy of CCL2 depletion and intestinal inflammation in SLICK-H$^{ER\text{-}Cre}$*Ccl2*$^{fl/fl}$ mice, supplementary to Fig. 5. Fig. S7 shows the targeting of neurons by the SLICK-H$^{ER\text{-}Cre}$ model. Fig. S8 shows the myenteric plexus remodeling in SLICK-H$^{ER\text{-}Cre}$*Ccl2*$^{fl/fl}$ mice, supplementary to Fig. 5. Fig. S9 shows the negative regulation of CCL2 by HIF1 signaling in cultured myenteric neurons, supplementary to Fig. 6. Fig. S10 shows myenteric inflammation in PX-478–treated mice or mice with neuron-specific depletion of *Myd88*, *Hif1a*, or *Vhl*, supplementary to Fig. 6. Fig. S11 shows mucosal inflammation in PX-478–treated mice or mice with neuron-specific depletion of *Myd88*, *Hif1a*, or *Vhl*, supplementary to Fig. 6. Fig. S12 shows myenteric plexus remodeling in mice with neuron-specific depletion of *Hif1a* or *Vhl*, supplementary to Fig. 6. Table S1 provides the list of mouse colon scRNA-seq cluster markers. Table S2 provides the list of DEGs generated from RNA-seq analysis of

MM subsets isolated from water and 1×DSS-treated mice and compared across two conditions (water versus DSS). Table S3 provides the list of DEGs generated from RNA-seq analysis of MM subsets isolated from 1×DSS-treated mice and compared with each other. Table S4 provides pathway analysis for MM subsets isolated from 1×DSS-treated mice. Table S5 provides identity signatures for MM subsets isolated from 1×DSS-treated mice, supplementary to Table S4. Table S6 provides the computational evidence that MM- and neuron-interacting genes from the normal mouse colon scRNA-seq dataset are conserved in DSS colitis. Table S7 provides the list of genes identified as an inflamed enteric neural gene signature from the ileum of CD patients. Tables S8, S9, S10, and S11 include antibodies for flow cytometry, and primary and secondary antibodies for immunofluorescence and experimental animals. Video 1 shows MMs form direct contacts with enteric neurons in the myenteric ganglia. Video 2 shows MMs engulf enteric neurons in the myenteric ganglia. Video 3 shows MMs contact and engulf enteric neurons in the myenteric ganglia.

Data availability

The data generated from this study were deposited in the NCBI Gene Expression Omnibus under the RNA accession identifiers GSE263945 for subset-specific RNA-seq and GSE266254 for scRNA-seq. The code for the analysis of both RNA-seq datasets was deposited in GitHub: https://github.com/YuLiu-PetersLab/Mount-Sinai/. All data supporting the findings of this study are provided within the article and its supplementary materials. Source data tables for all figures are available upon request. The corresponding author can be contacted for any further clarifications.

Acknowledgments

We thank the Sanderson Center for Optical Experimentation (RRID:SCR_022721) and the Flow Cytometry Core (RRID:SCR_012630) at the University of Massachusetts Chan Medical School for their assistance, and the Genomic Sciences Core (RRID:SCR_021123) and the Advanced Light Microscopy Core (RRID:SCR_022526) at the Penn State University College of Medicine (PSUCoM) for their assistance. We thank Dr. Sean J. Pittock, at Mayo Clinic, Rochester, MN, USA, for providing us aliquots of human serum–containing ANNA-1 antibody. The Genome Sciences Core (RRID:SCR_021123) services and instruments used in this project were funded, in part, by the PSUCoM via the Office of the Vice Dean of Research and Graduate Students and the Pennsylvania Department of Health using tobacco settlement funds (Commonwealth Universal Research Enhancement [CURE]). The content is solely the responsibility of the authors and does not necessarily represent the official views of the University or College of Medicine. The Pennsylvania Department of Health specifically disclaims responsibility for any analyses, interpretations, or conclusions. The content is solely the responsibility of the authors and does not necessarily represent the official views of the University or College of Medicine. The Pennsylvania Department of Health specifically disclaims responsibility for any analyses, interpretations, or conclusions. The library preparation and scRNA-seq of colonic cells were performed at the Single Cell and Transcriptomics Core at the Johns Hopkins University.

This work was supported by Junior Faculty Research Scholar Award by PSUCoM and Pennsylvania Department of Health using tobacco CURE funds (M. Bogunovic), Kenneth Rainin Foundation Innovation Award (M. Bogunovic), National Institutes of Health (NIH)-National Institute of Allergy and Infectious Diseases R21AI126351-01 (M. Bogunovic), NIH-National Institute of Diabetes and Digestive and Kidney Diseases (NIDDK) R01DK107603 (M. Bogunovic), NIH-National Institute on Aging (NIA) R01AG066768 (S. Kulkarni), NIH-NIA R21AG072107 (S. Kulkarni), NIH-National Institute of Neurological Disorders and Stroke R01NS112492 (T. Thomson), the Harvard Digestive Disease Center Pilot and Feasibility Award (S. Kulkarni), NIH-NIDDK R01DK080684 (S. Srinivasan), the computational and data resources and staff expertise provided by Scientific Computing and Data at the Icahn School of Medicine at Mount Sinai (L.A. Peters), the Clinical and Translational Science Award grant UL1TR004419 from the National Center for Advancing Translational Sciences (L.A. Peters), and in part The Leona M. and Harry B. Helmsley Charitable Trust (L.A. Peters). The Advanced Light Microscopy Core (RRID:SCR_022526) and instruments used in this project were funded, in part, by the PSUCoM via the Office of the Vice Dean of Research and Graduate Students and the Pennsylvania Department of Health using tobacco settlement funds (CURE).

Author contributions: Sravya Kurapati: conceptualization, data curation, formal analysis, investigation, methodology, project administration, software, validation, visualization, and writing—original draft, review, and editing. Changsik Shin: conceptualization, data curation, formal analysis, investigation, methodology, project administration, resources, validation, visualization, and writing—original draft, review, and editing. Krisztina Szabo: formal analysis, investigation, visualization, and writing—original draft, review, and editing. Yu Liu: data curation and software. Azree Z. Ashraf: formal analysis and investigation. Balazs Koscso: formal analysis and investigation. Chinmayee Dash: methodology. Katherine L. Kruckow: investigation and writing—review and editing. Leonardo E. Navarro: data curation and investigation. Amanda M. Clark: formal analysis, methodology, software, and writing—original draft, review, and editing. Monalee Saha: data curation. Sushma Nagaraj: formal analysis. Wenhui Wang: resources. Jun Zhu: methodology. Kevin Brown: conceptualization, methodology, supervision, and writing—review and editing. Travis Thomson: software. Natalia Shulzhenko: formal analysis, methodology, and validation. Andrey Morgun: methodology, software, and writing—review and editing. Christina E. Baer: formal analysis and software. Shanthi Srinivasan: methodology. Subhash Kulkarni: conceptualization and writing—review and editing. Pankaj J. Pasricha: conceptualization, data curation, formal analysis, methodology, and writing—review and editing. Lauren A. Peters: conceptualization, data curation, formal analysis, funding acquisition, investigation, methodology, project administration, resources, supervision, validation, visualization, and writing—original draft, review, and editing. Milena

Bogunovic: conceptualization, data curation, formal analysis, funding acquisition, investigation, methodology, project administration, resources, supervision, validation, visualization, and writing—original draft, review, and editing.

Disclosures: M. Bogunovic reported grants from Bristol Myers Squibb, personal fees from Takeda, and personal fees from Boehringer Ingelheim during the conduct of the study. No other disclosures were reported.

Submitted: 28 August 2025
Revised: 8 October 2025
Accepted: 19 December 2025

References

Argmann, C., M. Tokuyama, R.C. Ungaro, R. Huang, R. Hou, S. Gurunathan, R. Kosoy, A. Di'Narzo, W. Wang, B. Losic, et al. 2021. Molecular characterization of limited ulcerative colitis reveals novel biology and predictors of disease extension. *Gastroenterology*. 161:1953–1968.e15. https://doi.org/10.1053/j.gastro.2021.08.053

Babickova, J., L. Tothova, E. Lengyelova, A. Bartonova, J. Hodosy, R. Gardlik, and P. Celec. 2015. Sex differences in experimentally induced colitis in mice: A role for estrogens. *Inflammation*. 38:1996–2006. https://doi.org/10.1007/s10753-015-0180-7

Bain, C.C., A. Bravo-Blas, C.L. Scott, E. Gomez Perdiguero, F. Geissmann, S. Henri, B. Malissen, L.C. Osborne, D. Artis, and A.M. Mowat. 2014. Constant replenishment from circulating monocytes maintains the macrophage pool in the intestine of adult mice. *Nat. Immunol.* 15: 929–937. https://doi.org/10.1038/ni.2967

Bais, A.S., and D. Kostka. 2020. scds: Computational annotation of doublets in single-cell RNA sequencing data. *Bioinformatics*. 36:1150–1158. https://doi.org/10.1093/bioinformatics/btz698

Baltar, J., R.M. Miranda, M. Cabral, S. Rebelo, F. Grahammer, T.B. Huber, C. Reguenga, and F.A. Monteiro. 2024. Nephl is required for neurite branching and is negatively regulated by the PRRXL1 homeodomain factor in the developing spinal cord dorsal horn. *Neural Dev.* 19:13. https://doi.org/10.1186/s13064-024-00190-6

Belkina, A.C., C.O. Ciccolella, R. Anno, R. Halpert, J. Spidlen, and J.E. Snyder-Cappione. 2019. Automated optimized parameters for T-distributed stochastic neighbor embedding improve visualization and analysis of large datasets. *Nat. Commun.* 10:5415. https://doi.org/10.1038/s41467-019-13055-y

Belkind-Gerson, J., A. Carreon-Rodriguez, L.A. Benedict, C. Steiger, A. Pieretti, N. Nagy, J. Dietrich, and A.M. Goldstein. 2013. Nestin-expressing cells in the gut give rise to enteric neurons and glial cells. *Neurogastroenterol. Motil.* 25:61–69.e7. https://doi.org/10.1111/nmo.12015

Belkind-Gerson, J., R. Hotta, N. Nagy, A.R. Thomas, H. Graham, L. Cheng, J. Solorzano, D. Nguyen, M. Kamionek, J. Dietrich, et al. 2015. Colitis induces enteric neurogenesis through a 5-HT4-dependent mechanism. *Inflamm. Bowel Dis.* 21:870–878. https://doi.org/10.1097/MIB.0000000000000326

Berg, D.J., N. Davidson, R. Kühn, W. Müller, S. Menon, G. Holland, L. Thompson-Snipes, M.W. Leach, and D. Rennick. 1996. Enterocolitis and colon cancer in interleukin-10-deficient mice are associated with aberrant cytokine production and CD4(+) TH1-like responses. *J. Clin. Invest.* 98:1010–1020. https://doi.org/10.1172/JCI118861

Bleriot, C., S. Chakarov, and F. Ginhoux. 2020. Determinants of resident tissue macrophage identity and function. *Immunity*. 52: 957–970. https://doi.org/10.1016/j.immuni.2020.05.014

Bogunovic, M., F. Ginhoux, J. Helft, L. Shang, D. Hashimoto, M. Greter, K. Liu, C. Jakubzick, M.A. Ingersoll, M. Leboeuf, et al. 2009. Origin of the lamina propria dendritic cell network. *Immunity*. 31:513–525. https://doi.org/10.1016/j.immuni.2009.08.010

Bolger, A.M., M. Lohse, and B. Usadel. 2014. Trimmomatic: A flexible trimmer for illumina sequence data. *Bioinformatics*. 30:2114–2120. https://doi.org/10.1093/bioinformatics/btu170

Brierley, S.M., and D.R. Linden. 2014. Neuroplasticity and dysfunction after gastrointestinal inflammation. *Nat. Rev. Gastroenterol. Hepatol.* 11:611–627. https://doi.org/10.1038/nrgastro.2014.103

Butler, A., P. Hoffman, P. Smibert, E. Papalexi, and R. Satija. 2018. Integrating single-cell transcriptomic data across different conditions, technologies, and species. *Nat. Biotechnol.* 36:411–420. https://doi.org/10.1038/nbt.4096

Camilleri, M., and D.R. Linden. 2016. Measurement of gastrointestinal and colonic motor functions in humans and animals. *Cell Mol. Gastroenterol. Hepatol.* 2:412–428. https://doi.org/10.1016/j.jcmgh.2016.04.003

Cao, M., P. Chen, B. Peng, Y. Cheng, J. Xie, Z. Hou, H. Chen, L. Ye, H. Li, H. Wang, et al. 2023. The transcription factor ELF4 alleviates inflammatory bowel disease by activating IL1RN transcription, suppressing inflammatory TH17 cell activity, and inducing macrophage M2 polarization. *Front. Immunol.* 14:1270411. https://doi.org/10.3389/fimmu.2023.1270411

Cao, M., W. Xu, J. Yu, H. Zheng, X. Tan, L. Li, Y. Rui, G. Xu, G. Cui, J. Xu, et al. 2013. Up-regulation of SGTB is associated with neuronal apoptosis after neuroinflammation induced by lipopolysaccharide. *J. Mol. Histol.* 44:507–518. https://doi.org/10.1007/s10735-013-9517-4

Chang, S.L., R.H. Chou, H.J. Zeng, Y.H. Lin, T.Y. Chiu, D.M. Yang, S.C. Hung, C.H. Lai, J.T. Hsieh, W.C. Shyu, and Y.L. Yu. 2013. Downregulation of DAB2IP promotes mesenchymal-to-neuroepithelial transition and neuronal differentiation of human mesenchymal stem cells. *PLoS One*. 8: e75884. https://doi.org/10.1371/journal.pone.0075884

Chassaing, B., J.D. Aitken, M. Malleshappa, and M. Vijay-Kumar. 2014. Dextran sulfate sodium (DSS)-induced colitis in mice. *Curr. Protoc. Immunol.* 104:15.25.1–15.25.14. https://doi.org/10.1002/0471142735.im1525s104

Chassaing, B., G. Srinivasan, M.A. Delgado, A.N. Young, A.T. Gewirtz, and M. Vijay-Kumar. 2012. Fecal lipocalin 2, a sensitive and broadly dynamic non-invasive biomarker for intestinal inflammation. *PLoS One*. 7: e44328. https://doi.org/10.1371/journal.pone.0044328

Chen, E.Y., C.M. Tan, Y. Kou, Q. Duan, Z. Wang, G.V. Meirelles, N.R. Clark, and A. Ma'ayan. 2013. Enrichr: Interactive and collaborative HTML5 gene list enrichment analysis tool. *BMC Bioinformatics*. 14:128. https://doi.org/10.1186/1471-2105-14-128

Colgan, S.P., E.L. Campbell, and D.J. Kominsky. 2016. Hypoxia and mucosal inflammation. *Annu. Rev. Pathol.* 11:77–100. https://doi.org/10.1146/annurev-pathol-012615-044231

Collins, S.M. 2014. A role for the gut microbiota in IBS. *Nat. Rev. Gastroenterol. Hepatol.* 11:497–505. https://doi.org/10.1038/nrgastro.2014.40

Davison, A.C., and D.V. Hinkley. 1997. Bootstrap Methods and Their Application. Cambridge University Press, Cambridge; New York, NY.

De Schepper, S., S. Verheijden, J. Aguilera-Lizarraga, M.F. Viola, W. Boesmans, N. Stakenborg, I. Voytyuk, I. Schmidt, B. Boeckx, I. Dierckx De Casterle, et al. 2019. Self-maintaining gut macrophages are essential for intestinal homeostasis. *Cell*. 176:676. https://doi.org/10.1016/j.cell.2019.01.010

Dengler, V.L., M. Galbraith, and J.M. Espinosa. 2014. Transcriptional regulation by hypoxia inducible factors. *Crit. Rev. Biochem. Mol. Biol.* 49:1–15. https://doi.org/10.3109/10409238.2013.838205

Dick, S.A., A. Wong, H. Hamidzada, S. Nejat, R. Nechanitzky, S. Vohra, B. Mueller, R. Zaman, C. Kantores, L. Aronoff, et al. 2022. Three tissue resident macrophage subsets coexist across organs with conserved origins and life cycles. *Sci. Immunol.* 7:eabf7777. https://doi.org/10.1126/sciimmunol.abf7777

Dobin, A., C.A. Davis, F. Schlesinger, J. Drenkow, C. Zaleski, S. Jha, P. Batut, M. Chaisson, and T.R. Gingeras. 2013. STAR: Ultrafast universal RNA-seq aligner. *Bioinformatics*. 29:15–21. https://doi.org/10.1093/bioinformatics/bts635

Feng, Y., C. Zhou, F. Zhao, T. Ma, Y. Xiao, K. Peng, and R. Xia. 2024. ZEB2 alleviates Hirschsprung's-associated enterocolitis by promoting the proliferation and differentiation of enteric neural precursor cells via the notch-1/Jagged-2 pathway. *Gene*. 912:148365. https://doi.org/10.1016/j.gene.2024.148365

Forster, P.M., M.O. Jakob, D. Yusuf, M. Bubeck, H. Limberger, Y. Luo, P. Thieme, A. Polici, N. Sterczyk, S. Boulekou, et al. 2025. A transcriptional atlas of gut-innervating neurons reveals activation of interferon signaling and ferroptosis during intestinal inflammation. *Neuron*. 113: 1333–1351.e7. https://doi.org/10.1016/j.neuron.2025.02.018

Forsythe, J.A., B.H. Jiang, N.V. Iyer, F. Agani, S.W. Leung, R.D. Koos, and G.L. Semenza. 1996. Activation of vascular endothelial growth factor gene transcription by hypoxia-inducible factor 1. *Mol. Cell Biol.* 16:4604–4613. https://doi.org/10.1128/MCB.16.9.4604

Fung, C., T. Venneman, A.M. Holland, T. Martens, M.I. Alata, M.M. Hao, C. Alar, Y. Obata, J. Tack, A. Sifrim, et al. 2025. Nutrients activate distinct patterns of small-intestinal enteric neurons. *Nature*. 644:1069–1077. https://doi.org/10.1038/s41586-025-09228-z

Furness, J.B. 2012. The enteric nervous system and neurogastroenterology. *Nat. Rev. Gastroenterol. Hepatol.* 9:286–294. https://doi.org/10.1038/nrgastro.2012.32

Gabanyi, I., P.A. Muller, L. Feighery, T.Y. Oliveira, F.A. Costa-Pinto, and D. Mucida. 2016. Neuro-immune interactions drive tissue programming in intestinal macrophages. *Cell*. 164:378–391. https://doi.org/10.1016/j.cell.2015.12.023

Galili, T., A. O'Callaghan, J. Sidi, and C. Sievert. 2018. heatmaply: An R package for creating interactive cluster heatmaps for online publishing. *Bioinformatics*. 34:1600–1602. https://doi.org/10.1093/bioinformatics/btx657

Germain, P.L., A. Lun, C. Garcia Meixide, W. Macnair, and M.D. Robinson. 2021. Doublet identification in single-cell sequencing data using. *F1000Res.* 10:979. https://doi.org/10.12688/f1000research.73600.2

Gomez Ramos, B., J. Ohnmacht, N. de Lange, E. Valceschini, A. Ginolhac, M. Catillon, D. Ferrante, A. Rakovic, R. Halder, F. Massart, et al. 2024. Multiomics analysis identifies novel facilitators of human dopaminergic neuron differentiation. *EMBO Rep.* 25:254–285. https://doi.org/10.1038/s44319-023-00024-2

Gonzales, J., C. Le Berre-Scoul, A. Dariel, P. Bréhéret, M. Neunlist, and H. Boudin. 2020. Semaphorin 3A controls enteric neuron connectivity and is inversely associated with synapsin 1 expression in Hirschsprung disease. *Sci. Rep.* 10:15119. https://doi.org/10.1038/s41598-020-71865-3

Graubert, A., F. Aguet, A. Ravi, K.G. Ardlie, and G. Getz. 2021. RNA-SeQC 2: Efficient RNA-seq quality control and quantification for large cohorts. *Bioinformatics*. 37:3048–3050. https://doi.org/10.1093/bioinformatics/btab135

GrubišIć, V., A.L. Perez-Medina, D.E. Fried, J. Sévigny, S.C. Robson, J.J. Galligan, and B.D. Gulbransen. 2019. NTPDase1 and -2 are expressed by distinct cellular compartments in the mouse colon and differentially impact colonic physiology and function after DSS colitis. *Am. J. Physiol. Gastrointest. Liver Physiol.* 317:G314–G332. https://doi.org/10.1152/ajpgi.00104.2019

Gu, P., M.E. Kuenzig, G.G. Kaplan, M. Pimentel, and A. Rezaie. 2018. Fecal incontinence in inflammatory bowel disease: A systematic review and meta-analysis. *Inflamm. Bowel Dis.* 24:1280–1290. https://doi.org/10.1093/ibd/izx109

Gulbransen, B.D., M. Bashashati, S.A. Hirota, X. Gui, J.A. Roberts, J.A. Macdonald, D.A. Muruve, D.M. Mckay, P.L. Beck, G.M. Mawe, et al. 2012. Activation of neuronal P2X7 receptor-pannexin-1 mediates death of enteric neurons during colitis. *Nat. Med.* 18:600–604. https://doi.org/10.1038/nm.2679

Guo, S., Q. Lei, Q. Yang, and R. Chen. 2024. IGFBP5 promotes neuronal apoptosis in a 6-OHDA-toxicant model of Parkinson's disease by inhibiting the sonic hedgehog signaling pathway. *Med. Princ. Pract.* 33:269–280. https://doi.org/10.1159/000538467

Hao, Y., T. Stuart, M.H. Kowalski, S. Choudhary, P. Hoffman, A. Hartman, A. Srivastava, G. Molla, S. Madad, C. Fernandez-Granda, and R. Satija. 2024. Dictionary learning for integrative, multimodal and scalable single-cell analysis. *Nat. Biotechnol.* 42:293–304. https://doi.org/10.1038/s41587-023-01767-y

He, S., J. Wang, Y. Huang, F. Kong, R. Yang, Y. Zhan, Z. Li, C. Ye, L. Meng, Y. Ren, et al. 2023. Intestinal fibrosis in aganglionic segment of Hirschsprung's disease revealed by single-cell RNA sequencing. *Clin. Transl. Med.* 13:e1193. https://doi.org/10.1002/ctm2.1193

Healy, L.M., G. Perron, S.Y. Won, M.A. Michell-Robinson, A. Rezk, S.K. Ludwin, C.S. Moore, J.A. Hall, A. Bar-Or, and J.P. Antel. 2016. MerTK is a functional regulator of myelin phagocytosis by human myeloid cells. *J. Immunol.* 196:3375–3384. https://doi.org/10.4049/jimmunol.1502562

Hoffman, G.E., and E.E. Schadt. 2016. variancePartition: Interpreting drivers of variation in complex gene expression studies. *BMC Bioinformatics*. 17:483. https://doi.org/10.1186/s12859-016-1323-z

Hou, B., B. Reizis, and A.L. Defranco. 2008. Toll-like receptors activate innate and adaptive immunity by using dendritic cell-intrinsic and -extrinsic mechanisms. *Immunity*. 29:272–282. https://doi.org/10.1016/j.immuni.2008.05.016

Huang, D.W., B.T. Sherman, and R.A. Lempicki. 2009. Systematic and integrative analysis of large gene lists using DAVID bioinformatics resources. *Nat. Protoc.* 4:44–57. https://doi.org/10.1038/nprot.2008.211

Jha, M.K., G.J. Song, M.G. Lee, N.H. Jeoung, Y. Go, R.A. Harris, D.H. Park, H. Kook, I.K. Lee, and K. Suk. 2015. Metabolic connection of inflammatory pain: Pivotal role of a pyruvate dehydrogenase kinase-pyruvate dehydrogenase-lactic acid axis. *J. Neurosci.* 35:14353–14369. https://doi.org/10.1523/JNEUROSCI.1910-15.2015

Jian, H., B. Liu, and J. Zhang. 2014. Hypoxia and hypoxia-inducible factor 1 repress SEMA4B expression to promote non-small cell lung cancer invasion. *Tumour Biol.* 35:4949–4955. https://doi.org/10.1007/s13277-014-1651-4

Jiang, T., J. Zhuang, H. Duan, Y. Luo, Q. Zeng, K. Fan, H. Yan, D. Lu, Z. Ye, J. Hao, et al. 2012. CD146 is a coreceptor for VEGFR-2 in tumor angiogenesis. *Blood*. 120:2330–2339. https://doi.org/10.1182/blood-2012-01-406108

Jin, S., C.F. Guerrero-Juarez, L. Zhang, I. Chang, R. Ramos, C.H. Kuan, P. Myung, M.V. Plikus, and Q. Nie. 2021. Inference and analysis of cell-cell communication using CellChat. *Nat. Commun.* 12:1088. https://doi.org/10.1038/s41467-021-21246-9

Jung, S., J. Aliberti, P. Graemmel, M.J. Sunshine, G.W. Kreutzberg, A. Sher, and D.R. Littman. 2000. Analysis of fractalkine receptor CX(3)CR1 function by targeted deletion and green fluorescent protein reporter gene insertion. *Mol. Cell Biol.* 20:4106–4114. https://doi.org/10.1128/MCB.20.11.4106-4114.2000

Kacmaz, H., A. Alto, K. Knutson, D.R. Linden, S.J. Gibbons, G. Farrugia, and A. Beyder. 2021. A simple automated approach to measure mouse whole gut transit. *Neurogastroenterol. Motil.* 33:e13994. https://doi.org/10.1111/nmo.13994

Karhausen, J., G.T. Furuta, J.E. Tomaszewski, R.S. Johnson, S.P. Colgan, and V.H. Haase. 2004. Epithelial hypoxia-inducible factor-1 is protective in murine experimental colitis. *J. Clin. Invest.* 114:1098–1106. https://doi.org/10.1172/JCI21086

Keller, J., C. Beglinger, J.J. Holst, V. Andresen, and P. Layer. 2009. Mechanisms of gastric emptying disturbances in chronic and acute inflammation of the distal gastrointestinal tract. *Am. J. Physiol. Gastrointest. Liver Physiol.* 297:G861–G868. https://doi.org/10.1152/ajpgi.00145.2009

Kim, N., Y. Li, R. Yu, H.S. Kwon, A. Song, M.H. Jun, J.Y. Jeong, J.H. Lee, H.H. Lim, M.J. Kim, et al. 2024. Repulsive Sema3E-Plexin-D1 signaling coordinates both axonal extension and steering via activating an autoregulatory factor, Mtss1. *Elife*. 13:e96891. https://doi.org/10.7554/eLife.96891

Koch, C.J. 2002. Measurement of absolute oxygen levels in cells and tissues using oxygen sensors and 2-nitroimidazole EF5. *Methods Enzymol.* 352:3–31. https://doi.org/10.1016/s0076-6879(02)52003-6

Koscso, B., and M. Bogunovic. 2016. Analysis and purification of mouse intestinal dendritic cell and macrophage subsets by flow cytometry. *Curr. Protoc. Immunol.* 114:14.39.1–14 39.14. https://doi.org/10.1002/cpim.11

Koscso, B., K. Gowda, T.D. Schell, and M. Bogunovic. 2015. Purification of dendritic cell and macrophage subsets from the normal mouse small intestine. *J. Immunol. Methods*. 421:1–13. https://doi.org/10.1016/j.jim.2015.02.013

Koscso, B., S. Kurapati, R.R. Rodrigues, J. Nedjic, K. Gowda, C. Shin, C. Soni, A.Z. Ashraf, I. Purushothaman, M. Palisoc, et al. 2020. Gut-resident CX3CR1(hi) macrophages induce tertiary lymphoid structures and IgA response in situ. *Sci. Immunol.* 5:eaax0062. https://doi.org/10.1126/sciimmunol.aax0062

Kühn, R., J. Löhler, D. Rennick, K. Rajewsky, and W. Müller. 1993. Interleukin-10-deficient mice develop chronic enterocolitis. *Cell*. 75:263–274. https://doi.org/10.1016/0092-8674(93)80068-p

Kuleshov, M.V., M.R. Jones, A.D. Rouillard, N.F. Fernandez, Q. Duan, Z. Wang, S. Koplev, S.L. Jenkins, K.M. Jagodnik, A. Lachmann, et al. 2016. Enrichr: A comprehensive gene set enrichment analysis web server 2016 update. *Nucleic Acids Res.* 44:W90–W97. https://doi.org/10.1093/nar/gkw377

Kulkarni, S., M.A. Micci, J. Leser, C. Shin, S.C. Tang, Y.Y. Fu, L. Liu, Q. Li, M. Saha, C. Li, et al. 2017. Adult enteric nervous system in health is maintained by a dynamic balance between neuronal apoptosis and neurogenesis. *Proc. Natl. Acad. Sci. USA*. 114:E3709–E3718. https://doi.org/10.1073/pnas.1619406114

Kulkarni, S., M. Saha, J. Slosberg, A. Singh, S. Nagaraj, L. Becker, C. Zhang, A. Bukowski, Z. Wang, G. Liu, et al. 2023. Age-associated changes in lineage composition of the enteric nervous system regulate gut health and disease. *Elife*. 12:RP88051. https://doi.org/10.7554/eLife.88051

Kulkarni, S., S. Kurapati, and M. Bogunovic. 2021. Neuro-innate immune interactions in gut mucosal immunity. *Curr. Opin. Immunol.* 68:64–71. https://doi.org/10.1016/j.coi.2020.09.007

Kurahashi, M., H. Zheng, L. Dwyer, S.M. Ward, S.D. Koh, and K.M. Sanders. 2011. A functional role for the 'fibroblast-like cells' in gastrointestinal smooth muscles. *J. Physiol.* 589:697–710. https://doi.org/10.1113/jphysiol.2010.201129

Laddach, A., S.H. Chng, R. Lasrado, F. Progatzky, M. Shapiro, A. Erickson, M. Sampedro Castaneda, A.V. Artemov, A.C. Bon-Frauches, E.M. Amaniti, et al. 2023. A branching model of lineage differentiation underpinning

the neurogenic potential of enteric glia. *Nat. Commun.* 14:5904. https://doi.org/10.1038/s41467-023-41492-3

Lagace, D.C., M.C. Whitman, M.A. Noonan, J.L. Ables, N.A. Decarolis, A.A. Arguello, M.H. Donovan, S.J. Fischer, L.A. Farnbauch, R.D. Beech, et al. 2007. Dynamic contribution of nestin-expressing stem cells to adult neurogenesis. *J. Neurosci.* 27:12623–12629. https://doi.org/10.1523/JNEUROSCI.3812-07.2007

Lakner, J., C. Seyer, T. Hermsdorf, and T. Schöneberg. 2011. Characterization of the expression, promoter activity and molecular architecture of fibin. *BMC Biochem.* 12:26. https://doi.org/10.1186/1471-2091-12-26

Lazic, S.E. 2010. The problem of pseudoreplication in neuroscientific studies: Is it affecting your analysis? *BMC Neurosci.* 11:5. https://doi.org/10.1186/1471-2202-11-5

Li, Z.L., B. Wang, L.L. Lv, T.T. Tang, Y. Wen, J.Y. Cao, X.X. Zhu, S.T. Feng, S.D. Crowley, and B.C. Liu. 2021. FIH-1-modulated HIF-1α C-TAD promotes acute kidney injury to chronic kidney disease progression via regulating KLF5 signaling. *Acta Pharmacol. Sin.* 42:2106–2119. https://doi.org/10.1038/s41401-021-00617-4

Linden, D.R., K.A. Sharkey, and G.M. Mawe. 2003. Enhanced excitability of myenteric AH neurones in the inflamed guinea-pig distal colon. *J. Physiol.* 547:589–601. https://doi.org/10.1113/jphysiol.2002.035147

Madisen, L., T.A. Zwingman, S.M. Sunkin, S.W. Oh, H.A. Zariwala, H. Gu, L.L. Ng, R.D. Palmiter, M.J. Hawrylycz, A.R. Jones, et al. 2010. A robust and high-throughput Cre reporting and characterization system for the whole mouse brain. *Nat. Neurosci.* 13:133–140. https://doi.org/10.1038/nn.2467

Margolis, K.G., M.D. Gershon, and M. Bogunovic. 2016. Cellular organization of neuroimmune interactions in the gastrointestinal tract. *Trends Immunol.* 37:487–501. https://doi.org/10.1016/j.it.2016.05.003

Martin, J.C., C. Chang, G. Boschetti, R. Ungaro, M. Giri, J.A. Grout, K. Gettler, L.S. Chuang, S. Nayar, A.J. Greenstein, et al. 2019. Single-cell analysis of Crohn's disease lesions identifies a pathogenic cellular module associated with resistance to anti-TNF therapy. *Cell.* 178:1493–1508.e20. https://doi.org/10.1016/j.cell.2019.08.008

Matenia, D., and E.M. Mandelkow. 2009. The tau of MARK: A polarized view of the cytoskeleton. *Trends Biochem. Sci.* 34:332–342. https://doi.org/10.1016/j.tibs.2009.03.008

Matheis, F., P.A. Muller, C.L. Graves, I. Gabanyi, Z.J. Kerner, D. Costa-Borges, T. Ahrends, P. Rosenstiel, and D. Mucida. 2020. Adrenergic signaling in muscularis macrophages limits infection-induced neuronal loss. *Cell.* 180:64–78.e16. https://doi.org/10.1016/j.cell.2019.12.002

Matsuda, S., Y. Matsuda, and L. D'Adamio. 2009. CD74 interacts with APP and suppresses the production of Abeta. *Mol. Neurodegener.* 4:41. https://doi.org/10.1186/1750-1326-4-41

Mawe, G.M. 2015. Colitis-induced neuroplasticity disrupts motility in the inflamed and post-inflamed colon. *J. Clin. Invest.* 125:949–955. https://doi.org/10.1172/JCI76306

Mcginnis, C.S., L.M. Murrow, and Z.J. Gartner. 2019. DoubletFinder: Doublet detection in single-cell RNA sequencing data using artificial nearest neighbors. *Cell Syst.* 8:329–337.e4. https://doi.org/10.1016/j.cels.2019.03.003

Melo, C.G.S., E.N. Nicolai, C. Alcaino, T.J. Cassmann, S.T. Whiteman, A.M. Wright, K.E. Miller, S.J. Gibbons, A. Beyder, and D.R. Linden. 2020. Identification of intrinsic primary afferent neurons in mouse jejunum. *Neurogastroenterol. Motil.* 32:e13989. https://doi.org/10.1111/nmo.13989

Miller, J.C., B.D. Brown, T. Shay, E.L. Gautier, V. Jojic, A. Cohain, G. Pandey, M. Leboeuf, K.G. Elpek, J. Helft, et al. 2012. Deciphering the transcriptional network of the dendritic cell lineage. *Nat. Immunol.* 13:888–899. https://doi.org/10.1038/ni.2370

Mojsilovic-Petrovic, J., D. Callaghan, H. Cui, C. Dean, D.B. Stanimirovic, and W. Zhang. 2007. Hypoxia-inducible factor-1 (HIF-1) is involved in the regulation of hypoxia-stimulated expression of monocyte chemoattractant protein-1 (MCP-1/CCL2) and MCP-5 (Ccl12) in astrocytes. *J. Neuroinflammation.* 4:12. https://doi.org/10.1186/1742-2094-4-12

Mondal, B., H. Jin, S. Kallappagoudar, Y. Sedkov, T. Martinez, M.F. Sentmanat, G.J. Poet, C. Li, Y. Fan, S.M. Pruett-Miller, and H.M. Herz. 2020. The histone deacetylase complex MiDAC regulates a neurodevelopmental gene expression program to control neurite outgrowth. *Elife.* 9:e57519. https://doi.org/10.7554/eLife.57519

Morarach, K., A. Mikhailova, V. Knoflach, F. Memic, R. Kumar, W. Li, P. Ernfors, and U. Marklund. 2021. Diversification of molecularly defined myenteric neuron classes revealed by single-cell RNA sequencing. *Nat. Neurosci.* 24:34–46. https://doi.org/10.1038/s41593-020-00736-x

Muller, P.A., B. Koscso, G.M. Rajani, K. Stevanovic, M.L. Berres, D. Hashimoto, A. Mortha, M. Leboeuf, X.M. Li, D. Mucida, et al. 2014. Crosstalk between muscularis macrophages and enteric neurons regulates gastrointestinal motility. *Cell.* 158:300–313. https://doi.org/10.1016/j.cell.2014.04.050

Munoz-Sanchez, J., and M.E. Chanez-Cardenas. 2019. The use of cobalt chloride as a chemical hypoxia model. *J. Appl. Toxicol.* 39:556–570. https://doi.org/10.1002/jat.3749

Nozaki, K., V.I. Maltez, M. Rayamajhi, A.L. Tubbs, J.E. Mitchell, C.A. Lacey, C.K. Harvest, L. Li, W.T. Nash, H.N. Larson, et al. 2022. Caspase-7 activates ASM to repair gasdermin and perforin pores. *Nature.* 606:960–967. https://doi.org/10.1038/s41586-022-04825-8

Ohman, L., and M. Simren. 2010. Pathogenesis of IBS: Role of inflammation, immunity and neuroimmune interactions. *Nat. Rev. Gastroenterol. Hepatol.* 7:163–173. https://doi.org/10.1038/nrgastro.2010.4

Olbe, L. 2008. Concept of Crohn's disease being conditioned by four main components, and irritable bowel syndrome being an incomplete Crohn's disease. *Scand. J. Gastroenterol.* 43:234–241. https://doi.org/10.1080/00365520701676971

Oshima, K., N. Siddiqui, J.E. Orfila, D. Carter, J. Laing, X. Han, I. Zakharevich, R.V. Iozzo, A. Ghasabyan, H. Moore, et al. 2024. A role for decorin in improving motor deficits after traumatic brain injury. *Matrix Biol.* 125:88–99. https://doi.org/10.1016/j.matbio.2023.12.005

Ou, Y.N., Y.X. Yang, Y.T. Deng, C. Zhang, H. Hu, B.S. Wu, Y. Liu, Y.J. Wang, Y. Zhu, J. Suckling, et al. 2021. Identification of novel drug targets for Alzheimer's disease by integrating genetics and proteomes from brain and blood. *Mol. Psychiatry.* 26:6065–6073. https://doi.org/10.1038/s41380-021-01251-6

Park, M.D., A. Silvin, F. Ginhoux, and M. Merad. 2022. Macrophages in health and disease. *Cell.* 185:4259–4279. https://doi.org/10.1016/j.cell.2022.10.007

Peters, L.A., J.R. Friedman, A. Stojmirovic, J. Hagen, S. Houten, T. Dodatko, M.P. Amaro, P. Restrepo, Z. Chai, J. Rodrigo Mora, et al. 2023. A temporal classifier predicts histopathology state and parses acute-chronic phasing in inflammatory bowel disease patients. *Commun. Biol.* 6:95. https://doi.org/10.1038/s42003-023-04469-y

Peters, L.A., J. Perrigoue, A. Mortha, A. Iuga, W.M. Song, E.M. Neiman, S.R. Llewellyn, A. Di Narzo, B.A. Kidd, S.E. Telesco, et al. 2017. A functional genomics predictive network model identifies regulators of inflammatory bowel disease. *Nat. Genet.* 49:1437–1449. https://doi.org/10.1038/ng.3947

Phillips, R.J., and T.L. Powley. 2012. Macrophages associated with the intrinsic and extrinsic autonomic innervation of the rat gastrointestinal tract. *Auton. Neurosci.* 169:12–27. https://doi.org/10.1016/j.autneu.2012.02.004

Qian, Y., L. Yang, J. Chen, C. Zhou, N. Zong, Y. Geng, S. Xia, H. Yang, X. Bao, Y. Chen, and Y. Xu. 2024. SRGN amplifies microglia-mediated neuroinflammation and exacerbates ischemic brain injury. *J. Neuroinflammation.* 21:35. https://doi.org/10.1186/s12974-024-03026-6

Rasmussen, S., T.H. Jensen, S.L. Henriksen, P.F. Haastrup, P.V. Larsen, J. Sondergaard, and D.E. Jarbol. 2015. Overlap of symptoms of gastroesophageal reflux disease, dyspepsia and irritable bowel syndrome in the general population. *Scand. J. Gastroenterol.* 50:162–169. https://doi.org/10.3109/00365521.2014.983157

Reichardt, L.F., and K.J. Tomaselli. 1991. Extracellular matrix molecules and their receptors: Functions in neural development. *Annu. Rev. Neurosci.* 14:531–570. https://doi.org/10.1146/annurev.ne.14.030191.002531

Rezaie, A., P. Gu, G.G. Kaplan, M. Pimentel, and A.K. Al-Darmaki. 2018. Dyssynergic defecation in inflammatory bowel disease: A systematic review and meta-analysis. *Inflamm. Bowel Dis.* 24:1065–1073. https://doi.org/10.1093/ibd/izx095

Robinson, A., S. Keely, J. Karhausen, M.E. Gerich, G.T. Furuta, and S.P. Colgan. 2008. Mucosal protection by hypoxia-inducible factor prolyl hydroxylase inhibition. *Gastroenterology.* 134:145–155. https://doi.org/10.1053/j.gastro.2007.09.033

Robinson, M.D., and G.K. Smyth. 2007. Moderated statistical tests for assessing differences in tag abundance. *Bioinformatics.* 23:2881–2887. https://doi.org/10.1093/bioinformatics/btm453

Ryan, H.E., M. Poloni, W. Mcnulty, D. Elson, M. Gassmann, J.M. Arbeit, and R.S. Johnson. 2000. Hypoxia-inducible factor-1alpha is a positive factor in solid tumor growth. *Cancer Res.* 60:4010–4015.

Saederup, N., A.E. Cardona, K. Croft, M. Mizutani, A.C. Cotleur, C.L. Tsou, R.M. Ransohoff, and I.F. Charo. 2010. Selective chemokine receptor usage by central nervous system myeloid cells in CCR2-red fluorescent protein knock-in mice. *PLoS One.* 5:e13693. https://doi.org/10.1371/journal.pone.0013693

Sanmarco, L.M., J.M. Rone, C.M. Polonio, G. Fernandez Lahore, F. Giovannoni, K. Ferrara, C. Gutierrez-Vazquez, N. Li, A. Sokolovska, A. Plasencia, et al. 2023. Lactate limits CNS autoimmunity by stabilizing HIF-1α in dendritic cells. *Nature*. 620:881–889. https://doi.org/10.1038/s41586-023-06409-6

Saravanan, V., G.J. Berman, and S.J. Sober. 2020. Application of the hierarchical bootstrap to multi-level data in neuroscience. *Neuron Behav. Data Anal. Theor.* 3:1–25.

Schwartz, D.L., G. Powis, A. Thitai-Kumar, Y. He, J. Bankson, R. Williams, R. Lemos, J. Oh, A. Volgin, S. Soghomonyan, et al. 2009. The selective hypoxia inducible factor-1 inhibitor PX-478 provides in vivo radiosensitization through tumor stromal effects. *Mol. Cancer Ther.* 8:947–958. https://doi.org/10.1158/1535-7163.MCT-08-0981

Seguella, L., and B.D. Gulbransen. 2021. Enteric glial biology, intercellular signalling and roles in gastrointestinal disease. *Nat. Rev. Gastroenterol. Hepatol.* 18:571–587. https://doi.org/10.1038/s41575-021-00423-7

Seguella, L., B. Thomasi, S. Basili Franzin, J.L. Mcclain, R. Lavalle, A. Zilli, V. Parmar, G. Esposito, and B.D. Gulbransen. 2025. Hyperactive enteric glia contribute to persistent dysmotility following inflammation by driving aberrant excitatory responses in neurons. *Cell Mol. Gastroenterol. Hepatol.* 20:101634. https://doi.org/10.1016/j.jcmgh.2025.101634

Serbina, N.V., T. Jia, T.M. Hohl, and E.G. Pamer. 2008. Monocyte-mediated defense against microbial pathogens. *Annu. Rev. Immunol.* 26:421–452. https://doi.org/10.1146/annurev.immunol.26.021607.090326

Serbina, N.V., C. Shi, and E.G. Pamer. 2012. Monocyte-mediated immune defense against murine Listeria monocytogenes infection. *Adv. Immunol.* 113:119–134. https://doi.org/10.1016/B978-0-12-394590-7.00003-8

Sharkey, K.A., and G.M. Mawe. 2023. The enteric nervous system. *Physiol. Rev.* 103:1487–1564. https://doi.org/10.1152/physrev.00018.2022

Sharp, F.R., and M. Bernaudin. 2004. HIF1 and oxygen sensing in the brain. *Nat. Rev. Neurosci.* 5:437–448. https://doi.org/10.1038/nrn1408

Sherman, B.T., M. Hao, J. Qiu, X. Jiao, M.W. Baseler, H.C. Lane, T. Imamichi, and W. Chang. 2022. DAVID: a web server for functional enrichment analysis and functional annotation of gene lists (2021 update). *Nucleic Acids Res.* 50(W1):W216–W221. https://doi.org/10.1093/nar/gkac194

Shi, C., T. Jia, S. Mendez-Ferrer, T.M. Hohl, N.V. Serbina, L. Lipuma, I. Leiner, M.O. Li, P.S. Frenette, and E.G. Pamer. 2011. Bone marrow mesenchymal stem and progenitor cells induce monocyte emigration in response to circulating toll-like receptor ligands. *Immunity*. 34:590–601. https://doi.org/10.1016/j.immuni.2011.02.016

Stavely, R., A.A. Rahman, J.L. Mueller, A.R. Leavitt, C.Y. Han, W. Pan, K.N. Kaiser, L.C. Ott, T. Ohkura, R.A. Guyer, et al. 2024. Mature enteric neurons have the capacity to reinnervate the intestine with glial cells as their guide. *Neuron*. 112:3143–3160.e6. https://doi.org/10.1016/j.neuron.2024.06.018

Street, K., D. Risso, R.B. Fletcher, D. Das, J. Ngai, N. Yosef, E. Purdom, and S. Dudoit. 2018. Slingshot: Cell lineage and pseudotime inference for single-cell transcriptomics. *BMC Genomics*. 19:477. https://doi.org/10.1186/s12864-018-4772-0

Suárez-Fariñas, M., M. Tokuyama, G. Wei, R. Huang, A. Livanos, D. Jha, A. Levescot, H. Irizar, R. Kosoy, S. Cording, et al. 2021. Intestinal inflammation modulates the expression of ACE2 and TMPRSS2 and potentially overlaps with the pathogenesis of SARS-CoV-2-related disease. *Gastroenterology*. 160:287–301.e20. https://doi.org/10.1053/j.gastro.2020.09.029

Takeo, Y., N. Kurabayashi, M.D. Nguyen, and K. Sanada. 2016. The G protein-coupled receptor GPR157 regulates neuronal differentiation of radial glial progenitors through the Gq-IP3 pathway. *Sci. Rep.* 6:25180. https://doi.org/10.1038/srep25180

Tannahill, G.M., A.M. Curtis, J. Adamik, E.M. Palsson-Mcdermott, A.F. Mcgettrick, G. Goel, C. Frezza, N.J. Bernard, B. Kelly, N.H. Foley, et al. 2013. Succinate is an inflammatory signal that induces IL-1β through HIF-1α. *Nature*. 496:238–242. https://doi.org/10.1038/nature11986

Taylor, C.T., and S.P. Colgan. 2017. Regulation of immunity and inflammation by hypoxia in immunological niches. *Nat. Rev. Immunol.* 17:774–785. https://doi.org/10.1038/nri.2017.103

Tong, Z., and Z. Yin. 2024. Distribution, contribution and regulation of nestin. *J. Adv. Res.* 61:47–63. https://doi.org/10.1016/j.jare.2023.08.013

Viola, M.F., M. Chavero-Pieres, E. Modave, M. Delfini, N. Stakenborg, M.C. Estévez, N. Fabre, I. Appeltans, T. Martens, K. Vandereyken, et al. 2023. Dedicated macrophages organize and maintain the enteric nervous system. *Nature*. 618:818–826. https://doi.org/10.1038/s41586-023-06200-7

Vuong, T.A., S.J. Lee, Y.E. Leem, J.R. Lee, G.U. Bae, and J.S. Kang. 2019. SGTb regulates a surface localization of a guidance receptor BOC to promote neurite outgrowth. *Cell Signal.* 55:100–108. https://doi.org/10.1016/j.cellsig.2019.01.003

Wang, T., S. Chen, Z. Wang, S. Li, X. Fei, and M. Zhang. 2024. KIRREL promotes the proliferation of gastric cancer cells and angiogenesis through the PI3K/AKT/mTOR pathway. *J. Cell Mol. Med.* 28:e18020. https://doi.org/10.1111/jcmm.18020

Wang, Y.B., Z.J. Gan, J.Y. Zhang, S. Wanchana, and X.L. Guo. 2023. Suppression of SAMSN1 contributes to neuroprotection in neonatal rats suffering from hypoxic-ischemic encephalopathy injury. *Ibrain*. 9:3–12. https://doi.org/10.1002/ibra.12078

Watts, E.R., and S.R. Walmsley. 2019. Inflammation and hypoxia: HIF and PHD isoform selectivity. *Trends Mol. Med.* 25:33–46. https://doi.org/10.1016/j.molmed.2018.10.006

Weise, S.C., G. Arumugam, A. Villarreal, P. Videm, S. Heidrich, N. Nebel, V.I. Dumit, F. Sananbenesi, V. Reimann, M. Craske, et al. 2019. FOXG1 regulates PRKAR2B transcriptionally and posttranscriptionally via miR200 in the adult hippocampus. *Mol. Neurobiol.* 56:5188–5201. https://doi.org/10.1007/s12035-018-1444-7

White, J.P., S. Xiong, N.P. Malvin, W. Khoury-Hanold, R.O. Heuckeroth, T.S. Stappenbeck, and M.S. Diamond. 2018. Intestinal dysmotility syndromes following systemic infection by flaviviruses. *Cell*. 175:1198–1212.e12. https://doi.org/10.1016/j.cell.2018.08.069

Windster, J.D., A. Sacchetti, G.J. Schaaf, E.M. Bindels, R.M. Hofstra, R.M. Wijnen, C.E. Sloots, and M.M. Alves. 2023. A combinatorial panel for flow cytometry-based isolation of enteric nervous system cells from human intestine. *EMBO Rep.* 24:e55789. https://doi.org/10.15252/embr.202255789

Xie, Z., A. Bailey, M.V. Kuleshov, D.J.B. Clarke, J.E. Evangelista, S.L. Jenkins, A. Lachmann, M.L. Wojciechowicz, E. Kropiwnicki, K.M. Jagodnik, et al. 2021. Gene set knowledge discovery with Enrichr. *Curr. Protoc.* 1:e90. https://doi.org/10.1002/cpz1.90

Xu, Z., Y. Rao, Y. Huang, T. Zhou, R. Feng, S. Xiong, T.F. Yuan, S. Qin, Y. Lu, X. Zhou, et al. 2020. Efficient strategies for microglia replacement in the central nervous system. *Cell Rep.* 32:108041. https://doi.org/10.1016/j.celrep.2020.108041

Yang, J., Y. Zhao, L. Zhang, H. Fan, C. Qi, K. Zhang, X. Liu, L. Fei, S. Chen, M. Wang, et al. 2018. RIPK3/MLKL-mediated neuronal necroptosis modulates the M1/M2 polarization of microglia/macrophages in the ischemic cortex. *Cereb. Cortex*. 28:2622–2635. https://doi.org/10.1093/cercor/bhy089

Young, H.M., J.B. Furness, P. Sewell, E.F. Burcher, and C.J. Kandiah. 1993. Total numbers of neurons in myenteric ganglia of the guinea-pig small intestine. *Cell Tissue Res.* 272:197–200. https://doi.org/10.1007/BF00323587

Young, P., L. Qiu, D. Wang, S. Zhao, J. Gross, and G. Feng. 2008. Single-neuron labeling with inducible Cre-mediated knockout in transgenic mice. *Nat. Neurosci.* 11:721–728. https://doi.org/10.1038/nn.2118

Zhan, X., M. Cao, A.S. Yoo, Z. Zhang, L. Chen, G.R. Crabtree, and J.I. Wu. 2015. Generation of BAF53b-Cre transgenic mice with pan-neuronal Cre activities. *Genesis*. 53:440–448. https://doi.org/10.1002/dvg.22866

Zhang, Y., and W. Hu. 2021. Mouse enteric neuronal cell culture. *Methods Mol. Biol.* 2311:63–71. https://doi.org/10.1007/978-1-0716-1437-2_6

Zhou, Y., J. Yang, D.J. Watkins, L.A. Boomer, M.A. Matthews, Y. Su, and G.E. Besner. 2013. Enteric nervous system abnormalities are present in human necrotizing enterocolitis: Potential neurotransplantation therapy. *Stem Cell Res. Ther.* 4:157. https://doi.org/10.1186/scrt387

Zhu, J., B. Zhang, E.N. Smith, B. Drees, R.B. Brem, L. Kruglyak, R.E. Bumgarner, and E.E. Schadt. 2008. Integrating large-scale functional genomic data to dissect the complexity of yeast regulatory networks. *Nat. Genet.* 40:854–861. https://doi.org/10.1038/ng.167

JEM

Supplemental material

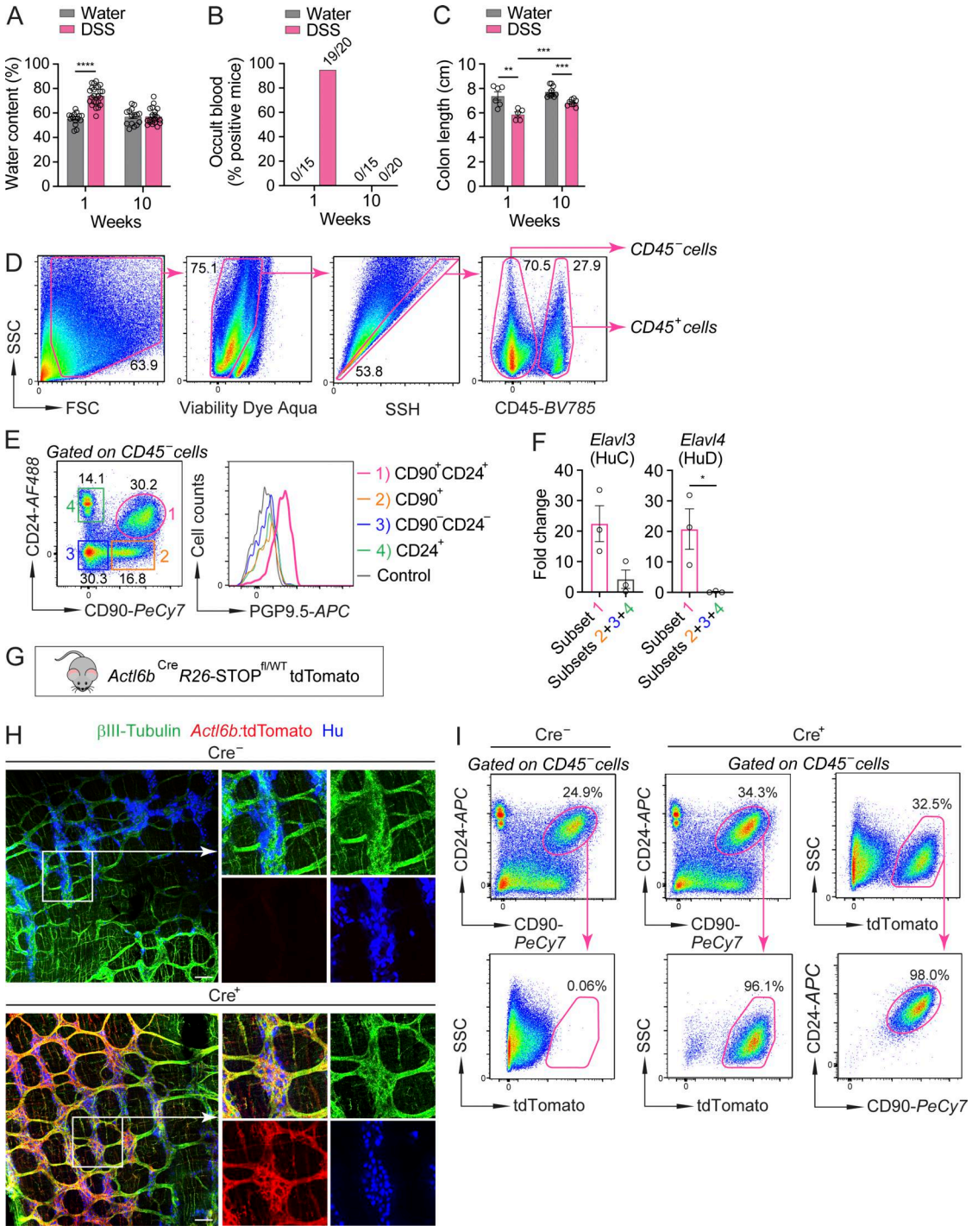

Figure S1. **Colitis is associated with the loss and recovery of nonhematopoietic CD90⁺CD24⁺ myenteric cells enriched in neurons. (A)** Water content in fecal pellets of 3×DSS- or water-treated WT mice (control, *n* = 15; DSS, *n* = 20). **(B)** Occult blood in fecal pellets of 3×DSS- or water-treated WT mice (control, *n* = 15; DSS, *n* = 20). **(C)** Colon length in 3×DSS- or water-treated WT mice (control, *n* = 6–10; DSS, *n* = 5–8). **(D)** FC gating strategy to identify CD45⁺ immune cells (including MMs) and CD45⁻ nonhematopoietic stromal cells (including myenteric neurons) in colonic muscularis. **(E)** Intracellular expression of pan-neuronal marker PGP9.5 by four CD45⁻ nonhematopoietic subsets identified based on their co-expression of CD90 and CD24, shown by FC. **(F)** Relative expression by qPCR of pan-neuronal genes *Elavl3* (HuC) and *Elavl4* (HuD) by FACS-purified CD45⁻ subsets defined in E, normalized to *Actb* (*n* = 3 per group, *n*—independent cell sorting). **(G)** Transgenic mice used in H and I. **(H)** Confocal images of colonic myenteric plexus isolated from control *R26*-STOP$^{fl/WT}$tdTomato (Cre⁻, top) and *Actl6b*^{Cre}*R26*-STOP$^{fl/WT}$tdTomato (Cre⁺, bottom) mice at steady state, stained with Hu (neuronal somas), tdTomato (Baf53b(*Actl6b*):tdTomato⁺ neurons), and βIII-tubulin (nerve fibers) antibodies. Scale bars, 100 µm. **(I)** FC plots showing gating strategy and percentage of *Actl6b*:tdTomato⁺ neurons among total CD45⁻CD90⁺CD24⁺ cells (left, Cre⁻ and Cre⁺) or percentage of CD90⁺CD24⁺ cells among total CD45⁻*Actl6b*:tdTomato⁺ neurons (right Cre⁺) in colonic muscularis isolated from control *R26*-STOP$^{fl/WT}$tdTomato (Cre⁻) and *Actl6b*^{Cre}*R26*-STOP$^{fl/WT}$tdTomato (Cre⁺) mice at steady state. All graphs show the mean ± SEM, *n*—mouse unless stated differently. Data are representative of at least two independent experiments with similar results. Statistical analyses: unpaired Student's *t* test (A, C, and F), *P ≤ 0.05, **P ≤ 0.01, ***P ≤ 0.001, and ****P ≤ 0.0001.

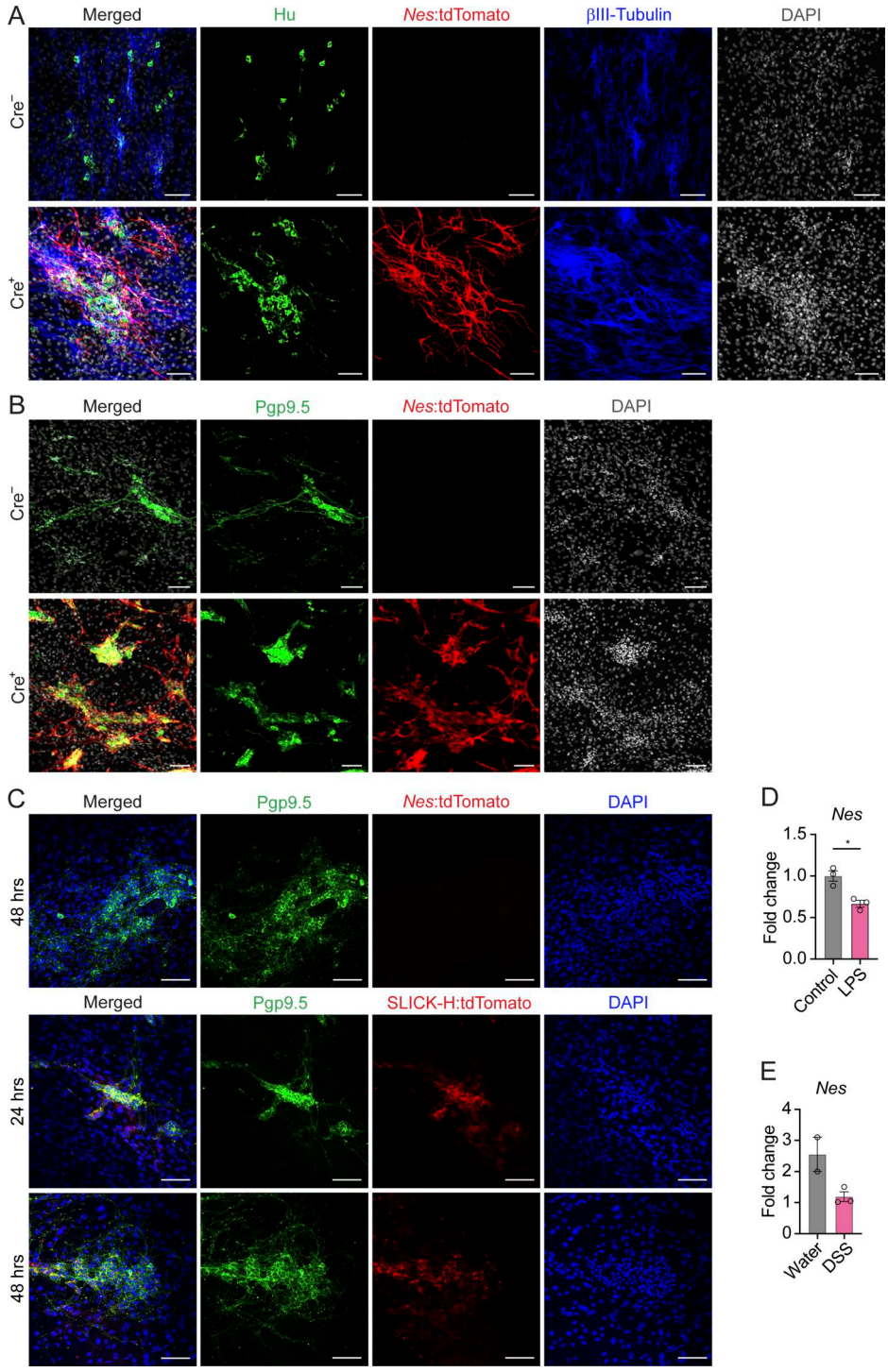

Figure S2. ***In vitro* validation of *Nes*$^{ER\text{-}Cre}$*R26*-STOP$^{fl/fl}$tdTomato fate-mapping strategy to detect newborn neurons. (A)** Confocal images of primary adult myenteric neuronal cultures derived from colonic muscularis of tamoxifen-treated control *R26*-STOP$^{fl/fl}$tdTomato (Cre⁻, top) and *Nes*$^{ER\text{-}Cre}$*R26*-STOP$^{fl/fl}$tdTomato (Cre⁺, bottom) mice, stained with Hu (neuronal somas), tdTomato (Nestin⁺ precursor–derived cells), and βIII-tubulin (nerve fibers) antibodies, and DAPI (nuclei). Scale bars, 100 µm. **(B)** Confocal images of primary adult myenteric neuronal cultures described in A stained with PGP9.5 (whole neurons), tdTomato (Nestin⁺ precursor–derived cells), and DAPI (nuclei). Scale bars, 100 µm. **(C)** Confocal images of primary adult myenteric neuronal cultures derived from colonic muscularis of naïve *Nes*$^{ER\text{-}Cre}$*R26*-STOP$^{fl/fl}$tdTomato (Cre⁺, top) and control SLICK-H$^{ER\text{-}Cre}$*R26*-STOP$^{fl/fl}$tdTomato (Cre⁺, bottom) mice and treated with 4-hydroxytamoxifen *in vitro* for 24 or 48 h, stained with PGP9.5 (whole neurons), tdTomato (Cre-targeted cells), and βIII-tubulin (nerve fibers) antibodies, and DAPI (nuclei). Scale bars, 100 µm. **(D)** *Nes* expression in mature neurons differentiated *in vitro* from the myenteric plexus of WT adult mice (2 wk in cell culture) and treated with LPS or vehicle as in Fig. 6 F, normalized to *Actb* (n = 3, n—replica wells in the same cell culture). **(E)** *Nes* expression by qPCR in CD45⁻CD90⁺CD24⁺ myenteric neurons FACS-purified from water- and DSS-treated mice on day 7 after starting the DSS regimen, normalized to *Actb* (n = 2–3, n—independent cell sorting). All graphs show the mean ± SEM. Data are representative of at least two independent experiments with similar results. Statistical analyses: unpaired Student's t test (D), *P ≤ 0.05.

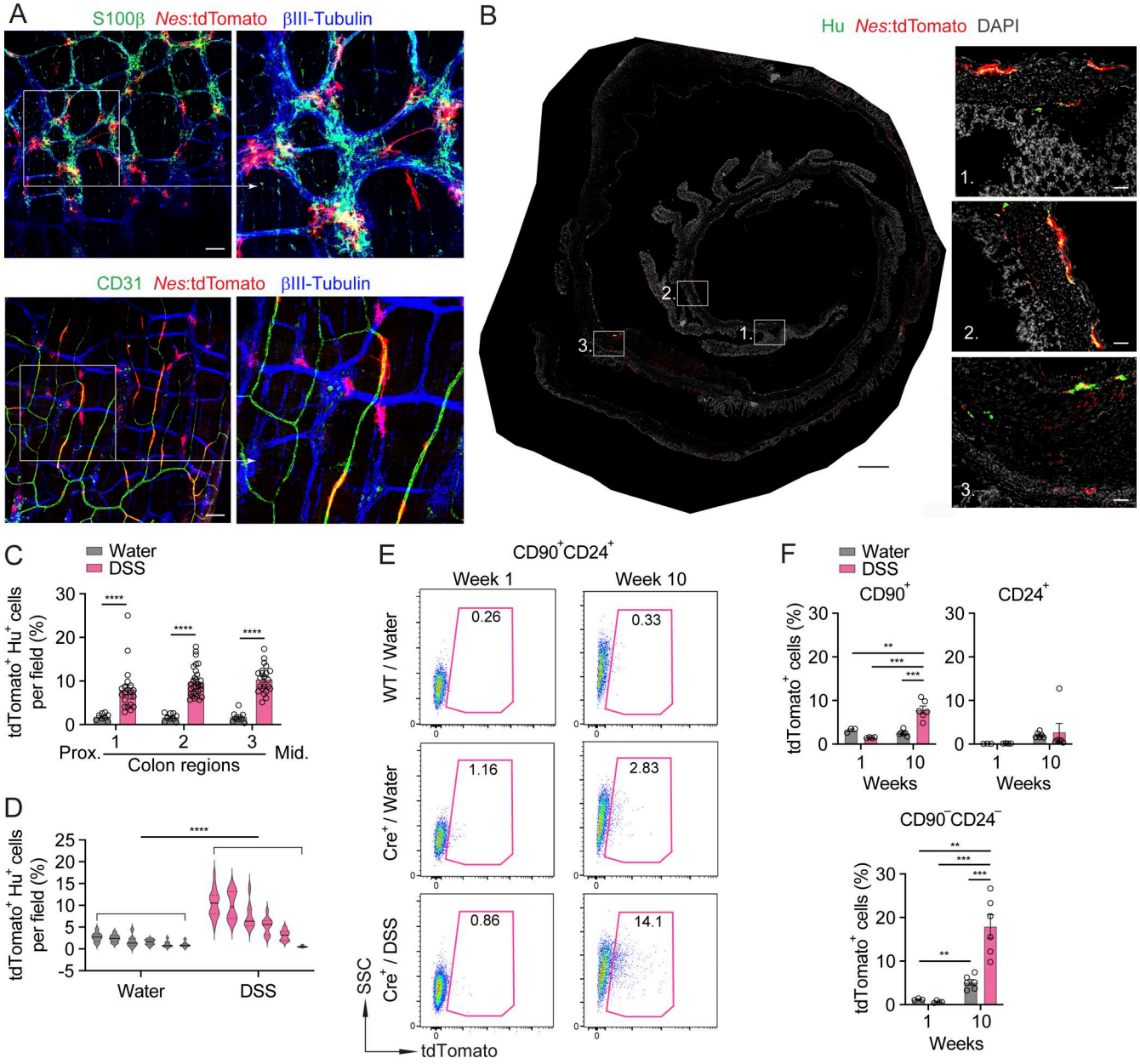

Figure S3. **Colitis facilitates neurogenesis in the colonic myenteric plexus. (A)** Confocal images of colonic myenteric plexus isolated from tamoxifen- and 1×DSS-treated *Nes*$^{ER\text{-}Cre}$*R26*-STOP$^{fl/fl}$tdTomato (Cre$^+$) mice on day 45 (6.5 wk) and stained with S100β (enteric glia, top) or CD31 (blood endothelial cells, bottom), tdTomato (newborn cells), and βIII-tubulin (nerve fibers) antibodies. Scale bars, 100 µm. **(B)** Confocal image of full-length colon Swiss roll cross-section from tamoxifen- and 3×DSS-treated Cre$^+$ mice at week 10, stained with antibodies to Hu (neuronal somas), tdTomato (newborn cells), and DAPI (nuclei). Overview image—scale bar, 500 µm. Magnified images—scale bars, 50 µm. **(C)** Percentage of newly generated tdTomato$^+$Hu$^+$ neurons among total Hu$^+$ myenteric neurons in proximal to middle regions of the colon from tamoxifen- and 3×DSS- or water-treated Cre$^+$ mice at week 10 after starting DSS, quantified by confocal microscopy of muscularis whole mounts (water, n =8–9; and DSS, n = 21–30, n—microscopy fields of view in the same mouse). **(D)** Complementary to Fig. 2 E: percentage of newly generated tdTomato$^+$Hu$^+$ neurons among total colonic myenteric neurons per field per mouse in tamoxifen- and 3×DSS- or water-treated Cre$^+$ mice at week 10, quantified by confocal microscopy of muscularis whole mounts. Data represent the mean ± SEM of 5–10 fields of view analyzed per mouse per group. Each violin plot represents a mouse (n = 6 per group). **(E)** Complementary to Fig. 2 F: FC plots showing percentages of newly generated tdTomato$^+$ cells among total CD45$^-$CD90$^+$CD24$^+$ myenteric neurons in colonic muscularis isolated from tamoxifen- and 3×DSS- or water-treated *Nes*$^{ER\text{-}Cre}$*R26*-STOP$^{fl/fl}$tdTomato (Cre$^+$) mice as compared to control *R26*-STOP$^{fl/fl}$tdTomato (WT) mice. **(F)** Complementary to Fig. 2 F: percentage of newly generated tdTomato$^+$ cells among CD45$^-$ nonhematopoietic CD90$^+$, CD24$^+$, and CD90$^-$CD24$^-$ stromal cells in colonic myenteric plexus from mice described in E, quantified by FC (control, n = 3–6; DSS, n = 4–6). Week 10 data are from the same mice as in D. All graphs show the mean ± SEM, n—mouse. Data are representative of at least two independent experiments with similar results. Statistical analyses: unpaired Student's t test (C and F) and two-way ANOVA for multiple comparisons (D), **P ≤ 0.01, ***P ≤ 0.001, and ****P ≤ 0.0001.

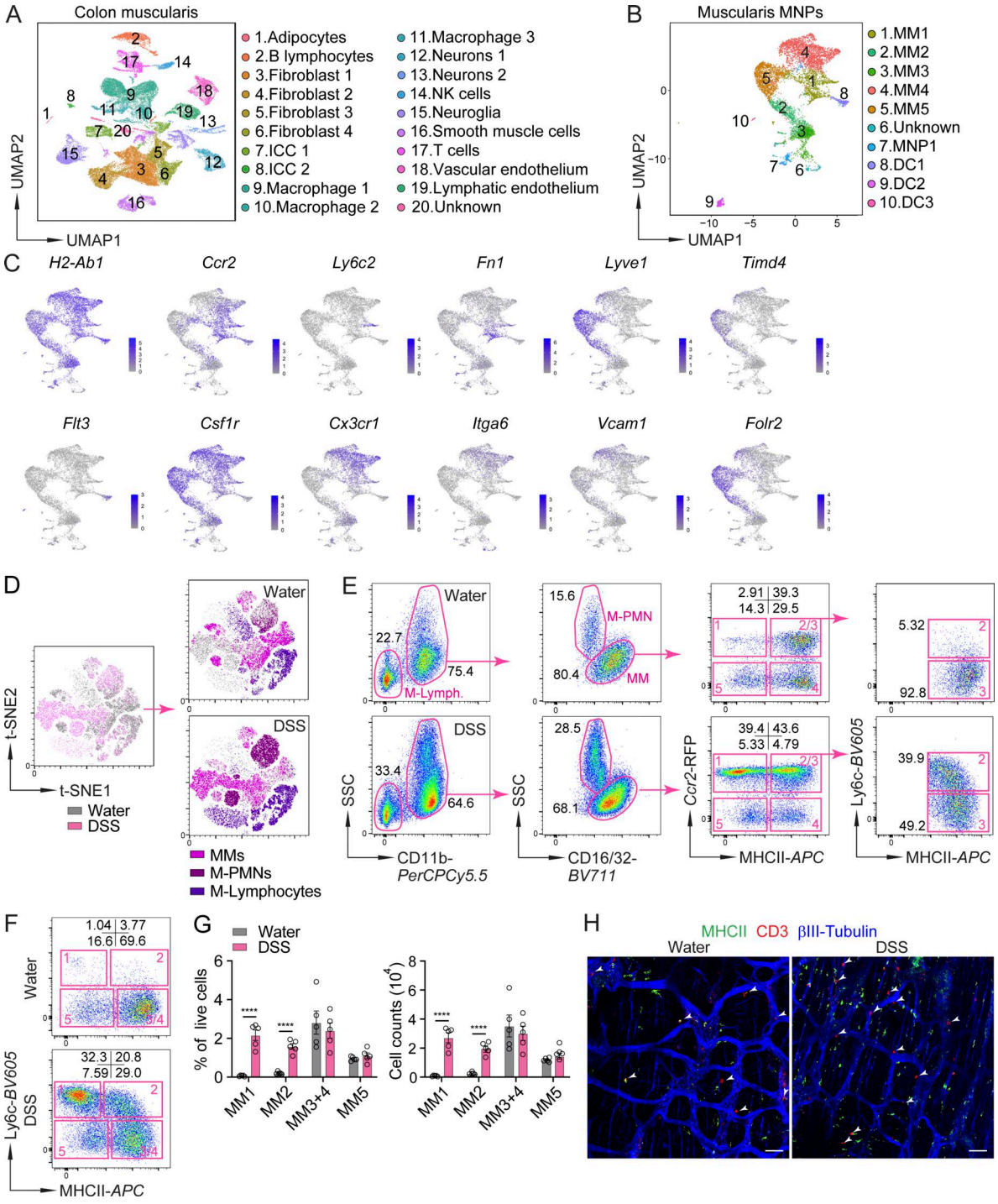

Figure S4. **Monocyte-derived MMs are the dominant immune cell type expanding in the myenteric plexus in response to colitis. (A)** Uniform Manifold Approximation and Projection (UMAP) clustering analysis of scRNA-seq dataset generated from colonic muscularis of normal adult WT mice. Cell type for each cluster annotated based on specific marker genes. ICC, interstitial cells of Cajal; NK cells, natural killer cells. **(B)** UMAP clustering analysis of all MNPs in the scRNA-seq dataset described in A. DC, dendritic cell. **(C)** Complementary to Fig. 4 E: normalized gene expression of 12 marker genes across muscularis MNP clusters identified in B. **(D)** FC t-SNE plots showing immune cell landscape of CD45$^+$ viable single cells in colonic muscularis from 1×DSS- or water-treated *Ccr2*$^{RFP/+}$*Cx3cr1*$^{GFP/+}$ reporter mice at week 1. **(E)** FC plots showing gating strategy for colonic MM subsets and their percentages based on *Ccr2*-RFP expression in 1×DSS- or water-treated *Ccr2*$^{RFP/+}$*Cx3cr1*$^{GFP/+}$ mice described in D, gated on CD45$^+$ viable single cells. **(F)** FC plots showing colonic MM subsets and their percentages based on Ly6c expression in the same 1×DSS- or water-treated *Ccr2*$^{RFP/+}$*Cx3cr1*$^{GFP/+}$ mice as in D, gated on CD45$^+$CD11b$^+$CD16/32$^+$ viable single cells. **(G)** Percentage of total viable cells (left) and absolute cell counts (right) of MM subsets based on Ly6c expression in the experiment described in D, quantified by FC (n = 5 per group). **(H)** Fluorescence microscopy images of colonic myenteric plexus from 1×DSS- (2.25%) or water-treated WT mice at week 1, stained with MHCII (MMs), βIII-tubulin (nerve fibers), and CD3 (T cells) antibodies. White arrowheads point to CD3$^+$ T cells. Scale bars, 50 µm. All graphs show the mean ± SEM, n—mouse. Data are representative of at least two independent experiments with similar results (D–H). Statistical analyses: unpaired Student's t test (G), ****P ≤ 0.0001. MNPs, mononuclear phagocytes.

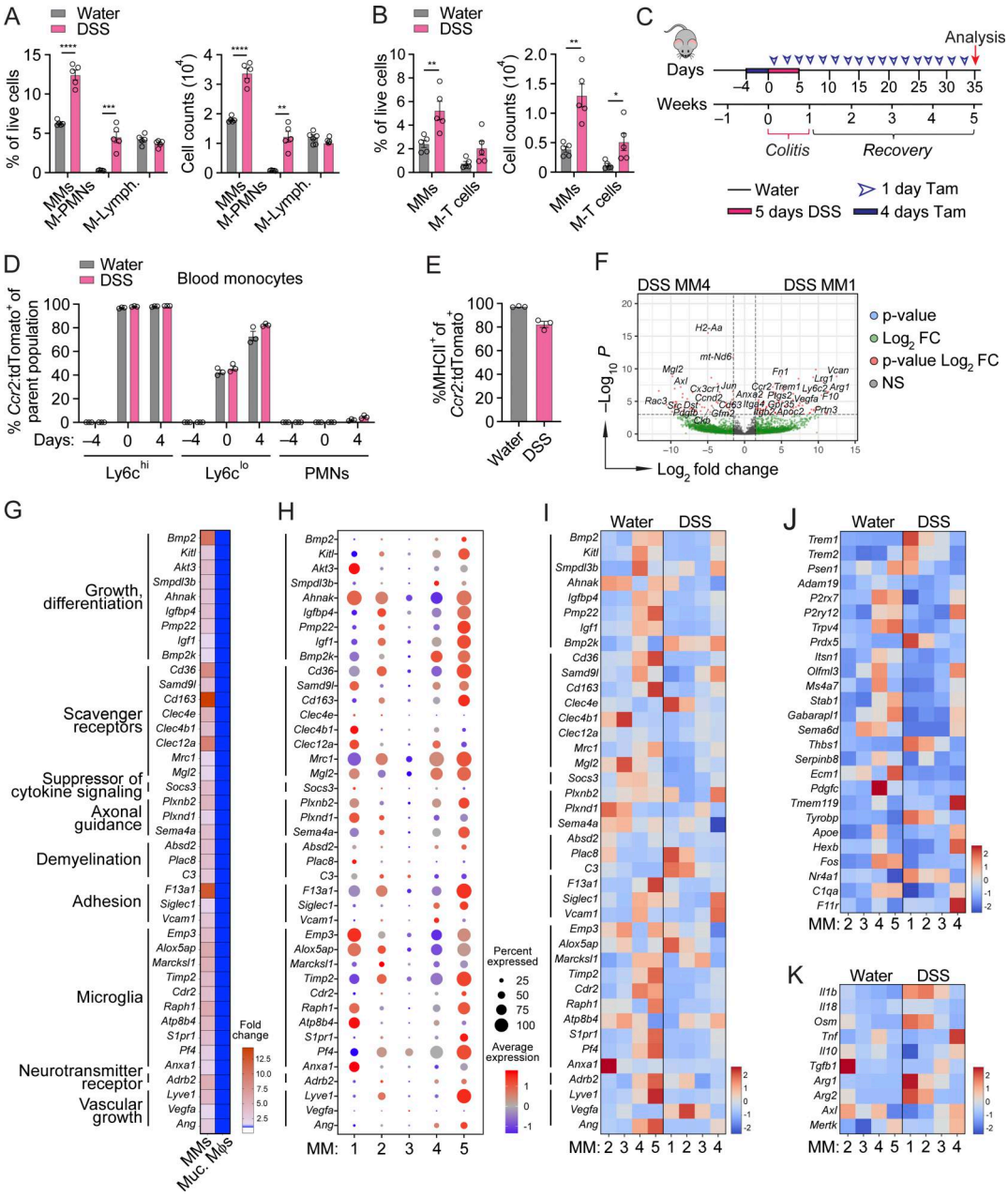

Figure S5. **Transcriptional profiling of monocyte-derived MMs predicts their crosstalk with enteric neurons. (A)** Percentage of total viable cells (left) and absolute cell counts (right) of major immune cell types in the colonic muscularis single-cell suspensions from 1×DSS- or water-treated *Ccr2*$^{RFP/+}$*Cx3cr1*$^{GFP/+}$ reporter mice at week 1, quantified by FC (n = 5 per group). **(B)** Percentage of total viable cells (left) and absolute cell counts (right) of MMs and M-T cells in 1×DSS- or water-treated WT mice at week 1, quantified by FC (n = 5 per group). **(C)** Experimental design used in D and Fig. 4 K: 3×DSS and tamoxifen (Tam) were given as shown. **(D)** Percentage of tdTomato$^+$ cells among Ly6c^{hi} and Ly6c^{lo} monocytes, and PMNs in the blood of tamoxifen- and 1×DSS- or water-treated *Ccr2*$^{ER\text{-}Cre}$*R26*-STOP$^{fl/fl}$tdTomato mice, quantified by FC (n = 3 per group). Sampling was done in the same animals across time points. **(E)** Percentage of MHCII$^+$ cells among *Ccr2*:tdTomato$^+$ cells in 1×DSS or water-treated *Ccr2*$^{ER\text{-}Cre}$*R26*-STOP$^{fl/fl}$tdTomato mice, quantified by confocal microscopy of whole muscularis (n = 3 per group). Data represent the mean ± SEM of 5–6 fields of view analyzed per mouse per group. **(F)** Volcano plot showing a comparison of gene expression between the most distinct Mo-MMs: DSS MM1 and DSS MM4 from the same experiment as in Fig. 4 F. The limma model was used to calculate the P value and fold change. The cutoff for significance is adjusted P value: 1E−5 and Log_2 fold change (Log_2FC) >1.5 or <−1.5. **(G)** Heat map showing genes (referred to as MM Core Signature genes) highly expressed in MMs as compared to mucosal macrophages (Muc. Mϕs) in ImmGen gene array dataset generated from normal small bowel MNPs. **(H)** scRNA-seq dot heatmap showing expression of MM Core Signature genes across five MM clusters identified in Fig. 4 E. Color denotes the average expression level, and size represents the percentage of cells expressing the indicated genes. **(I)** Subset RNA-seq heatmap showing expression of MM Core Signature genes across MM subsets defined by FC in Fig. 4 F, and isolated by four-way FACS from 1×DSS- or water-treated *Ccr2*$^{RFP/+}$*Cx3cr1*$^{GFP/+}$ mice at week 1. **(J)** Subset RNA-seq heatmap showing expression of brain microglia–specific genes from the literature by MM subsets defined by FC in Fig. 4 F, isolated by four-way FACS from 1×DSS- or water-treated *Ccr2*$^{RFP/+}$*Cx3cr1*$^{GFP/+}$ mice at week 1. **(K)** Subset RNA-seq heatmap showing expression of pro- and anti-inflammatory genes by MM subsets defined by FC in Fig. 4 F, isolated by four-way FACS from 1×DSS- or water-treated *Ccr2*$^{RFP/+}$*Cx3cr1*$^{GFP/+}$ mice at week 1. All graphs show the mean ± SEM, n—mouse. Data are representative of at least two independent experiments with similar results (A, B, D, and E). Statistical analyses: unpaired Student's t test (B, D, and E) and multiple t test (A), *P ≤ 0.05, **P ≤ 0.01, ***P ≤ 0.001, and ****P ≤ 0.0001.

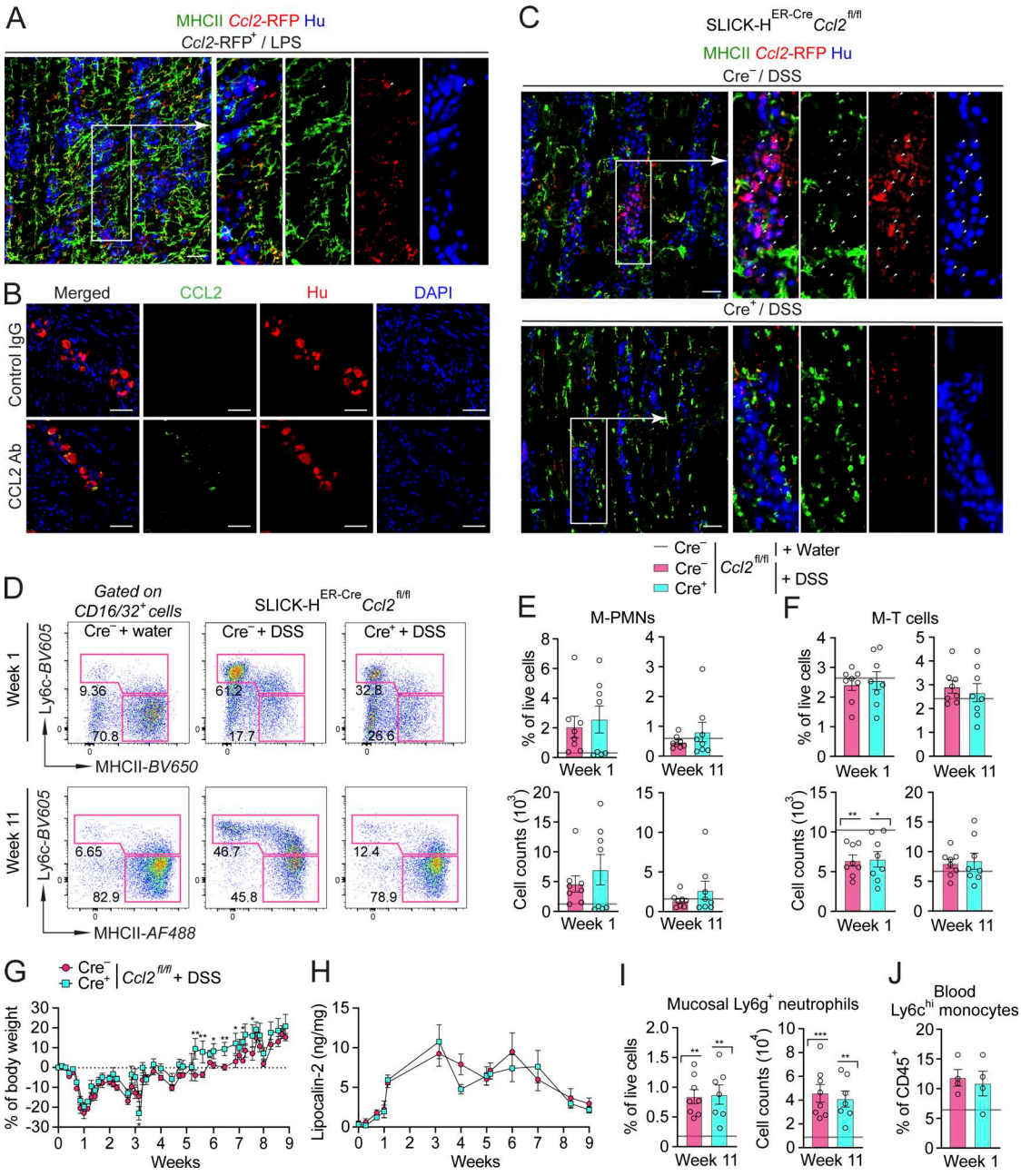

Figure S6. **Efficacy of CCL2 depletion and extent of intestinal inflammation in SLICK-H$^{ER\text{-}Cre}$*Ccl2*$^{fl/fl}$ mice. (A)** Complementary to Fig. 5 D: confocal images of colonic myenteric plexus from LPS-injected *Ccl2*-RFP$^{fl/fl}$ mice, stained with MHCII (MMs), tdTomato (*Ccl2*-RFP), and Hu (neuronal somas) antibodies. White arrowheads indicate CCL2$^+$Hu$^+$ neurons. Scale bars, 50 µm. **(B)** Confocal images of large bowel muscularis from the inflamed tissue cross-section of a CD patient described in Fig. 3, M–O, stained with CCL2 or isotype control IgG and Hu (neuronal somas) antibodies, and DAPI (nuclei). Scale bars, 50 µm. **(C)** Confocal images of colonic myenteric plexus from tamoxifen- and 1×DSS-treated SLICK-H$^{ER\text{-}Cre}$*Ccl2*-RFP$^{fl/fl}$ (Cre$^+$) and *Ccl2*-RFP$^{fl/fl}$ (Cre$^-$) littermates at week 1, stained with MHCII (MMs), tdTomato (*Ccl2*-RFP), and Hu (neuronal somas) antibodies. White arrowheads indicate CCL2$^+$ Hu$^+$ neurons. Scale bars, 50 µm. **(D)** Complementary to Fig. 5 F: FC plots showing proportions of Ly6c$^+$ and Ly6c$^-$ Mo-MM subsets and their percentages in colons of tamoxifen- and 3×DSS-(2.15%) or water-treated SLICK-H$^{ER\text{-}Cre}$*Ccl2*-RFP$^{fl/fl}$ (Cre$^+$) and *Ccl2*-RFP$^{fl/fl}$ (Cre$^-$) littermates. **(E)** Percentage of total viable cells (left) and absolute cell counts (right) of colonic M-PMNs in mice described in D, quantified by FC (DSS Cre$^-$ and Cre$^+$, *n* = 8 per group). Baseline shows the mean value for tamoxifen- and water-treated Cre$^-$ littermates (water Cre$^-$, *n* = 5–6). **(F)** Percentage of total viable cells (left) and absolute cell counts (right) of colonic M-T cells in mice described in D, quantified by FC (DSS Cre$^-$ Cre$^+$, *n* = 8 per group; water Cre$^-$ baseline, *n* = 5–6). P values above each column indicate statistical differences against baseline. **(G)** Percentage of body weight change in tamoxifen- and 3×DSS-treated mice described in D (DSS Cre$^-$ and Cre$^+$, *n* ≥ 10 per group). **(H)** Fecal lipocalin-2 in tamoxifen- and 3×DSS-treated mice described in D (DSS Cre$^-$ and Cre$^+$, *n* ≥ 10 per group). **(I)** Percentage of total viable cells (left) and absolute cell counts (right) of colonic mucosal Ly6g$^+$ neutrophils in mice described in D, quantified by FC (DSS Cre$^-$ and Cre$^+$, *n* = 7–8 per group; water Cre$^-$ baseline, *n* = 5–6). P values above each column indicate statistical differences against baseline. **(J)** Percentage of blood Ly6c^{hi} monocytes among total viable CD45$^+$ blood cells in mice described in D, quantified by FC (DSS Cre$^-$ and Cre$^+$, *n* = 4 per group; Water Cre$^-$ baseline, *n* = 3). All graphs show the mean ± SEM, *n*—mouse. Data are representative of at least two independent experiments with similar results. Data are pooled from 3 smaller experiments (G and H). Statistical analyses: unpaired Student's *t* test (E, F, I, and J) and multiple *t* tests (G and H), *P ≤ 0.05, **P ≤ 0.01, and ***P ≤ 0.001.

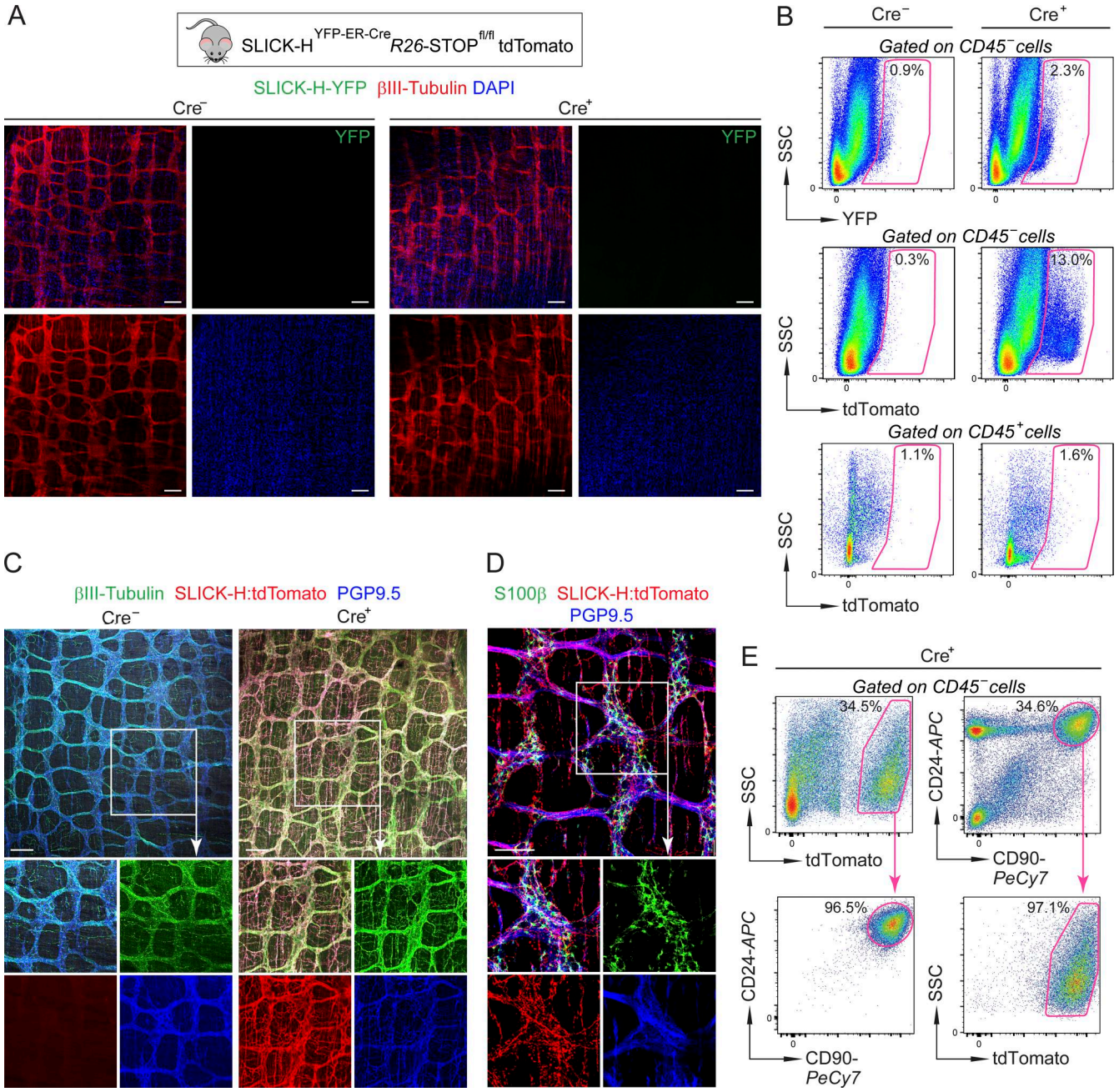

Figure S7. **Tamoxifen-inducible Cre expression in SLICK-H$^{ER\text{-}Cre}$ mice selectively targets neurons in the colonic myenteric plexus. (A)** Confocal images of colonic myenteric plexus from untreated (control) *R26*-STOP$^{fl/fl}$tdTomato (Cre$^-$, left) and SLICK-H$^{ER\text{-}Cre}$*R26*-STOP$^{fl/fl}$tdTomato (Cre$^+$, right) mice, stained with βIII-tubulin antibody (nerve fibers), endogenous SLICK-H-YFP (YFP), and DAPI (nuclei). Scale bars, 100 µm. **(B)** FC plots showing percentage of YFP$^+$ and tdTomato$^+$ cells among CD45$^-$ cells in colonic muscularis of tamoxifen-treated control Cre$^-$ (left) and Cre$^+$ (right) mice described in A. **(C)** Confocal images of colonic myenteric plexus from tamoxifen-treated control Cre$^-$ (left) and Cre$^+$ (right) mice described in A, stained with βIII-tubulin (nerve fibers), tdTomato (Cre-targeted cells), and PGP9.5 (whole neurons) antibodies. Scale bars, 100 µm. **(D)** Confocal images of colonic myenteric plexus from tamoxifen-treated Cre$^+$ mice described in A, stained with s100β (enteric glia), tdTomato (Cre-targeted cells), and PGP9.5 (whole neurons) antibodies. Scale bars, 100 µm. **(E)** FC plots showing percentage of CD90$^+$CD24$^+$ cells among total CD45$^-$ SLICK-H:tdTomato$^+$ cells (left) or SLICK-H:tdTomato$^+$ cells among total CD45$^-$CD90$^+$CD24$^+$ cells (right) in colonic muscularis of tamoxifen-treated Cre$^+$ mice described in A.

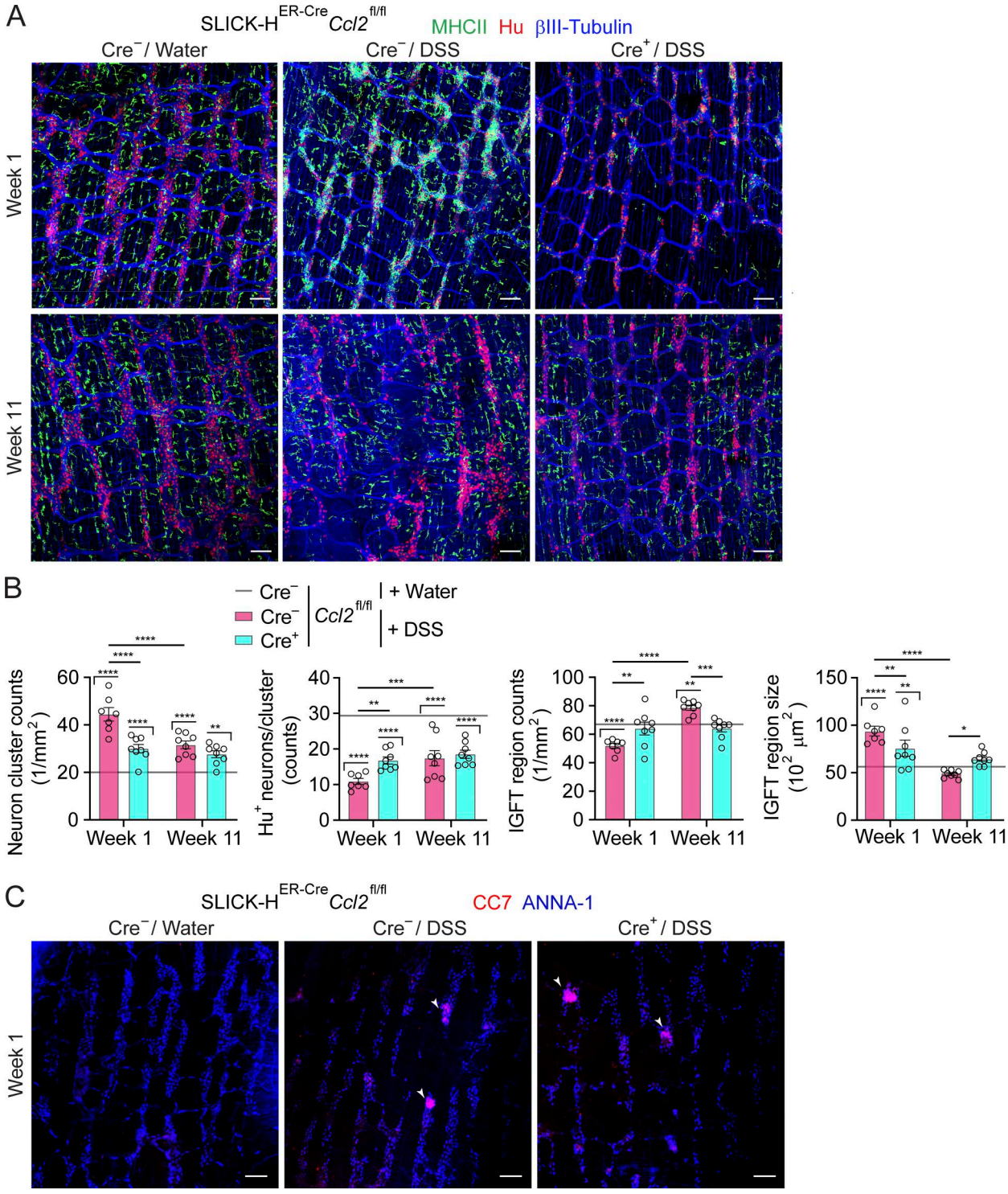

Figure S8. **Mo-MMs recruited by enteric neurons via the CCL2 axis facilitate myenteric plexus remodeling. (A)** Complementary to Fig. 5, F and G: confocal images of colonic myenteric plexus from tamoxifen- and 3×DSS- or water-treated SLICK-H$^{ER\text{-}Cre}$*Ccl2*$^{fl/fl}$ (Cre$^+$) and *Ccl2*$^{fl/fl}$ (Cre$^-$) littermates, stained with antibodies specific to MHCII (MMs), Hu (neuronal somas), and βIII-tubulin (nerve fibers). Images are representative of control and DSS mice (DSS Cre$^-$ and Cre$^+$, *n* = 7–8 per group; water Cre$^-$ baseline, *n* = 4–6). Scale bars, 100 µm. **(B)** Complementary to Fig. 5 G: structural changes in colonic myenteric plexus of mice described in A quantified by confocal microscopy, showing counts of neuron clusters, counts of Hu$^+$ neurons per cluster, and counts and area of IGFT regions (DSS Cre$^-$ and Cre$^+$, *n* = 7–8; water Cre$^-$ baseline, *n* = 4–6). Each value is the mean per mouse. P values above each column show statistical differences against baseline. **(C)** Complementary to Fig. 5 I: confocal images of colonic myenteric plexus from mice described in A at week 1, stained with CC7 (apoptotic cells) and ANNA-1 (neuronal somas) antibodies. Images are representative of control and DSS mice (DSS Cre$^-$ and Cre$^+$, *n* = 4 per group; water Cre$^-$ baseline, *n* = 2). White arrowheads point to clusters of CC7$^+$ANNA-1$^+$ neurons. Scale bars, 100 µm. Graphs show the mean ± SEM, *n*—mouse. Data are representative of at least two independent experiments with similar results. Statistical analyses: two-way ANOVA for multiple comparisons (B), *P ≤ 0.05, **P ≤ 0.01, ***P ≤ 0.001, and ****P ≤ 0.0001.

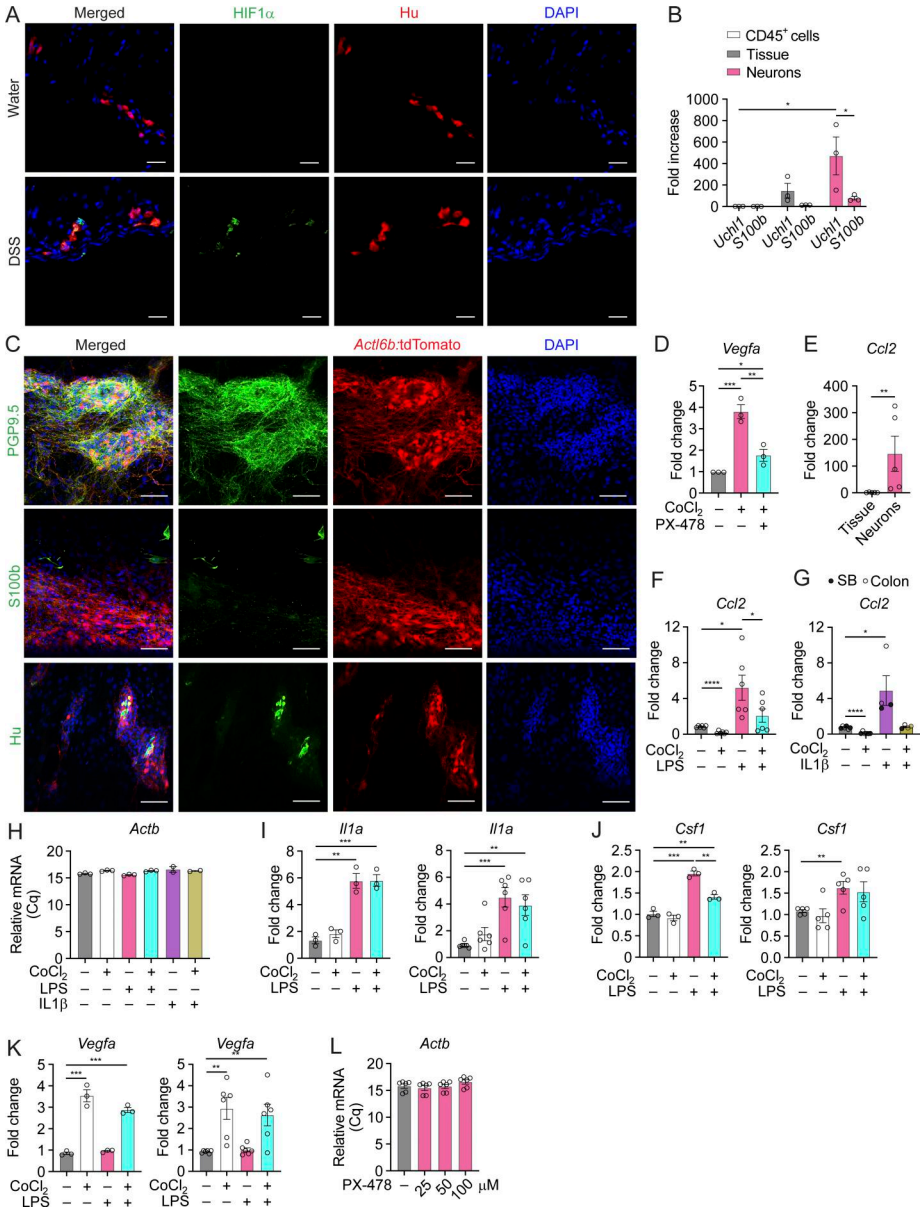

Figure S9. **HIF1 signaling in cultured myenteric neurons negatively regulates CCL2 expression. (A)** Confocal images of colonic muscularis tissue cross-sections from water- or 1×DSS- (3.5%) treated WT mice at week 1, stained with HIF1α (hypoxic cells) and Hu (neuronal somas) antibodies, and DAPI (nuclei). Scale bars, 25 µm. **(B)** *Uchl1* and *s100b* expression by qPCR in primary adult myenteric neuronal cultures as compared to total colonic muscularis tissue and sorted hematopoietic CD45⁺ cells as a negative control, normalized to *Actb* (n = 3 per group, n—independent cell culture or independent cell sorting). **(C)** Confocal images of primary adult myenteric neuronal cultures derived from colonic muscularis of *Actl6b*^{Cre}*R26*-STOP$^{fl/WT}$tdTomato (Cre⁺) mice at steady state, stained with tdTomato (*Actl6b*:tdTomato⁺ cells), PGP9.5 (whole neurons), s100β (enteric glia), and Hu (neuronal somas) antibodies, and DAPI (nuclei). Scale bars, 100 µm. **(D)** *Vegfa* expression by qPCR in cultured adult colonic myenteric neurons from WT mice, treated with $CoCl_2$, HIF1α inhibitor PX-478, or their combinations, normalized to *Actb* (n = 3 per group, n—replica wells in the same cell culture). **(E)** *Ccl2* expression by qPCR in cultured adult colonic myenteric neurons as compared to adult colonic muscularis tissue, normalized to *Actb* (n = 5 per group, n—independent cell culture or mice). **(F)** Complementary to Fig. 6 F: *Ccl2* expression by qPCR in cultured adult colonic myenteric neurons treated with $CoCl_2$, LPS, or their combination, normalized to *Actb* (n = 6 per group, n—independent cell culture). **(G)** *Ccl2* expression by qPCR in cultured SB or colonic myenteric neurons treated with $CoCl_2$, IL-1β, or their combination, normalized to *Actb* (n = 4–6 per group, n—replica wells in the same cell culture). **(H)** *Actb* mRNA expression (Cq, Quantification cycle) by qPCR in cultured adult colonic myenteric neurons treated with $CoCl_2$, LPS, IL-1β, or their combination (n = 3, n—replica wells in the same cell culture). **(I)** *Il1a* expression by qPCR in cultured adult colonic myenteric neurons treated with $CoCl_2$, LPS, or their combination, normalized to *Actb* (left, n = 3, n—replica wells in the same cell culture; right, n = 6, n—independent cell culture). **(J)** *Csf1* expression by qPCR in cultured adult colonic myenteric neurons treated with $CoCl_2$, LPS, or their combination, normalized to *Actb* (left, n = 3, n—replica wells in the same cell culture; right, n = 5, n—independent cell culture). **(K)** *Vegfa* expression by qPCR in cultured adult colonic myenteric neurons treated with $CoCl_2$, LPS, or their combination, normalized to *Actb* (left, n = 3, n—replica wells in the same cell culture; right, n = 6, n—independent cell culture). **(L)** *Actb* mRNA expression (Cq) by qPCR in cultured colonic myenteric neurons treated with increasing concentrations of PX-478 as indicated (n = 6, n—replica wells in the same cell culture). All graphs show the mean ± SEM. Data are representative of at least two independent experiments with similar results (A–L) or as indicated. Statistical analyses: unpaired Student's t test (D, E, and, G–L), paired t test (F), and two-way ANOVA for multiple comparisons (B), *P ≤ 0.05, **P ≤ 0.01, ***P ≤ 0.001, and ****P ≤ 0.0001. SB, small bowel.

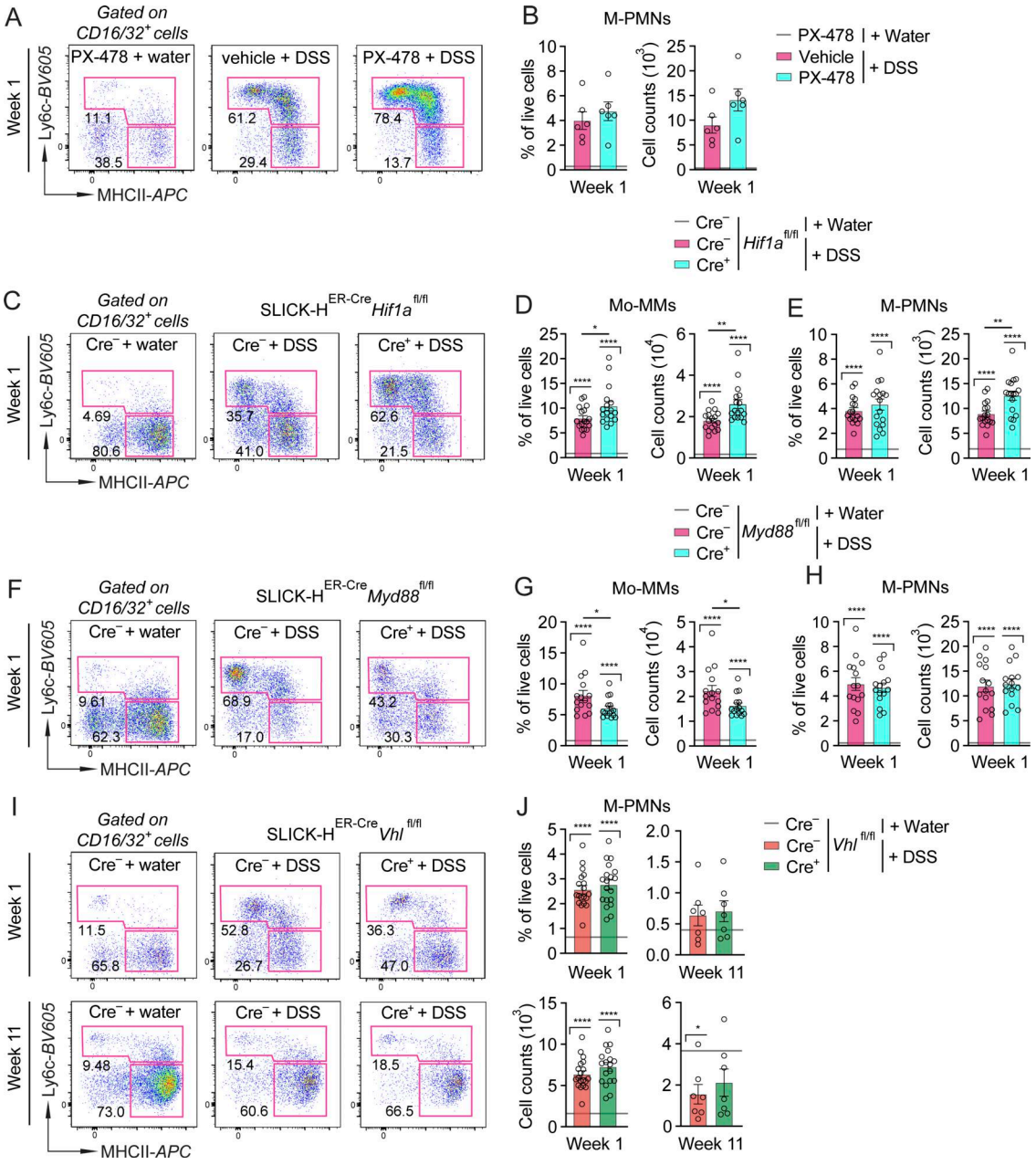

Figure S10. **Myenteric inflammation in mice treated with the HIF1α inhibitor PX-478 or with neuron-specific depletion of *Myd88*, *Hif1a*, or *Vhl*.** **(A)** Complementary to Fig. 6 K: FC plots showing colonic Mo-MM subsets and their percentages in 1×DSS- or water-treated WT mice injected daily with PX-478 or vehicle. **(B)** Percentage of total viable cells (left) and absolute cell counts (right) of colonic M-PMNs in mice described in A, quantified by FC (DSS vehicle and PX-478, *n* = 6 per group). Baseline shows mean value for PX-478–injected mice on water (*n* = 1). **(C)** FC plots showing colonic Mo-MM subsets and their percentages in tamoxifen- and 1×DSS- (3%) or water-treated SLICK-H$^{ER\text{-}Cre}$*Hif1a*$^{fl/fl}$ (Cre$^+$) or *Hif1a*$^{fl/fl}$ (Cre$^-$) littermates. **(D)** Percentage of total viable cells (left) and absolute cell counts (right) of colonic Mo-MMs in mice described in C, quantified by FC (DSS Cre$^-$ and Cre$^+$, *n* = 17 per group). Baseline shows the mean value for tamoxifen- and water-treated *Hif1a*$^{fl/fl}$ littermates (Water Cre$^-$, *n* = 13). P values above each column show statistical differences against baseline. **(E)** Percentage of total viable cells (left) and absolute cell counts (right) of colonic M-PMNs in mice described in C (DSS Cre$^-$ and Cre$^+$, *n* = 17 per group), quantified by FC (baseline Water Cre$^-$, *n* = 13). P values above each column show statistical differences against baseline. **(F)** FC plots of colonic Mo-MM subsets and their percentages in tamoxifen- and 1×DSS- (3%) or water-treated SLICK-H$^{ER\text{-}Cre}$*Myd88*$^{fl/fl}$ (Cre$^+$) or *Myd88*$^{fl/fl}$ (Cre$^-$) littermates. **(G)** Percentage of total viable cells (left) and absolute cell counts (right) of colonic Mo-MMs in mice described in F, quantified by FC (DSS Cre$^-$ and Cre$^+$, *n* = 15 per group). Baseline shows the mean value for tamoxifen- and water-treated *Myd88*$^{fl/fl}$ littermates (Water Cre$^-$, *n* = 12). P values above each column show statistical differences against baseline. **(H)** Percentage of total viable cells (left) and absolute cell counts (right) of colonic M-PMNs in mice described in F (DSS Cre$^-$ and Cre$^+$, *n* = 15 per group), quantified by FC (baseline water Cre$^-$, *n* = 12). P values above each column show statistical differences against baseline. **(I)** Complementary to Fig. 6 M: FC plots of colonic Mo-MM subsets and their percentages in tamoxifen- and 3×DSS- or water-treated SLICK-H$^{ER\text{-}Cre}$*Vhl*$^{fl/fl}$ (Cre$^+$) or *Vhl*$^{fl/fl}$ (Cre$^-$) littermates. **(J)** Percentage of total viable cells (top) and absolute cell counts (bottom) of colonic M-PMNs in mice described in I, quantified by FC (DSS Cre$^-$ and Cre$^+$, *n* = 18–19 per group). Baseline shows the mean value for tamoxifen- and water-treated *Vhl*$^{fl/fl}$ littermates (baseline water Cre$^-$, *n* = 5–9). All graphs show the mean ± SEM, *n*—mouse. Data are representative of at least two independent experiments with similar results. Data are pooled from 2 to 4 smaller experiments (B, D, E, G, H, and J). Statistical analyses: unpaired Student's *t* test (B, D, E, G, H, and J), *P ≤ 0.05, **P ≤ 0.01, and ****P ≤ 0.0001.

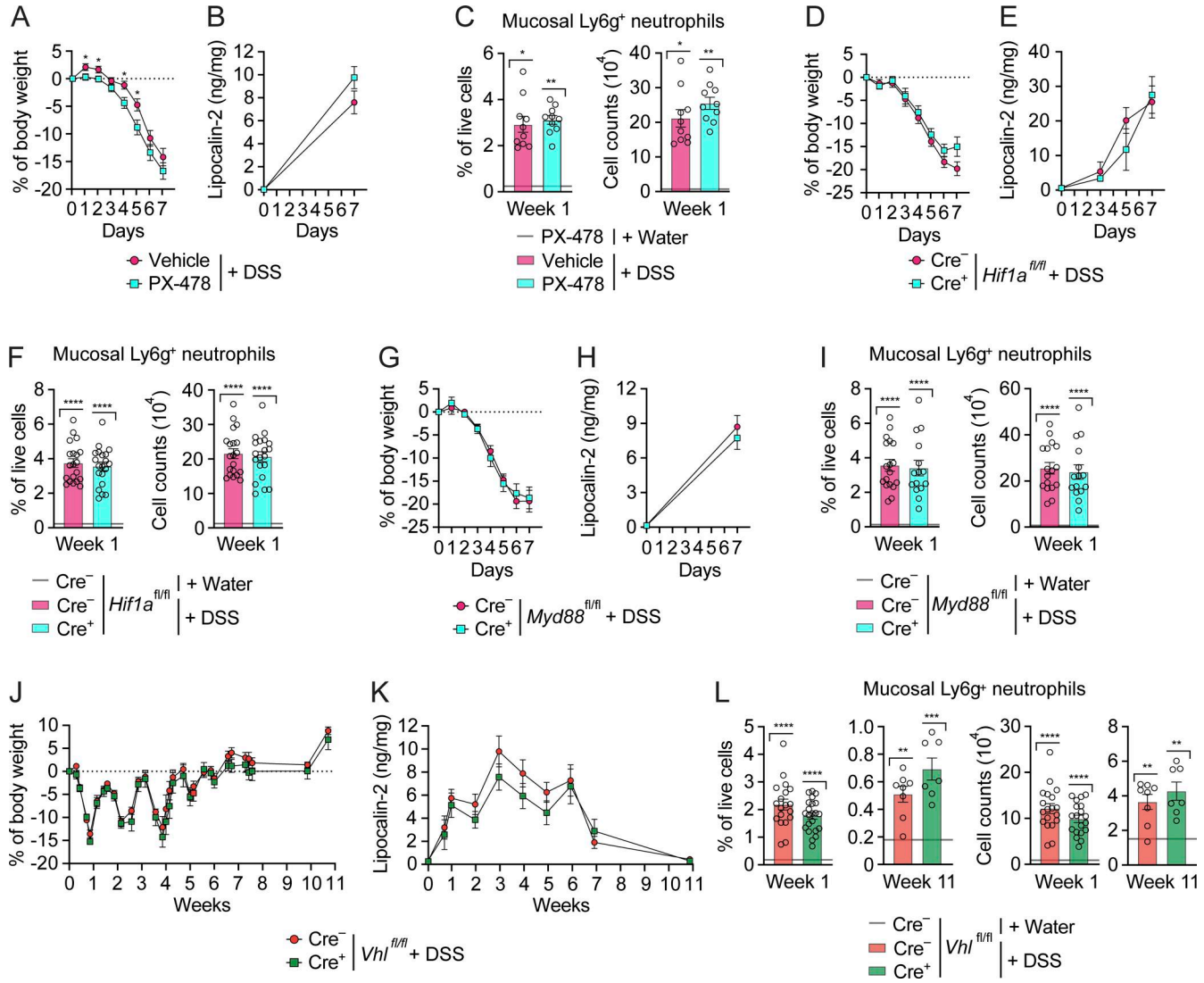

Figure S11. **Mucosal inflammation in mice treated with the HIF1α inhibitor PX-478 or with neuron-specific depletion of *Myd88*, *Hif1a*, or *Vhl*.** **(A)** Related to Fig. 6, I–K: percentage of body weight change in PX-478- or vehicle-injected and 1×DSS-treated WT mice (DSS vehicle and PX-478, *n* = 19 per group). **(B)** Fecal lipocalin-2 in mice described in A (DSS vehicle and PX-478, *n* = 19 per group). **(C)** Percentage of total viable cells (left) and absolute cell counts (right) of mucosal Ly6g$^+$ neutrophils in colons of mice described in A, quantified by FC (DSS vehicle and PX-478, *n* = 10 per group). Baseline shows the mean value for PX-478–injected mice on water (*n* = 1). **(D)** Related to Fig. S10, C–E: percentage of body weight change in tamoxifen- and 1×DSS-treated SLICK-H$^{ER\text{-}Cre}$*Hif1a*$^{fl/fl}$ (Cre$^+$) or *Hif1a*$^{fl/fl}$ (Cre$^-$) littermates (DSS Cre$^-$ and Cre$^+$, *n* = 19–23 per group). **(E)** Fecal lipocalin-2 in mice described in D (DSS Cre$^-$ and Cre$^+$, *n* = 26–31 per group). **(F)** Percentage of total viable cells (left) and absolute cell counts (right) of mucosal Ly6g$^+$ neutrophils in colons of mice described in D, quantified by FC (DSS Cre$^-$ and Cre$^+$, *n* = 20 per group). Baseline shows the mean value for tamoxifen- and water-treated *Hif1a*$^{fl/fl}$ littermates (water Cre$^-$, *n* = 13). P values above each column show statistical differences against baseline. **(G)** Related to Fig. S10, F–H: percentage of body weight change in tamoxifen- and 1×DSS-treated SLICK-H$^{ER\text{-}Cre}$*Myd88*$^{fl/fl}$ (Cre$^+$) and *Myd88*$^{fl/fl}$ (Cre$^-$) littermates (DSS Cre$^-$ and Cre$^+$, *n* = 18 per group). **(H)** Fecal lipocalin-2 levels in mice described in G (DSS Cre$^-$ and Cre$^+$, *n* = 18 per group). **(I)** Percentage of total viable cells (left) and absolute cell counts (right) of mucosal Ly6g$^+$ neutrophils in colons of mice described in G, quantified by FC (DSS Cre$^-$ and Cre$^+$, *n* = 15–18 per group). Baseline shows the mean value for tamoxifen- and water-treated *Myd88*$^{fl/fl}$ littermates (water Cre$^-$, *n* = 12). P values above each column show statistical differences against baseline. **(J)** Complementary to Fig. 6, L–P: percentage of body weight change in tamoxifen- and 3×DSS-treated SLICK-H$^{ER\text{-}Cre}$*Vhl*$^{fl/fl}$ (Cre$^+$) and *Vhl*$^{fl/fl}$ (Cre$^-$) littermates (DSS Cre$^-$ and Cre$^+$, *n* = 8 per group). **(K)** Fecal lipocalin-2 in mice described in J (DSS Cre$^-$ and Cre$^+$, *n* = 35–41 per group). **(L)** Percentage of total viable cells (left) and absolute cell counts (right) of mucosal Ly6g$^+$ neutrophils in colons of mice described in J, quantified by FC (DSS Cre$^-$ and Cre$^+$, *n* = 7–19 per group). Baseline shows the mean value for tamoxifen- and water-treated *Vhl*$^{fl/fl}$ littermates (water Cre$^-$, *n* = 5–9). P values above each column show statistical differences against baseline. All graphs show the mean ± SEM, *n*—mouse. Data are representative of at least two independent experiments with similar results. Data are pooled from two to four smaller experiments. Statistical analyses: unpaired Student's *t* test (C, F, I, and L), multiple *t* test (A, D, G, and J), and two-way ANOVA for multiple comparisons (B, E, H, and K), *P ≤ 0.05, **P ≤ 0.01, ***P ≤ 0.001, and ****P ≤ 0.0001.

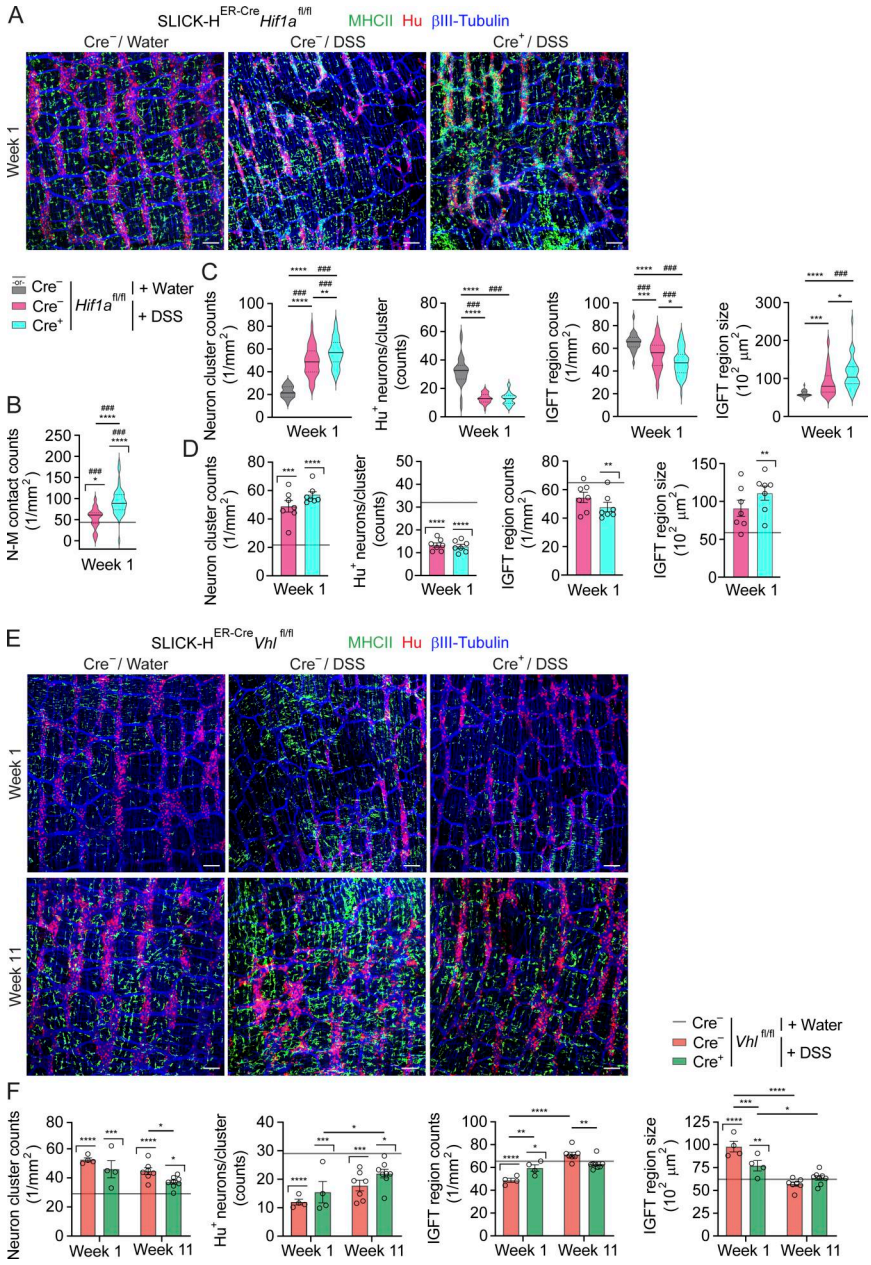

Figure S12. **ENS remodeling in mice with neuron-specific depletion of *Hif1a* or *Vhl*. (A)** Confocal images of colonic myenteric plexus from tamoxifen- and 1×DSS- or water-treated SLICK-H$^{ER\text{-}Cre}$*Hif1a*$^{fl/fl}$ (Cre$^+$) and *Hif1a*$^{fl/fl}$ (Cre$^-$) littermates, stained with MHCII (MMs), Hu (neuronal somas), and βIII-tubulin (nerve fibers) antibodies. Images are representative of control and DSS mice (DSS Cre$^-$ and Cre$^+$, *n* = 7 per group; baseline water Cre$^-$, *n* = 6). Scale bars, 100 µm. **(B)** Quantification of contacts between MMs and myenteric neurons in mice described in A by confocal microscopy (DSS Cre$^-$ and Cre$^+$, *n* = 7 per group). Baseline shows the mean value for tamoxifen- and water-treated *Hif1a*$^{fl/fl}$ littermates (water Cre$^-$, *n* = 6). Data are shown as a distribution of pooled values generated from analysis of 5–8 fields of view per mouse per group. P values above each violet plot show statistical differences against baseline. **(C)** Structural changes in myenteric plexus of mice described in A quantified by confocal microscopy, showing counts of total neuron clusters, counts of Hu$^+$ neurons per cluster, and counts and area of IGFT regions (DSS Cre$^-$ and Cre$^+$, *n* = 7 per group; baseline water Cre$^-$, *n* = 6). Data are shown as a distribution of pooled values generated from analysis of 5–8 fields of view per mouse per group. **(D)** Data same as in C shown as mean value per mouse per group (DSS Cre$^-$ and Cre$^+$, *n* = 7 per group; baseline water Cre$^-$, *n* = 6). P values above each column show statistical differences against baseline. **(E)** Complementary to Fig. 6 N: confocal images of colonic myenteric plexus from tamoxifen- and 3×DSS- or water-treated SLICK-H$^{ER\text{-}Cre}$*Vhl*$^{fl/fl}$ (Cre$^+$) and *Vhl*$^{fl/fl}$ (Cre$^-$) littermates, stained with MHCII (MMs), Hu (neuronal somas), and βIII-tubulin (nerve fibers) antibodies. Images are representative of control and DSS mice (DSS Cre$^-$ and Cre$^+$, *n* = 4–7 per group; baseline water Cre$^-$, *n* = 2–3). Scale bars, 100 µm. **(F)** Complementary to Fig. 6 N: structural changes in myenteric plexus of mice described in E quantified by confocal microscopy, showing counts of total neuron clusters, counts of Hu$^+$ neurons per cluster, and counts and area of IGFT regions (DSS Cre$^-$ and Cre$^+$, *n* = 4–7 per group; baseline water Cre$^-$, *n* = 2–3). Data same as in Fig. 6 N, shown as mean per mouse per group. P values above each column show statistical differences against baseline. All graphs show the mean ± SEM, *n*—mouse. Data are representative of at least two independent experiments with similar results. Statistical analyses: unpaired Student's *t* test (B), one-way ANOVA (C and D), and two-way ANOVA for multiple comparisons (F), *P ≤ 0.05, **P ≤ 0.01, ***P ≤ 0.001, and ****P ≤ 0.0001. # above pooled data in violin plots (B and C) indicates empirical P values calculated by the Nested Leave-One-Out Jackknife strategy, where ###P < 0.001.

Video 1. **MMs form direct contacts with enteric neurons in the myenteric ganglia.** The representative video shows a 3D rendering of MMs (MHCII Ab, green) in contact with neurons (Hu Ab, red) in the colonic myenteric plexus of WT mice treated with 1×DSS (week 1). Regions of contact are depicted in yellow. The video was generated from a set of two-photon microscopy images taken in the z axis and sequentially rotated using Imaris software. Scale bars, 10 µm.

Video 2. **MMs engulf enteric neurons in the myenteric ganglia.** The representative video shows a 3D rendering of neuronal signals (Hu Ab, red) inside MMs (MHCII Ab, green) in the colonic myenteric plexus of WT mice treated with 1×DSS (week 1). The video was generated from a set of two-photon microscopy images taken in the z axis and sequentially rotated using Imaris software. Scale bars, 5 µm.

Video 3. **MMs contact and engulf enteric neurons in the myenteric ganglia.** The representative video shows a 3D rendering of a colonic myenteric ganglion in WT mice treated with 1×DSS (week 1), wherein MMs (MHCII Ab, green) form direct contacts with neurons (Hu Ab, red) and engulf them. Regions of contact are depicted in yellow. The video was generated from a set of two-photon microscopy images taken in the z axis and sequentially rotated using Imaris software. Scale bars, 20 µm.

Provided online are Table S1, Table S2, Table S3, Table S4, Table S5, Table S6, Table S7, Table S8, Table S9, Table S10, and Table S11. Table S1 provides the list of mouse colon scRNA-seq cluster markers. Table S2 provides the list of DEGs generated from RNA-seq analysis of MM subsets isolated from water- and 1×DSS-treated mice and compared across two conditions (water versus DSS). Table S3 provides the list of DEGs generated from RNA-seq analysis of MM subsets isolated from 1×DSS-treated mice and compared with each other. Table S4 provides pathway analysis for MM subsets isolated from 1×DSS-treated mice. Table S5 provides identity signatures for MM subsets isolated from 1×DSS-treated mice, supplementary to Table S4. Table S6 provides the computational evidence that MM- and neuron-interacting genes from the normal mouse colon scRNA-seq dataset are conserved in DSS colitis. Table S7 provides the list of genes identified as an inflamed enteric neural gene signature from the ileum of CD patients. Table S8 shows antibodies for flow cytometry. Table S9 shows primary antibodies for immunofluorescence. Table S10 shows secondary antibodies for immunofluorescence. Table S11 shows experimental animals.